U.PORTO
FEUP FACULDADE DE ENGENHARIA UNIVERSIDADE DO PORTO

Departamento de Engenharia Mecânica

Programa Doutoral em Engenharia Mecânica (PRODEM)

Methodology to characterize plastic flow and fracture in Single Point Incremental Sheet Metal Forming

Kishore Jagannath Jawale

Advisor	Ana Rosanete Lourenço Reis, PhD Assistant Professor at FEUP and Unit director at INEGI, Porto.
Co-Advisors	José Manuel Ferreira Duarte, PhD Assistant Professor at FEUP.
	Maria Beatriz Cipriano de Jesus Silva, PhD Assistant Professor at IST, Lisbon.

Faculdade de Engenharia da Universidade do Porto (FEUP)
December, 2017

Kishore Jagannath Jawale: Methodology to characterize plastic flow and fracture in Single Point Incremental Sheet Metal Forming, A dissertation submitted in partial fulfilment of the requirements for the degree of Doctor of Philosophy, © December 2017, FEUP, University of Porto, Portugal.

Abstract

The forming limits based on the fracture strains are becoming acknowledged and the major application of these limits is to validate the formability in situations where the fracture precedes necking. Single point incremental forming (SPIF) is a sheet metal forming process which uses universal forming tool to locally deform the sheet and eliminates the use of conventional die and punch. One of the aims of this study is to obtain forming limits based on fracture i.e. Fracture forming Limit (FFL) and Shear Fracture Forming Limit (SFFL), using conventional sheet metal tests and to validate these forming limits using SPIF of copper sheet metal. Complex geometries of copper sheet metal are formed using SPIF so as to validate formability limits. It was found that the FFL and SFFL successfully describes the forming limits and strain points lying below the limits are safe and without fracture. The intersection region between FFL and SFFL is studied. The specific essential work of fracture is calculated for fracture by mode I, mode II and mixed mode I&II, and this can be used to predict the fracture loci on FFL and SFFL. The complete understanding of forming limits on the onset of fracture and specific essential work of fracture will enable us to get a new perspective on the plastic flow and fracture on the onset fracture or in situations when necking is suppressed.

The process parameters like forming tool, step down and feed rate, which affects the formability in SPIF are investigated. The effect of lubrication on the surface finish and formability of the formed component is also studied and optimal lubrication condition for single point incremental forming of copper sheet metal is suggested. The surface morphology of the formed component is investigated using the SEM analysis. The study revealed that there is significant damage due to cyclic loading on the formed component, in the form of micro-cracks and fragmentation. A comparative study is done to investigate the effect of size of forming tool diameter on the surface morphology of the formed component. This study suggests that increase in formability when smaller tool diameter was used, is probably due to decreased fragmentation density.

The grain structure of the copper sheet metal before and after single point incremental forming was investigated. The microstructure shows that there is an elongation of grain boundaries in the longitudinal direction whereas no change of grain boundaries in transverse direction.

Keywords: Single point incremental forming (SPIF); formability limits; fracture forming limits; process parameters; microstructure study; SPIF application; copper.

Resumo

O conhecimento e a caracterização da formabilidade com base nos limites de deformação à rotura tem vindo a aumentar nos últimos anos e a sua principal aplicação é na validação da formabilidade em processos nos quais a rotura é precedida de estrição. A deformação incremental (SPIF - Single point incremental forming) é um processo de deformação de chapa metálica que usa uma ferramenta universal para deformar pontualmente a chapa eliminando, assim, a necessidade de uso de matrizes e punções convencionais. Um dos principais objetivos deste estudo é definir os limites de deformação de chapas de cobre baseados na Curva Limite de Fractura (FFL - Fracture forming Limit) e na Curva Limite de Fractura ao Corte (SFFL - Shear Fracture Forming Limit), recorrendo a ensaios convencionais. Outro dos objetivos deste estudo é validar, com base nos resultados das curvas FFL e SFFL, os limites de deformação em processos de SPIF para geometrias complexas realizadas em chapas de cobre. Após a realização das peças em cobre verificou-se que a FFL e a SFFL definem corretamente os limites de deformação, não tendo ocorrido roturas em todos os pontos com nível de deformação inferior aos estabelecidos por estas curvas.

Foi ainda objeto de estudo a região de interseção das curvas FFL e SFFL. Considerando os três modos de rotura/fratura I, II e misto I&II é possível, com base na energia específica de fratura, calcular a curva de fratura nas curvas FFL e SFFL. O conhecimento dos limites de formabilidade à fratura e da energia específica de fratura permitem ter uma nova perspetiva da deformação plástica e fratura nos processos de deformação em que não ocorre estrição.

Neste trabalho foi estudada a influência na formabilidade dos seguintes parâmetros do processo: geometria da ferramenta, o incremento vertical de deformação (step down) e a velocidade de translação. Foi também estudada a influência da lubrificação no acabamento superficial da peça produzida. Com base neste estudo é sugerida uma condição de lubrificação ideal para SPIF em chapas de cobre.

O estudo da morfologia superficial do componente obtido por SPIF permitiu identificar a existência de danos significativos devido ao carregamento cíclico sob a forma de microfissuras e fragmentação. Foi ainda possível identificar que a dimensão da ferramenta utilizada influência este processo. A diminuição do diâmetro da ferramenta diminui a microfissuração e fragmentação aumentando desta forma a formabilidade.

O estudo realizado sobre a evolução da microestrutura da chapa de cobre com da deformação incremental permitiu identificar uma alteração da geometria do grão neste processo de deformação.

Palavras-chave: estampagem/deformação incremental (SPIF); limites de formabilidade; limites de deformação à fratura; parâmetros de processo; estudo da microestrutura; aplicação SPIF; cobre.

Acknowledgement

"I can no other answer make, but, thanks, and thanks" - William Shakespeare

This work is the fruit of well wishes and sincere guidance of the supervisor and co-supervisors. Firstly, I would express my deep gratitude to Prof. Ana Reis, for her constant support and guidance during my entire PhD by providing facilities, funding, materials and work plan. I owe my most sincere gratitude to Prof. M Beatriz Silva for her help in planning and conducting the experiments and for her careful revision and insightful suggestions regarding the organisation of this thesis. I am also grateful to Prof. J F Duarte for supporting me and providing his expertise particularly in the field of measurements, lubrication study and microstructure analysis for this study.

I would also like to extend my appreciation to my colleagues João Pedro Duarte, Inês Oliveira, Armanda Teixeira, José Francisco Teixeira, Andreia Durães, Diogo Fula, Soumitra Gain, Rui Amaral and Santiago Villa from INEGI and João Magrinho and Joana Correia from IST. Special thanks to my friends for being there and cheering all along.

Kind acknowledgement to EUPHRATES - Erasmus Mundus programme of European Union for granting me with fellowship.

I am eternally grateful to my parents, Shri. Jagannath Jawale and Smt. Laxmi Jawale, for believing in me and showering their unconditional love. The person who has been besides me providing encouragement and love, my wife, Trupti, special thanks to you.

PhD has been a roller coaster ride with many ups and downs. In all these phases I kept deriving my inspiration from late Dr. A P J Abdul Kalam, the missile man of India. His achievements have always amazed me, I look up to him and his quotes always inspires me to keep moving ahead come what may.

Contents

List of Figures

List of Tables

List of Symbols

Abbreviations

3D	Three dimension
CAD	Computer Assisted Design
CAM	Computer Assisted Manufacturing
CBT	Continuous bending under tension
CNC	Computer Numerical Control
CTOD	Crack tip opening displacement
DIC	Digital Image correlation
DNTT	Double notch tensile test
FEM	Finite Element Method
FFL	Fracture Forming Limit Line
FLC	Forming Limit Curve
FLD	Forming Limit Diagram
GPA	Grid process analyser
IFCT	Incremental forming using counter tool
INEGI	Instituto de Engenharia Mecanica e Gestão Industrial
ISF	Incremental sheet metal forming
ISO	International Organization for Standardization
IST	Instituto Superior Técnico
LVDT	Linear variable differential transformer
PC	Personal computer
RD	Rolling direction
RPM	Revolution Per Minute
s-CS	Staggered C-slit shear specimen
s-DNTT	Staggered double notch tensile test
SEM	Scanning electron microscope
SFFL	Shear fracture forming limit
SPIF	Single Point Incremental Forming
TPIF	Two Point Incremental Forming
TR	Triaxiality ratio
UTS	Ultimate tensile stress

Wire-EDM	Wire assisted electric discharge machining

Latin Symbols

a	Length of ligament
A	Elongation at break (in %)
A	Area of the ligament
D	Diameter of geometry
d	Initial diameter of circular grid
E	Young modulus
F	Force
G	Energy release rate
h	Height of the necked down region
K	Stress intensity factor
l_0	Initial length of specimen
N	Ratio of the major and the minor strain
n	Work hardening coefficient
m	Power index
p	Bulge pressure
R	Specific Essential work of fracture
R_a	Average surface roughness
R_{max}	Maximum roughness depth
R_Z	10-point mean roughness
R_I	Fracture toughness for mode I of fracture mechanics
$R_{I\&II}$	Fracture toughness for mixed mode I and II
R_{II}	Fracture toughness for mode II of fracture mechanics
r	Coefficient of anisotropy
$\bar{r}$	Normal anisotropy
r_{tool}	Tool radius
r_{part}	Radius of formed component
t_0	Initial thickness of sheet
t	Thickness of sheet at fracture
V	Radius of die cavity in bulge test

w_0	Initial width of specimen
w	Width of specimen at fracture
W_e	Essential work done for fracture
W_t	Total work done
W_P	Work done over the plastic region
W_Γ	Work done for elastic recovery

Greek symbol

α	Loading path
$\propto$	Forming angle
β	Strain path
Δr	Planar anisotropy
Δz	Step down
δ	Crack tip opening displacement
ε	Strain
ε_1	Principal major strain
ε_2	Principal minor strain
ε_l	Principal strain in length
ε_w	Principal strain in width
ε_t	Principal strain in thickness
$\bar{\varepsilon}$	Effective strain
ε_{1f}	Principal major fracture strain
ε_{1n}	Principal major necking strain
$\bar{\varepsilon}_f$	Effective fracture strain
ρ	Density
σ	Stress
σ_1	Stress in principal direction 1
σ_2	Stress in principal direction 2
σ_3	Stress in principal direction 3
σ_e	Average stress
σ_o	Strength co-efficient
$\bar{\sigma}$	Effective stress

σ_m	Hydrostatic stress
σ_{UTS}	Ultimate strength
σ_y	Yield stress
ψ_{max}	Maximum drawing angle for SPIF
$\emptyset$	Diameter

Chapter 1 **Introduction**

1.1 Motivation and goals

The Forming limit diagram (FLD) is used to characterize the formability of sheet metals. This diagram depicts the relationship between the major and the minor strains. The forming limit curve (FLC) in FLD, developed by Keller [1] and later by Goodwin [2], represents the maximum principal strains the sheet metal can sustain prior to the onset of localized necking. The experimental methods for the determination of the FLC are well established. The circle grid analysis and time dependent methods are the most common ones used to determine the FLC.

The formability limit by fracture has not been of interest to the sheet metal forming community because once a neck appears and spreads sideways under subsequent deformation, thinning will progress very fast under decreasing loads or pressures until the sheet cracks. Recently, there has been a growing interest, to consider the onset of failure by fracture as well as by necking because under certain conditions fracture can precede necking in traditional sheet metal forming processes [3] and in Single Point Incremental Forming (SPIF) [4].

Recent studies by Silva et al. [4] and Isik et al. [5] has showed the importance of the determination of the fracture limits, defining the fracture forming limit line (FFL) and shear fracture forming line (SFFL), being related with fracture by mode I and II of fracture mechanics, respectively. Isik et al. (2014) presented a methodology to characterize the fracture limits that includes the characterization of necking and fracture of tensile, Nakajima, bulge and shear tests in an Aluminium alloy. The region between the FFL and SFFL intersection is yet to be explored and presents an opportunity for research.

In the present study, the FFL and the SFFL is determined for the copper sheet metal with thickness of 0.8 mm. One of the aims of this study is to explore the region between FFL and SFFL using specimens specifically designed to induce fracture by mixed mode I&II of fracture mechanics. Another aim of this study is, to validate the obtained FFL and SFFL using SPIF.

Single point incremental forming can be considered as the rapid prototyping technique for sheet metal forming applications. The process can be carried out on sheet metal without the need of conventional die and punch. An universal forming tool can be used in SPIF to form any asymmetrical or symmetrical component [6]. One of the common application of copper is household decoration. The need of customers to be able to customise their home décor has created a necessity for investigating SPIF for copper sheet metal.

The effect of SPIF process parameters like feed rate, tool diameter and step down on the formability of copper sheet metal is investigated. It is observed that the formability, on the onset of fracture is higher than the conventional forming limit curve defined by necking [4]. The lubrication in manufacturing processes serves to reduce the wear and improve surface finish. In case of SPIF, the lubrication has an effect on formability along with surface finish [7]. The effect of lubrication on both formability and the surface finish is evaluated.

In order to investigate the reason of lubrication affecting formability and surface finish, scanning electron microscopic (SEM) analysis is conducted. The surface morphology is studied using SEM. In addition to this, the effect of single point incremental forming of the copper sheet metal on the grain boundaries are also investigated.

The SPIF applications with complex geometries like a decoration leaf, a vortex decoration bowl and a prototype of ship hull is formed to validate the obtained FFL and SFFL for the copper sheet metal.

1.2 Structure of the thesis

This thesis is organised in 5 chapters. The Chapter 1 entitled, “Introduction”, describes the motivation, the goals and the structure of the thesis.

The general overview of the existing literature on the formability and incremental sheet metal forming is presented in Chapter 2 entitled, “State of the Art”. The primary object of this chapter in to provide adequate context and background for the investigation presented in this thesis. Brief reviews regarding the formability, single point incremental forming, process parameter in SPIF, lubrication in SPIF and applications are included in this chapter. The secondary objective of this chapter is to describe the various methodologies used to calculate specific essential work of fracture, FFL, SFFL and FLC. This chapter also includes brief review of the experimental setups used for the SPIF, the conventional sheet metal tests and the measurement systems.

Chapter 3 entitled, “Experimental Setup” provides a comprehensive description of the material used in this study, the work plan for experiments used to determine material characterization and formability determination and different tools used to perform experiments and analysis.

Chapter 4 entitled, “Results and Discussion” presents the results obtained from the various experiments performed. The results are complimented by appropriate discussion. The experiments, for which the results that are presented in this chapter, includes the material characterization, the specific essential work of fracture calculation, the FLD determination, validation of these limits by SPIF geometries, investigating the effect of various process parameters on the formability, the microstructure analysis and the SPIF application.

The summary of all the topics addressed and the main conclusions obtained from this study are comprehensively discussed in Chapter 5 entitled, “Conclusions”. This thesis ends with the list of references mentioned in the text.

Chapter 2 **State of the Art**

In this chapter the history of the approaches used to study and quantify formability in sheet metal forming are presented. The state of the art related to formability limits in sheet metal forming and in particular single point incremental forming is discussed in detail. The literature review of single point incremental forming and its process parameters is also presented in this chapter.

2.1 Formability limits

Sheet metal forming is a manufacturing process where, using controlled plastic deformation the sheet metal is deformed into a desired shape. Formability is the ability of a material to plastically deform without failure. The forming limits are represented in the Forming Limit Diagram (FLD). The FLD is a graphical representation of the major and the minor strains in the principal strain space. The Forming Limit Curve (FLC) is used to represent the formability limits for the conventional forming, where the failure is caused by the necking. The Fracture forming limit line (FFL) and the Shear fracture forming limit line (SFFL) are used when the failure is to be characterised by the fracture.

2.1.1 Forming limit curve

To plot FLC the major and the minor strains should be measured and in order to be able to measure the strains, either the grid is etched on the sheet before the deformation or, the real-time non-contact measuring system (based on digital image correlation) is used [8].

The use of circles for etched grid on sheet metal instead of other geometric shapes is due to the fact that, it is easier to visually identify the principal major and minor directions in the plane of the sheet as the circles become ellipses after deformation. This observation along with technique would be much more complex if, for example, square shapes were used.

The circle-grid technique was first introduced by Keeler [1] in 1968, and this work was limited to biaxial domain i.e. first quadrant of FLC. Goodwin [2] in 1968, extended this curve in uniaxial domain, i.e. second quadrant of FLD. In the circle-grid technique circular grids are etched on the sheet before forming. After the sheet is formed the grid’s shape is converted into an ellipse or circle (as seen in Table 2.1) due to deformation.

The circles, after deformed, are ellipses and the major and minor axis directions of these ellipses correspond to the local main directions as seen in Figure 2.1b.

Table 2.1: Schematic representation of types of deformed grids due to different loading situations [8]

Uniaxial loading	In-plane stresses	Biaxial stresses
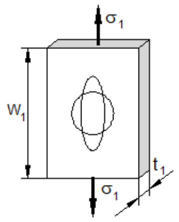	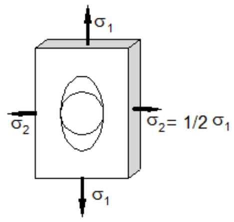	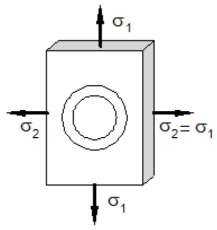

Afterwards, using the obtained limiting strain points, the FLC is plotted, see Figure 2.2. The schematic representation of the methodology to calculate major and minor strains is presented in Figure 2.1.

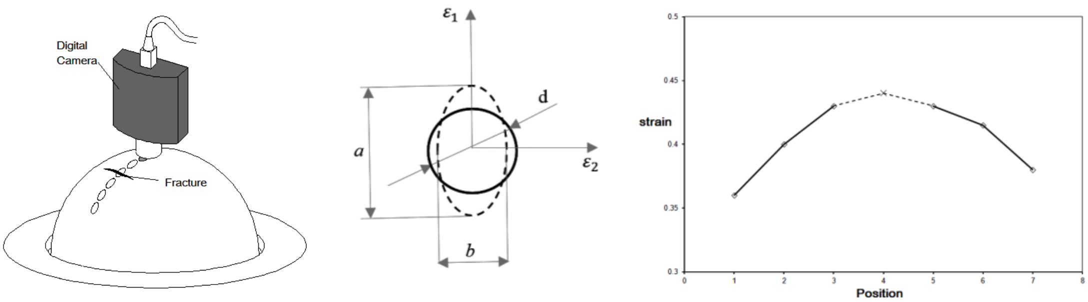

a) b) c)

Figure 2.1: Principal strain measurement using circle-grid technique, a) measuring grids, b) deformed grid and c) plotting bell curve to interpolate principal fracture strains [8].

The principal strains, ε_1 (major strain) and ε_2 (minor strain) for Figure 2.1b are calculated by the equations (2.1) and (2.2) respectively.

$$\varepsilon_1 = \ln\left({}^{a}/_{d}\right) \tag{2.1}$$

$$\varepsilon_2 = \ln\left({}^{b}/_{d}\right) \tag{2.2}$$

Based on the type (uni-axial or bi-axial) of deformation, limiting points in the principal strain space can be plotted which is FLC. Figure 2.2 shows a typical FLC curve with different loading situations, i.e. the tensile, the plane strain and the biaxial loading.

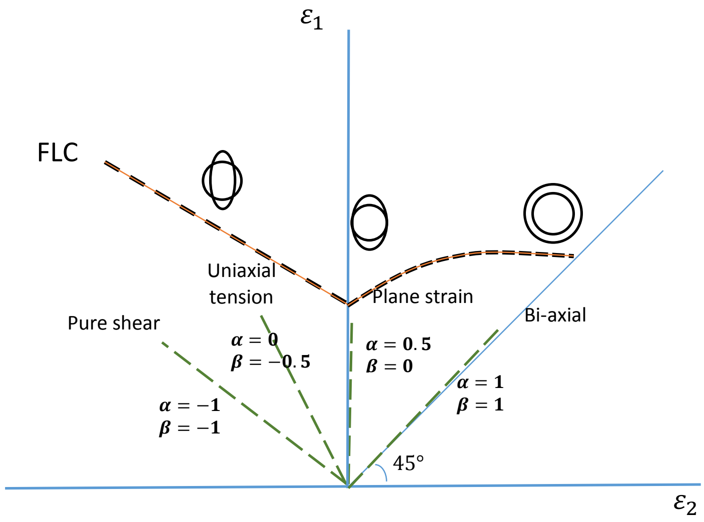

Figure 2.2: Schematic of FLC curve (adapted from [8]*)*

Where α corresponds to the loading path and β corresponds to deformation path (see Figure 2.2). Equations for loading path and deformation path, assuming proportional loading are:

$$\alpha = \frac{\sigma_2}{\sigma_1} \tag{2.3}$$

$$\beta = \frac{\varepsilon_2}{\varepsilon_1} = \frac{\partial \varepsilon_2}{\partial \varepsilon_1} \tag{2.4}$$

Where, σ_1 and σ_2 are the principal stresses as shown in Table 2.1 and ε_1 and ε_2 are the principal strains obtained from equations (2.1) and (2.2).

Another technique commonly used to obtain the major and the minor strains is to use a digital image correlation (DIC) system where multiple images of the specimen before, during and after the test are obtained in real-time and then are processed in order to calculate the strains. In order for DIC system to recognise the points on the sheet, the sheet is sprayed over with black and white colour (or any contrasting colours), also known as the speckle pattern. The DIC tracks the position of the same physical points shown in a reference image and a deformed image. To achieve this, square subsets of pixels are identified on the speckle pattern around point of interest on a reference image (see Figure 2.3a) and their corresponding location determined on the deformed image. The digital images are recorded and processed using an image correlation algorithm [9].

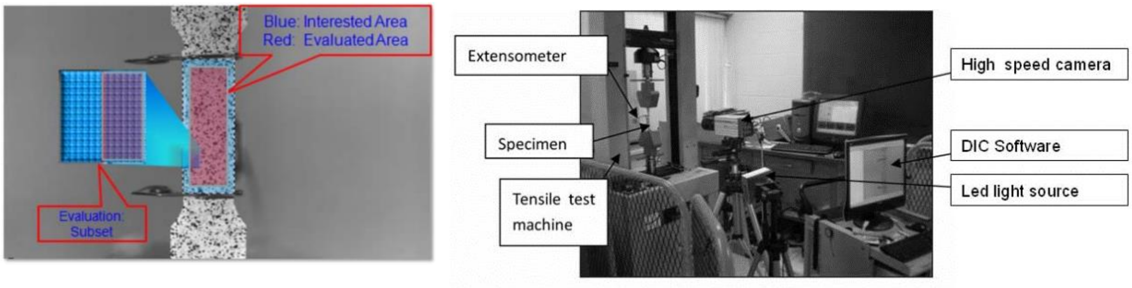

Figure 2.3: DIC, a) Prepared specimen with speckled pattern and b) Setup of a DIC system [9]

The characteristic modes of deformation are presented in Table 2.2 [8] for some conventional tests, which can be classified as uniaxial, plane-strain and biaxial deformations, depending on the mode of strain, states of strain and stress corresponding to each of the tests. A schematic representation of the specimens used in the tests are also presented.

Table 2.2: Formability test methods based on FLD (adapted from [8]*)*

Deformation mode	**Tests**	**Strain state**	**Stress state**	**Schematic representation**
Biaxial	Hydraulic Bulge	$\beta = 1$	$\alpha = 1$	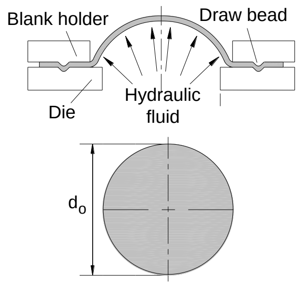
	Hemispheric expansion test	$\beta = [0,1]$	$\alpha = [0,1]$	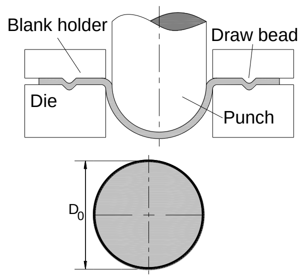
Plane deformation (and the transition region between the uniaxial deformation mode and biaxial deformation)	Nakajima	$\beta = [-0.5,0.5]$	$\alpha = [0,0.5]$	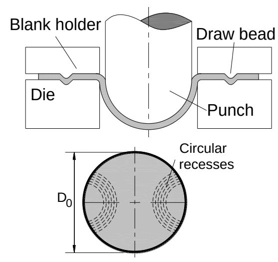
Plane strain deformation	Double notch tensile test	$\beta = 0$	$\alpha = 0.5$	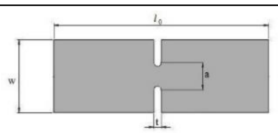

Uniaxial	Tensile Test	$\beta = -0.5$	$\alpha = 0$	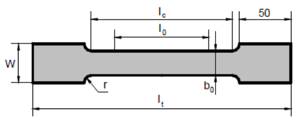
Mixed shear	Staggered test	$\beta = [-1, -0.5]$	$\alpha = [-1,0]$	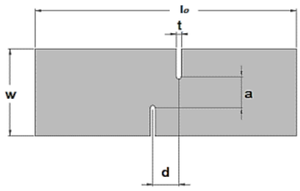
Pure Shear	V-slit shear specimen	$\beta = -1$	$\alpha = -1$	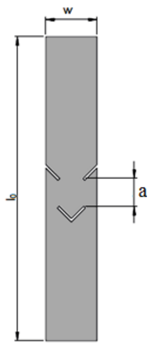
	C-slit shear specimen			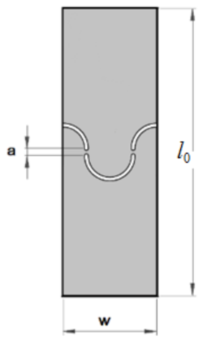

The most commonly used method to investigate the biaxial state of stress is the circular bulge test [10]. In the bulge test a circular sheet metal is fully clamped between two die surfaces and then is drawn within a die cavity by applying hydrostatic pressure on the inner surface of the sheet. The schematic representation of the process is shown in Figure 2.4. The die cavity diameter (2v) and initial sheet thickness (t_0) are constant parameters of most of the bulge testing. Instantaneous variables of biaxial test are: bulge pressure (p), dome height (a), bulge radius (ρ) and sheet thickness at the dome apex (t). Bulge test yields points in first quadrant of FLD with loading path of α =1 and deformation path of β =1.

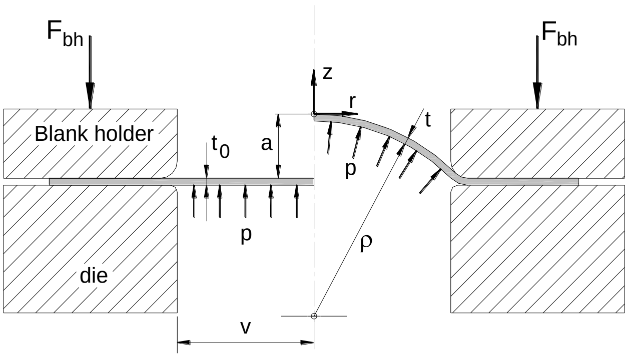

Figure 2.4: Schematic of hydroforming Bulge test [8]

To obtain the range of limiting strain points in the first quadrant of FLD, elliptical bulge test can be done. In this test instead of circular die, elliptical die is used to form the sheet metal [8]. Another test to obtain range of points between first and second quadrant of FLD is Nakajima test. In Nakajima test specimen with different widths (W) (as shown in Figure 2.5b) are formed till fracture using hemispherical punch [11]. By varying the specimen width, different deep draw and stretch forming conditions occur on the sheet metal surface (from a regular biaxial deformation to a simple tensile load) [12]. Thus the Nakajima test can be used to get strain points between biaxial and uniaxial region in FLD, these specimens provide points between tensile test and bulge test in FLD.

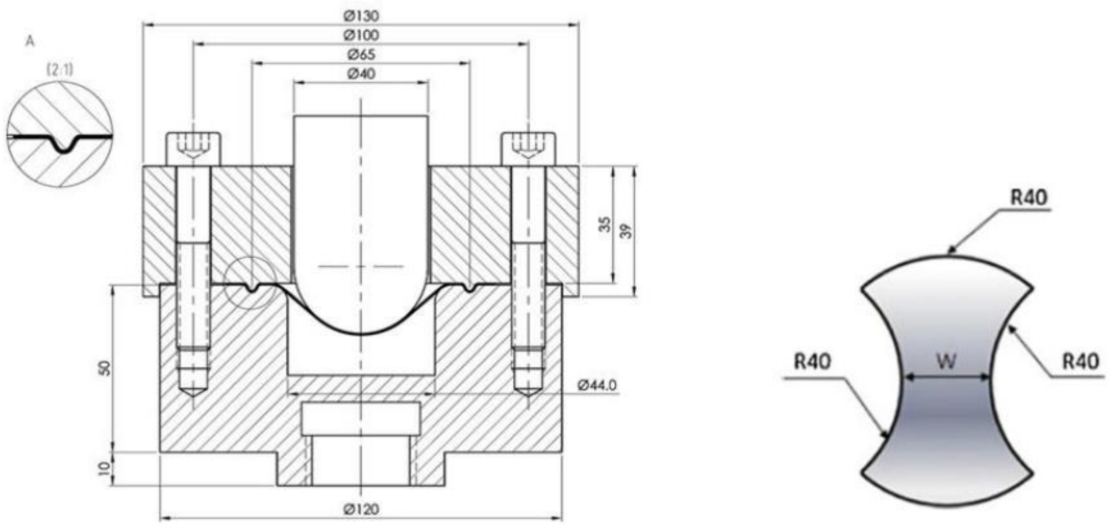

(a) (b)

Figure 2.5: Schematic representation of a) Nakajima test and b) Nakajima test specimen [11]

In order to obtain the limiting strain points in the uniaxial strain space the tensile test is used. The tensile test is also a mechanical characterization test, where the test specimen is subjected to a controlled tensile loading until fracture. The test is usually carried on a universal testing machine. The material properties that can be obtained from the tensile test are: ultimate tensile strength, maximum elongation, Young's modulus, yield strength, anisotropy coefficients. The specimen and the procedure are defined in ASTM E8 / E8M-13 (2013) standard [13]. The tensile test strain yields points in second quadrant of the FLD.

The fracture mechanics recognize three modes of crack deformation, which are: mode I, where the opening of the crack is due to normal tensile stresses (Figure 2.6a), mode II, due to in-plane shear stresses (Figure 2.6b) and mode III, due to out of plane shear stresses (Figure 2.6c) [8].

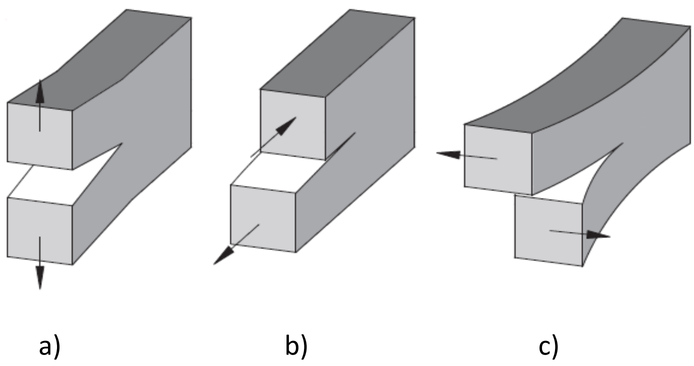

Figure 2.6: Mode of fracture; a) mode I, b) mode II, c) mode III [8]

The double notch tensile specimen (schematic representation of specimen is presented in Table 2.2) was initially used by Cotterell and Reddel [14] to calculate the fracture toughness where fracture occurs by mode I of fracture mechanics. The same specimen was later used to analyse fracture strains in plane strain deformation [5]. The double notch tensile test (DNTT) specimen is uniaxially loaded on universal testing machine till fracture. The fracture obtained from this test lie on the y-axis (plane strain) region, in the FLD.

In order to investigate limiting strains in the region between uniaxial zone and shear zone in FLD the staggered test specimen can be used. The staggered test specimen (schematic representation of specimen is presented in Table 2.2) was designed and used by Cotterell and Mai [15] to calculate the fracture toughness for fracture by mixed mode I&II of fracture mechanics. The specimen is uniaxially loaded on the universal testing machine till fracture. The specimen is designed such that it induces mixed mode I&II of fracture mechanics in the ligament. This specimen has previously not been used in literature to obtain fracture strains in the FLD. In the present study staggered specimen will be tested to obtain fracture strains in the FLD and the fracture strains are expected to lie between uniaxial zone and shear zone in the FLD.

The V-slit shear specimen (schematic representation of specimen is presented in Table 2.2) was used to calculate the fracture toughness when the fracture occurs by shear mode (fracture by mode II of fracture mechanics) and to obtain fracture strains in shear region of the FLD [5]. The V-slit shear specimen is loaded on universal testing machine till fracture. The slit in the specimen is designed in such a way that it induces shear mode of fracture in between the ligaments of the specimen. The C-slit shear specimen (schematic representation of specimen is presented in Table 2.2) described in the study of Shouler and Allwood [16] is a shear specimen that also induces shear mode of fracture in between the ligaments of the specimen. The fracture strains obtained from these specimens lie in the shear zone (loading path of $\alpha =$-1 and deformation path of $\beta =$-1).

2.1.2 Fracture limits

There are three major drawbacks of using the FLC in practise:

1. Sometimes fracture precedes necking. Embury and Duncan [3] verified through biaxial square stamping test that there are situations when the material fractures before undergoing necking.
2. The guidelines used in sheet metal design are mostly based on the reduction of critical thickness and not on the FLC [5].
3. The understanding of finite element programs that use ductile damage models to predict the onset of fracture requires data that comes from theories consistent with the relationship between fracture limits, ductile damage, and fracture toughness [8].

Thus, it is increasingly common to find other alternative of using the information provided by the fracture limits. The fracture limits are obtained by calculating fracture strains. Atkins [17] related the Fracture forming limit (FFL) to the critical thickness reduction and the ductile fracture criterion of McClintock [18] proposing the FFL as a '-1' slope line in FLD. Muscat-Fenech et al. [19] proposed the relation of this limit of formability to the fracture toughness in mode I, showing that the FLC is associated with the fracture resulting tensile stresses, eliminating the influence of the shear stresses in the thickness direction of the sheet. Shear fracture in the principal strain space was originally suggested by Marciniak [20], Figure 2.7 shows the proposed limiting loci for failure only by shear whatever the loading path. However, the forming limits suggested in Figure 2.7 were never accompanied by any phenomenological model or experimental evidence.

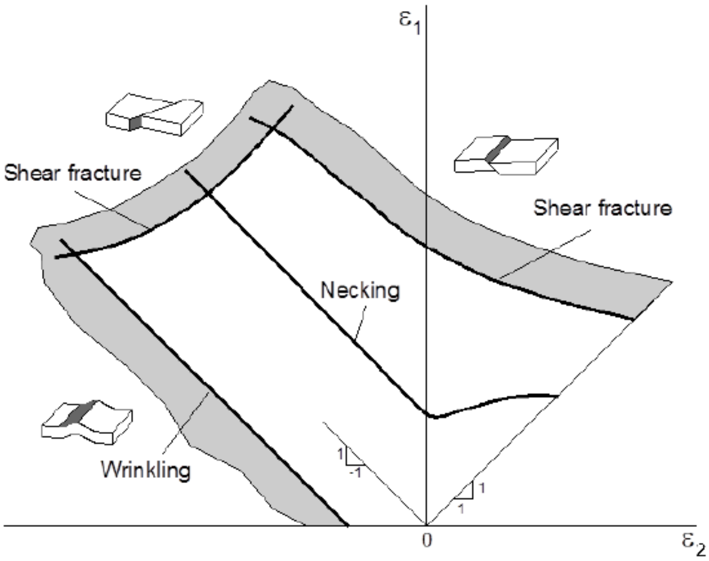

Figure 2.7: FLD suggested by Marciniak [20].

Until Atkins's study [17], the fracture limit was considered to be a parallel extension to the FLC. But it was this study that defined the FFL to be a straight line falling inclined from the second quadrant to the first quadrant in the FLD rather than a curve or band above the FLC. The formability limit by fracture had not been of interest to the sheet metal forming community because once a neck appears and spreads sideways under subsequent deformation, thinning will progress very fast under decreasing loads or pressures until the sheet cracks.

The Shear Fracture Forming Limit (SFFL) was investigated by Isik et al.[5], for AA 1050-H111 material, adding to the work of Atkins (1996) on FFL (Figure 2.8). In this investigation critical damage and plastic deformation was analysed in detail. SFFL is the limit by in-plane shear plastic deformation causing fracture. The investigation proposed that, theoretically the SFFL is a line with a '*+1*' slope and is perpendicular to the FFL. The dashed lines (in figure 2.8) represent the changes in strain paths towards plane strain conditions after necking.

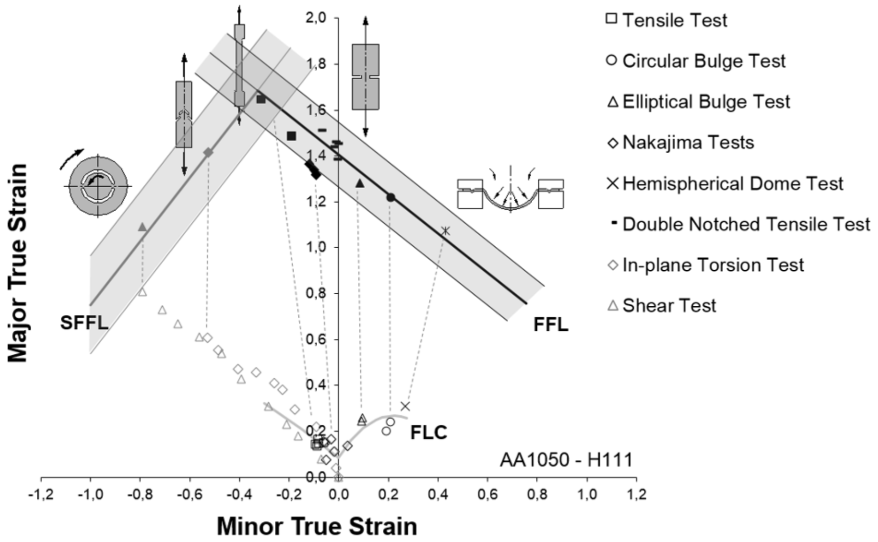

Figure 2.8: Results from study of Isik et al. [5]

Recent studies by Silva et al. [4] and Isik et al. [5] has showed the importance of Fracture forming limit line (FFL) and shear fracture forming line (SFFL). Silva et al. [21] confirmed the possibility of a fracture, without previous appearance of necking, and identified that the local deformation techniques create these possibilities.

The fracture strain points are determined using measurements of thickness and width (of fracture) before and after fracture (see Figure 2.9) [8].

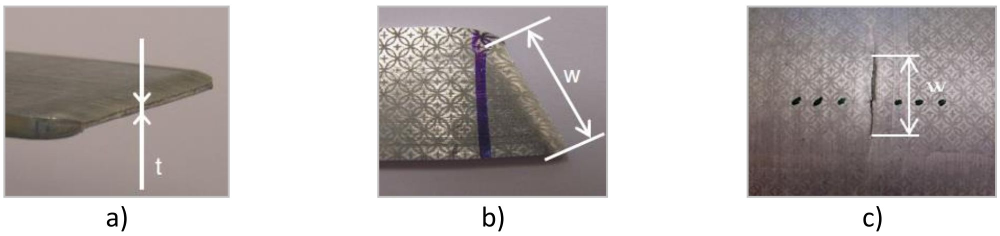

Figure 2.9:a) measuring the thickness after fracture; b) width after fracture; c) measuring width in case of Bulge [8]

The thickness strain (ε_t) is calculated according to following the expression,

$$\varepsilon_t = \ln\left(\frac{t}{t_0}\right) \tag{2.5}$$

Where t corresponds to the final thickness of the sheet and t_0 corresponds to the initial thickness of the sheet. The calculation of the width strain (ε_w) is obtained from the following equation,

$$\varepsilon_w = \ln\left(\frac{w}{w_0}\right) \tag{2.6}$$

Where w represents the final width of the fracture zone and w_0 is the initial width of the sheet. The third strain (longitudinal strain, ε_l) in the plane of the sheet, which is a direction perpendicular to the fracture, is obtained by means of the incompressibility equation:

$$\varepsilon_t + \varepsilon_w + \varepsilon_l = 0 \tag{2.7}$$

The equation of FFL can be derived from the equation of volume consistency,

$$\varepsilon_{1f} + \varepsilon_{2f} = -\varepsilon_{3f} \tag{2.8}$$

Where ε_{1f} is the first principal fracture strain, ε_{2f} is the second principal fracture strain and ε_{3f} is the thickness fracture strain. Thus it can be observed that the FFL is a straight line with '-1' slope.

The SFFL can be characterized by, [5]

$$\varepsilon_{1f} - \varepsilon_{2f} = \gamma_f \tag{2.9}$$

Where γ_f is maximum in-plane distortion.

The critical damage associated with FFL ($D^I{}_{crit}$), in terms of fracture strains can be written as,

$$D^I{}_{crit} = \frac{(1+r)}{3}\left(\varepsilon_{1f} + \varepsilon_{2f}\right) \tag{2.10}$$

Where r is the average value of the anisotropy coefficient $\bar{r}$ and D_{crit} can be obtained from [18], [22] as,

$$D^I{}_{crit} = \int_0^{\bar{\varepsilon}_f} \frac{\sigma_m}{\bar{\sigma}} d\bar{\varepsilon} \tag{2.11}$$

Where $\bar{\varepsilon}_f$ is the effective fracture strain, σ_m is average stress and $\bar{\sigma}$ is effective stress.

Similarly the critical damage associated in-plane shear ($D^{II}{}_{crit}$), in terms of fracture strains can be written as,

$$D^{II}{}_{crit} = \int_0^{\bar{\varepsilon}_f} \frac{\tau}{\bar{\sigma}} d\bar{\varepsilon} = \frac{(1+r)}{2(1+2r)}\left(\varepsilon_{1f} - \varepsilon_{2f}\right) \tag{2.12}$$

2.1.3 Fracture toughness in sheet metal

Specific Essential work of fracture (Fracture toughness, R) is the parameter that characterises fracture in the material. It can be considered as material constant even though it is thickness dependent [14]. The initial work of Cotterell and Reddel [14] introduced the methodology to calculate the specific essential work of fracture and the crack opening displacement (CTOD, δ) for mode I of fracture mechanics. In this case, a double notch tensile (DNTT) specimen (as shown in Figure 2.10a) was used. Total Work (W_t) done by the specimen till fracture is the sum of the work done over the plastic region (W_p), work done for elastic recovery (W_Γ) and essential work done for fracture (W_e). This total work can be represented as:

$$W_t = W_p + W_\Gamma + W_e \tag{2.13}$$

As in the case of DNTT, the experiment is performed till fracture and the ligament is completely yielded before fracture, so the work done for elastic recovery (W_Γ) can be neglected. If the total work equation (2.13) is divided by area (A) on both side, this leads to:

$$w = \frac{W_t}{A} = \frac{W_p}{A} + \frac{W_e}{A} = \frac{W_p}{A} + R \tag{2.14}$$

Where R is the specific essential work of fracture or fracture toughness. Same equation holds true if staggered DNTT specimen (Figure 2.10b) is used which induces fracture by mixed mode I & II of fracture mechanics [15].

It is found that the specific total energy is can be represented in terms of ligament size and this equation is linear [23]. Thus when the specific total energy is plotted against the ligament size the resultant graph will be a straight line.

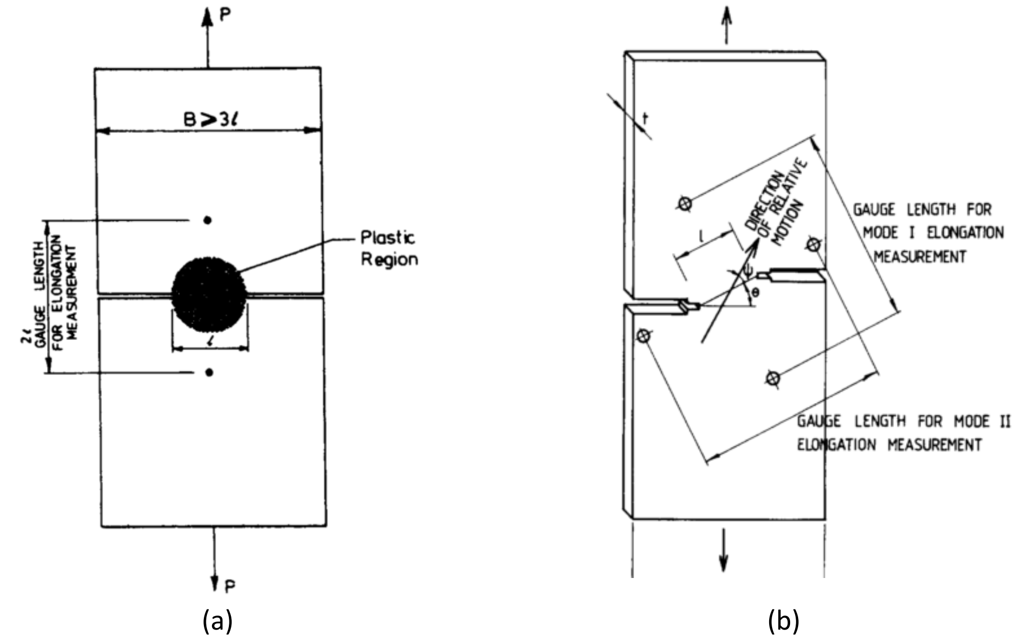

Figure 2.10: Specimen used by Cotterell et al. [15] *a) Deep notch tensile test specimen inducing fracture by mode I and b) Staggered DNTT specimen inducing mixed mode I&II fracture*

For ease of understanding, when fracture is induced by mode I of fracture mechanics, resulting fracture toughness is abbreviated as R_I when fracture is induced by mode II of fracture mechanics, resulting fracture toughness is abbreviated as R_{II} and when fracture is induced by mixed mode I & II of fracture mechanics, resulting fracture toughness is abbreviated as $R_{I\&II}$. In case of sheet metal forming fracture by mode III of fracture mechanics is very rare and is not often used.

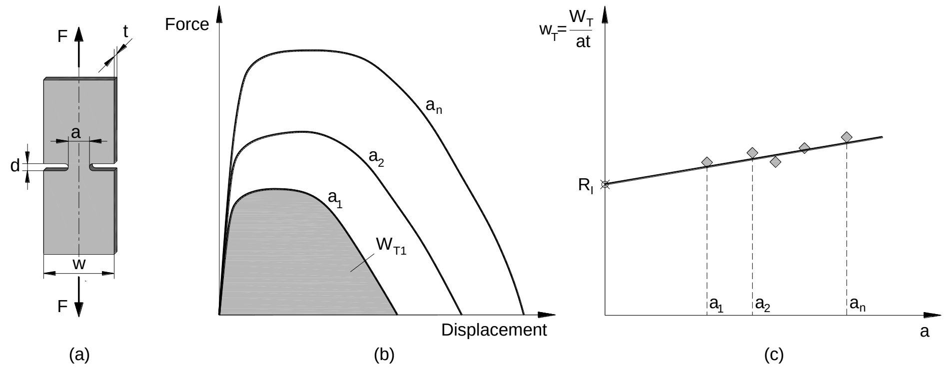

Figure 2.11: Method and procedure used for determining fracture toughness R. a) Schematic representation of a double notch tensile test specimen loaded in tension. b) Schematic evolution of the tensile force with displacement for test specimens with different ligament's size (a). c) Determining fracture toughness R from extrapolation of the amount of energy per unit of area w that is needed to create a new unit surface [24]

Figure 2.11 shows the procedure to calculate the fracture toughness [24]. Various ligament sizes (a), are used between the limits:

$$\frac{1}{\pi}\left(\frac{K}{\sigma_y}\right)^2 > \mathrm{a} > 5t \quad (2.15)$$

Where, K is the stress intensity factor in the given mode, σ_y is the yield stress and t is the sheet metal thickness.

The determination of fracture toughness mode II of fracture was investigated by Isik et al. [25] and Silva et al. [23]. The methodology to calculate essential work of fracture in mode II is similar to that of in mode I and is schematically represented in Figure 2.12.

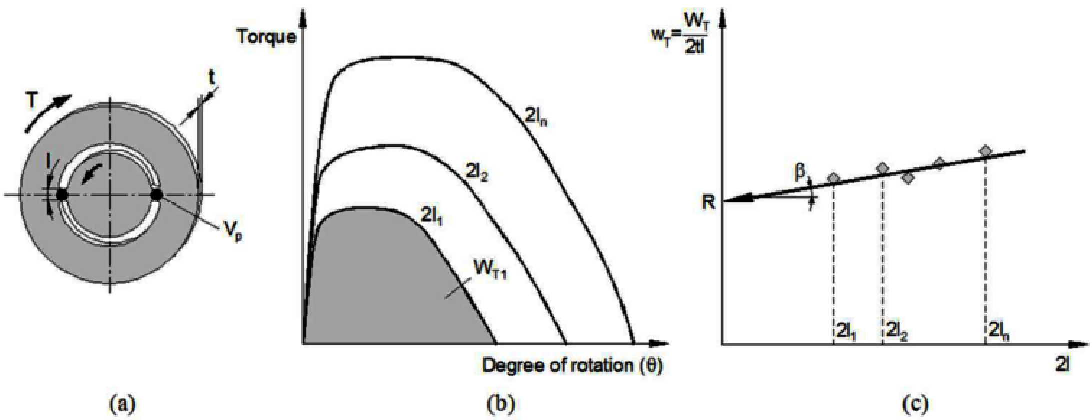

Figure 2.12: Method and procedure for determining fracture toughness R in crack opening mode II. (a) Schematic representation of a double-notched torsion test specimen; (b) Schematic evolution of the torque with degree of rotation for test specimens with different ligaments; (c) Determination of fracture toughness R from extrapolation of the total amount of energy per unit of area. [25]

Silva et al. [23] discussed the concept of plastic flow, ductile damage and void coalescence and growth to include fracture toughness in two different crack opening modes i.e. mode I and mode II. Figure 2.13 shows the schematic link of above mentioned parameters.

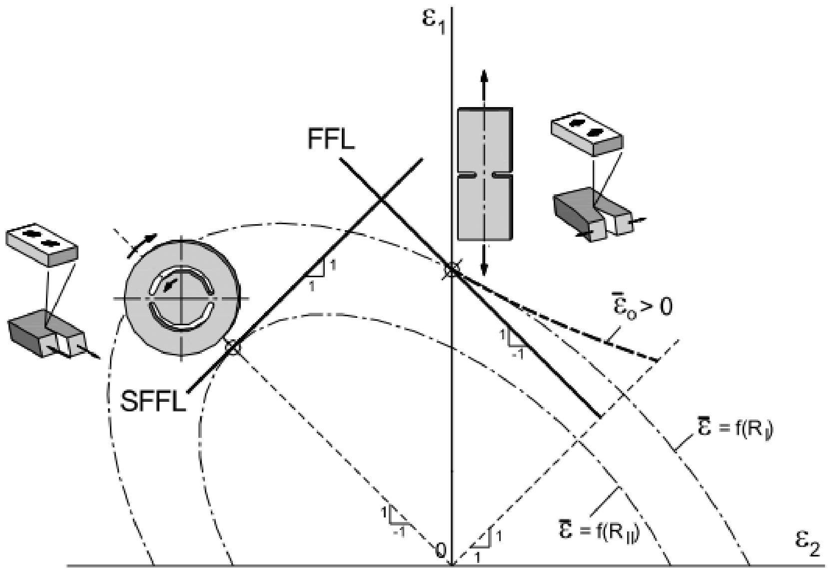

Figure 2.13: Schematic link between plastic flow, void coalescence and growth, ductile damage, crack opening modes, and fracture toughness in sheet metal forming. [23]

Atkin and Mai [26] proposed the possibility of predicting the fracture strain or the workability index (ε_{1f}) using the fracture toughness. Following equation was derived for effective strain ($\bar{\varepsilon}_f$),

$$\bar{\varepsilon}_f \; = \; [R(n+1)/(\sigma_0 h)]^{-1/(n+1)} \tag{2.16}$$

Where, *R* is the specific essential work of fracture or the fracture toughness in a given mode, *n* is the work-hardening coefficient, σ_0 is the strength coefficient and *h*, is the height of the necked down region. This equation is valid only when the Ludwick-Holloman equation is used. Effective stress ($\bar{\varepsilon}_f$), can also be expressed in terms of the major necking strain; ε_{1n} (from FLC) and the major fracture strain ε_{1f} (from FFL) as:

$$\bar{\varepsilon}_f \; = \frac{2}{\sqrt{3}}\varepsilon_{1n}\left(1+\frac{1}{N}+\frac{1}{N^2}\right)^{1/2} + \frac{2}{\sqrt{3}}\left(\varepsilon_{1f} + \varepsilon_{1n}\right) \tag{2.17}$$

Where, $N = \varepsilon_1/\varepsilon_2$ i.e. ratio of the major and the minor strains. Value of $\bar{\varepsilon}_f$ can be calculated using *R*, and using value of $\bar{\varepsilon}_f$, major strain at the onset of fracture (ε_{1f}) can be estimated.

The detailed analysis of the relationship between fracture strains and fracture toughness was conducted by Muscat-Fenech et al. [19]. The effect of anisotropy on the fracture toughness and the prediction of fracture strain was investigated. The effective strain equation which takes anisotropic factor, *r* in consideration is given by:

$$\bar{\varepsilon}_f = \{[2(1+r)]^{1/m}/2\}\left[|\varepsilon_1+\varepsilon_2|^{m/(m-1)} + (1+2r)^{-1/(m-1)}\left|(\varepsilon_1+\varepsilon_2)^{m/(m-1)}\right|\right]^{(m-1)/m} \quad (2.18)$$

Where, m is the power index. Thus finding value of R will be useful in predicting the fracture strains.

2.2 Incremental forming

In the conventional sheet metal forming process the blank sheet is formed against a die (positive geometry of the part) using a punch (negative geometry of the part). The cost of these punch and die is the major contribution to the total cost of the production. If the required component batch size is small, the conventional sheet metal forming is not appropriate. For these situations incremental forming is best solution. In incremental forming the need for the conventional die and the punch is eliminated thus also reducing the overall tooling cost. In incremental forming the desired shape from the sheet metal blank is achieved by series of small incremental deformations.

One of the oldest incremental sheet metal forming technique is Hammering. Conventionally it was done manually, and recently it has evolved into CNC Hammering (see Figure 2.14). Now-a-days a robot is used, that controls the movement of the tool, the blank sheet is clamped in a support frame, and the robot punches in a circular trajectory the sheet descending a small step each round [27].

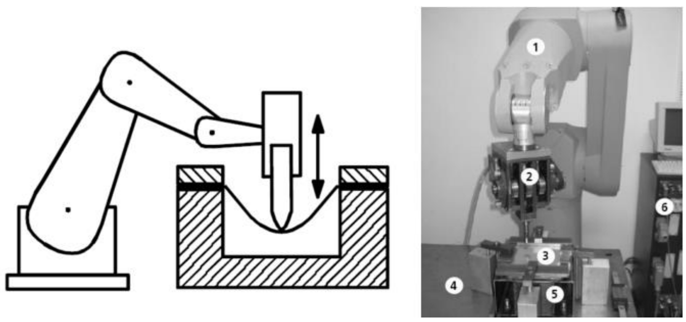

(a) (b)

Figure 2.14: Incremental hammering process, a) Schematic representation, b) Industrial robot [27]

The patent of Leszak [28] in 1967, is considered to be the first setup to be categorized under numerically controlled incremental sheet forming category. In this patent the process for manufacturing of disc-like or cup-like products from sheet metal is described. The blank rotates and a vertical displacement is created by local bending caused by pushing the sheet into an elastic medium by a roller. This process is more specifically termed as Spinning [29]. Berghahn et al., [30] in 1967 patented a process for manufacturing disc-like products from the sheet metal. The authors named this process as *dieless forming* in which the blank is clamped and rotates, while a roller moves inward along radial line, thus describing a contour that forms the final shape; which is again spinning process.

Metal spinning is a forming process that allows the manufacturing of symmetric shapes without the need of expensive dies. The spinning method involves clamping a sheet metal blank against a chuck on a spinning lathe. By using a solid rod, or roller, forming tool, the metal is gradually worked over the chuck surface. The chuck, otherwise known as a mandrel, is machined to the shape of the desired part. This gives an accurate surface for the sheet to be formed. This process is also known as conventional spinning [6]. If the roller tool is programmed to follow the profile of the part surface such that the formed component maintains a constant thickness but different than the initial blank thickness then the process is called as Shear spinning. Due to the nature of the process, the shear spinning will have two actions: 1) bending against the mandrel; and 2) applying downward force while rotating. Due to this, in shear spinning the thickness of final component will vary with respect to original blank thickness and this “thinning” is quantified using the Sine Law:

$$t_f = t_i \sin \propto \tag{2.19}$$

Where, t_f is the final thickness, t_i is the initial thickness and $\propto$ is the forming angle as seen in Figure 2.15.

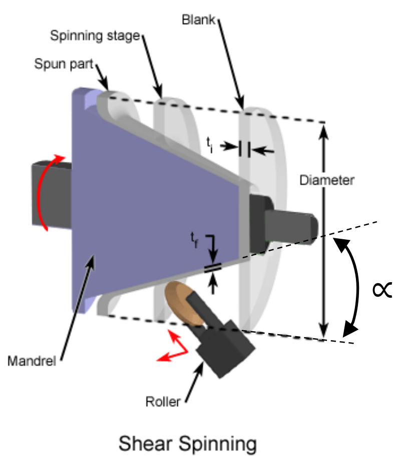

Figure 2.15: Schematic of shear spinning with thickness reduction [31]

One of the major draw-back of spinning is that, only axis-symmetric geometries can be formed using this process. This limitation is eliminated in single point incremental forming.

The term "*Single Point Incremental Forming (SPIF)*" was first coined by Jeswiet et al., [6] and in the same study they did a comprehensive review for Asymmetrical Incremental Forming, of which SPIF and TPIF are the sub-category.

The current concept of SPIF was first proposed by Mason [32] in 1978. He proposed using a single spherical roller with three axes control to generate shaped surface with sheet metal clamped rigidly at edge with some backing medium. Iseki et al. [33] in 1989 started their study on CNC milling machine. The schematic from their study is shown in Figure 2.16.

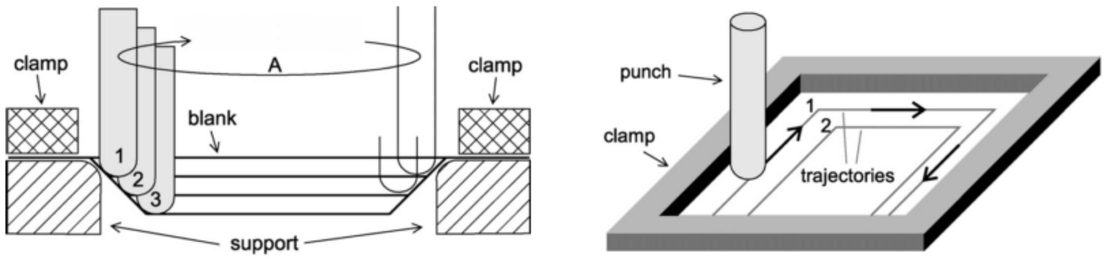

Figure 2.16: Schematic of SPIF on CNC milling machine [33]

Kitazawa [34] in 1993 had later improved to the Incremental Stretch Expanding process where a CNC lathe machine is used with a steel rod hemispherical forming tool tip and where the blank is clamped on the chuck of the lathe machine. Incremental Forming with Counter Tool (IFCT) is a variant of SPIF that utilizes two forming tools on both sides of the sheet. The counter tool makes a trajectory similar to that of the main forming tool [35]. The schematic representation of IFCT is shown in Figure 2.17.

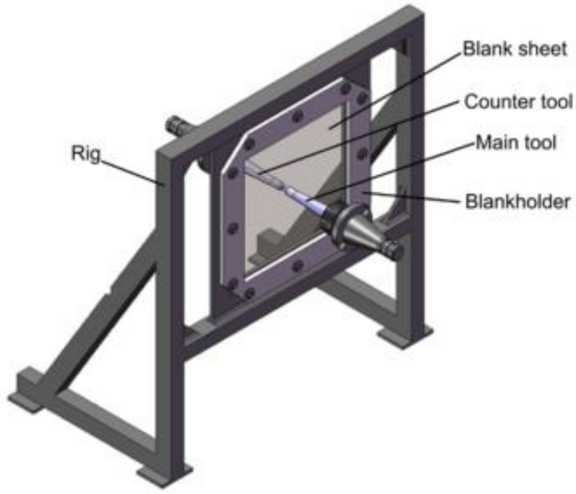

Figure 2.17: Schematic representation of Incremental forming with counter tool (IFCT)[35]

In 1994, Matsubara [36] had developed an Incremental Backward Bulge Process, where the sheet is clamped on downward moveable rig, the centre of blank is supported by a post. The forming tool is controlled by a CNC providing the tool movement that describes the trajectory to obtain the final symmetrical or non- symmetrical geometry of the desired part. This process was later termed as "*two point incremental forming (TPIF)"*. Figure 2.18 shows the schematic representation proposed by Matsubara.

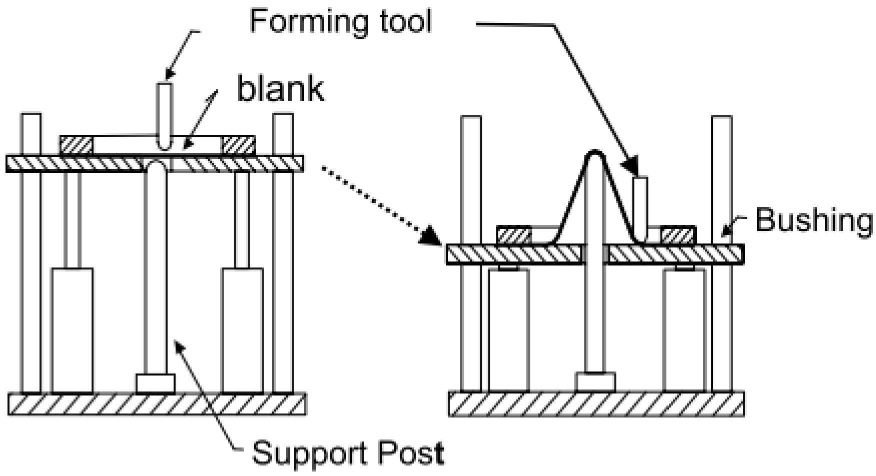

Figure 2.18: Two Point Incremental forming (TPIF). [36]

In TPIF, the sheet is clamped rigidly around its edges with a blank holder that moves vertically. The forming tool moves along a trajectory on the outer surface of the sheet part, from the top to the bottom of the geometry [37]. TPIF improves the surface quality and geometrical accuracy of the tool path [38]. Figure 2.19 shows schematic difference between SPIF and TPIF.

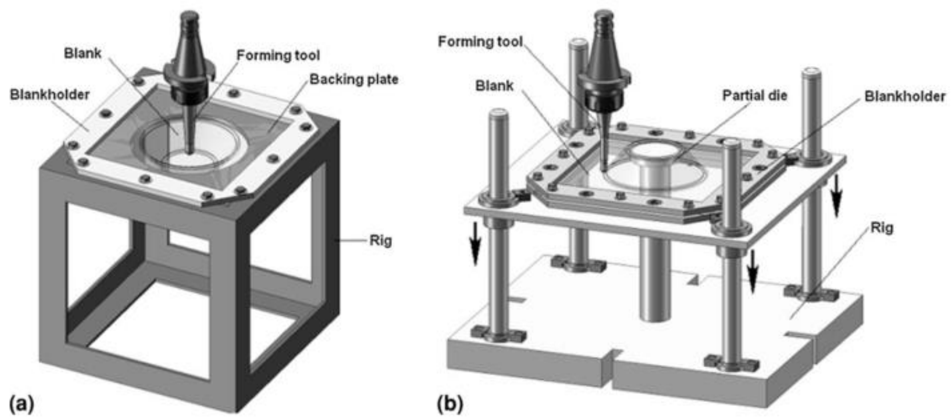

Figure 2.19: Schematic difference between: a) SPIF and b) TPIF [37]

There are two types of TPIF: one that uses partial die (see Figure 2.20a) and other that used full die (see Figure 2.20b) [39].

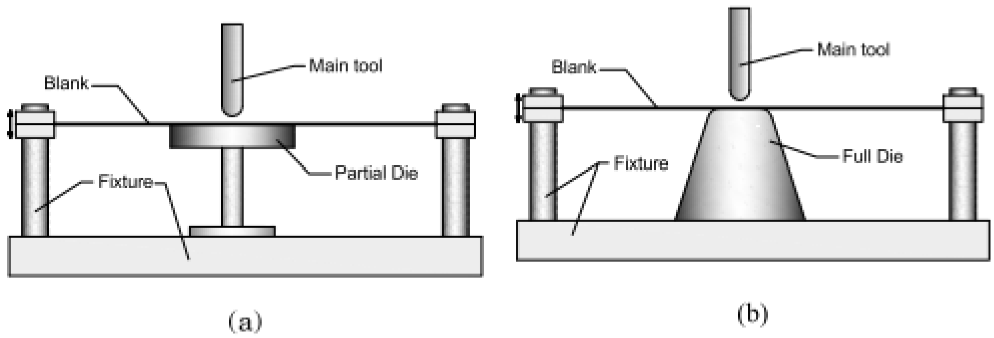

Figure 2.20: Schematic representation of TPIF: a) use of partial die; b) use of full die [39]

As the incremental sheet metal forming is finding its way in the industrial sector, it has raised the need to develop specialised machines that can perform incremental forming. Amino was probably the first industry to build its own specialised incremental forming machine [29]. Other specialised incremental forming setup includes the Roboforming and the Electromagnetic SPIF.

The roboforming principle is based on flexible shaping by means of freely programmable path- synchronous movements of two industrial 6-axis robots (see Figure 2.21) driving universal work piece-independent forming tools [40].

Figure 2.21: Roboforming [27]

Another emerging specialised incremental forming setup is the Electro-magnetic incremental forming. This method makes use of a small coil and a small discharge energy to cause workpiece to locally deform at a high speed. Finally, all local deformations accumulate into large parts [41]. The schematic for this method is shown in Figure 2.22.

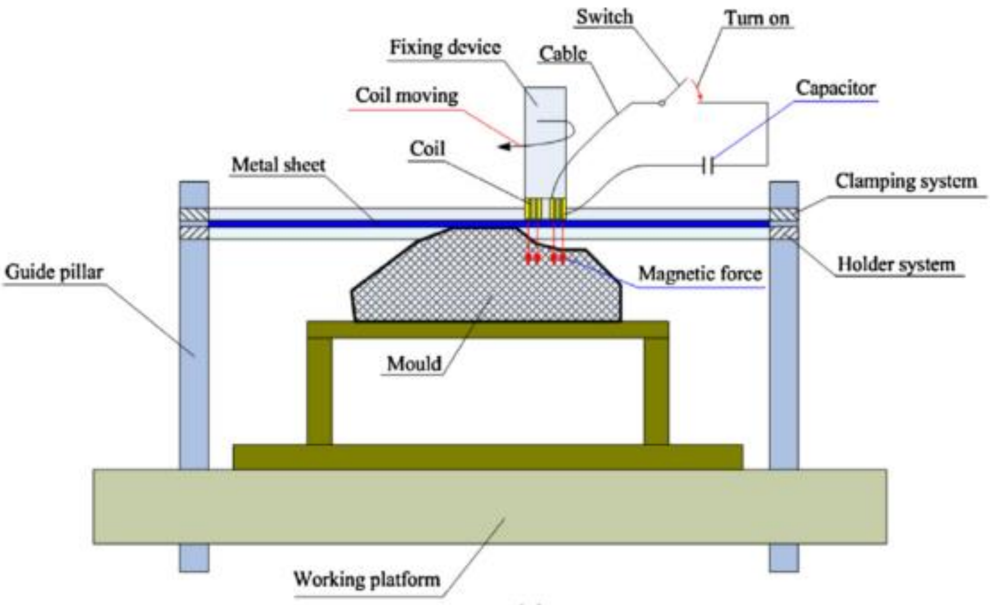

Figure 2.22: Schematic of Electromagnetic incremental forming [41]

If in SPIF, instead of solid tool, water (in jet form) is used to deform the blank, this methodology is called as water-jet incremental forming [42]. The schematic representation of this process is given in Figure 2.23. The water-jet SPIF when compared to SPIF is better in terms of tooling cost, surface integrity but SPIF is better in terms of forming accuracy and energy consumption [43].

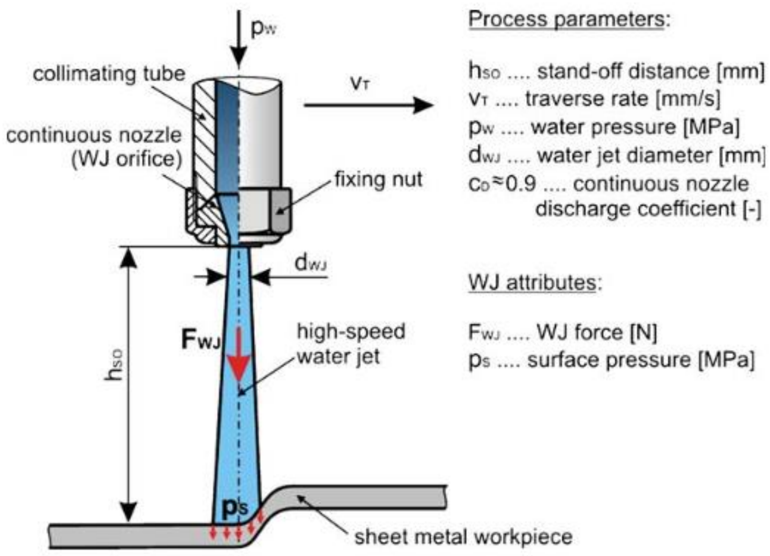

Figure 2.23: Schematic of Water jet incremental forming [43]

If incremental forming is performed at elevated temperature it led to advantages like reduced forming force and increased formability. This increased temperature permits to activate new sliding planes and dramatically increase the material formability [44]. The heating source to the blank can be from hot blowers [44], electric heating [45], or laser assisted [46]. Schematics of the laser and the electric assisted incremental forming at elevated temperature are shown in Figure 2.24.

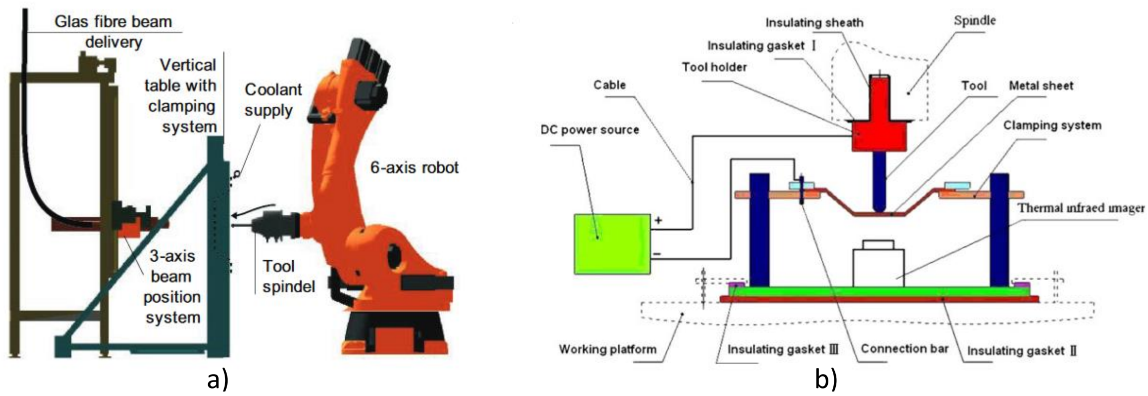

Figure 2.24: a) laser assisted SPIF [46]*; b) Electric hot SPIF* [45]

Magnesium alloy AZ31 has good properties to be a good structural component as the strength to weight ratio is very high. Unfortunately, this alloy is also brittle in nature which limits its formability. But at elevated temperature the formability improves and this alloy can be used in SPIF [44]. Thus warm incremental forming is used when the material is hard to form at room temperature. This technique increases the formability limits of the material and improves the dimensional accuracy [45].

2.3 Single Point Incremental Forming

In Incremental Sheet Forming (ISF) the desired shape of sheet is obtained by series of incremental plastic deformation. This is achieved by a numerical controlled forming tool. When no primary die or die support is used it is termed specifically as Single Point Incremental Forming (SPIF). Figure 2.25 shows a schematic representation of the SPIF process [4]. The motivation to have such process was to achieve a sheet forming technique that needs no die, uses a universal tool and can be used for prototyping of sheet metal.

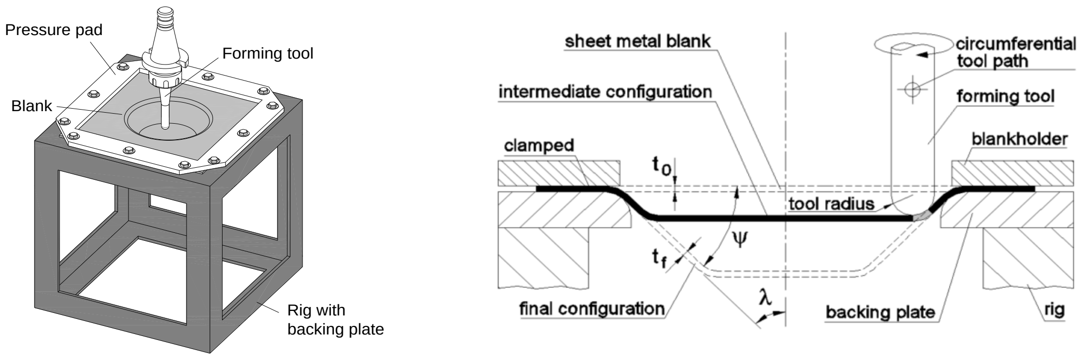

Figure 2.25: Schematic representation of Single Point Incremental Forming [4]

2.3.1 Formability limits for Single Point Incremental forming

In order to evaluate the formability limits in SPIF the truncated conical shaped geometry is formed till fracture. This benchmark truncated conical shaped geometry was proposed by Hussain et al. [47] which was later used by others to determine the formability limits in SPIF for plane strain deformation condition. The geometry is shown in Figure 2.26.

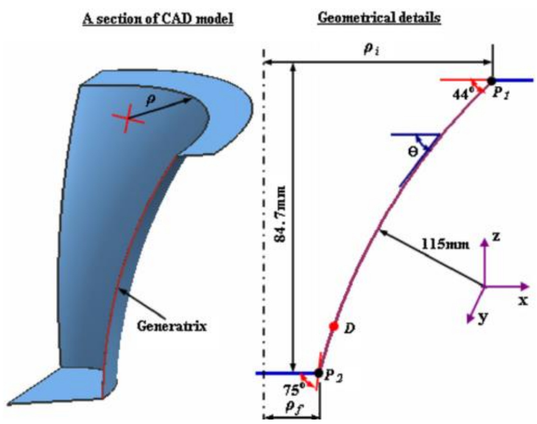

Figure 2.26: Truncated conical shaped component: CAD model and geometry [47]

Formability limits in case of Incremental forming is higher than the conventional forming processes and the limiting curve extends beyond the conventional FLC [6]. This increase in the formability is because of the fact that SPIF induces local plastic deformation and the necking is absent. Recent studies by Silva et al. [4] and Isik et al. [5] had shown the importance of the Fracture forming limit line (FFL) and the shear fracture forming line (SFFL) especially in the field of incremental sheet metal forming. The formability limits in incremental sheet metal forming are above the FLC. To plot these limits in the principal strain space, conventional tests are used [5] and SPIF geometries are used to validate these limits.

Recently, Soeiro et al. [48] proposed a new view for the formability limits for the sheet metal deformation processes by incremental forming. This asserts that the plastic deformation and the sheet fracture results from the competition between the reduction of thickness resulting from tensile stresses (mode I of the fracture mechanics) and the critical distortion caused by shear stresses in the plane of the sheet (mode II of the fracture mechanics) (see Figure 2.27). This conclusion is based on analytical work and experimental work. The analytical work was based on the development of a theoretical model [49] to determine the stress and strains that develop during the process of incremental forming of sheet metal. The experimental work consisted of performing incremental forming tests, which resulted in fractures due to shear stresses.

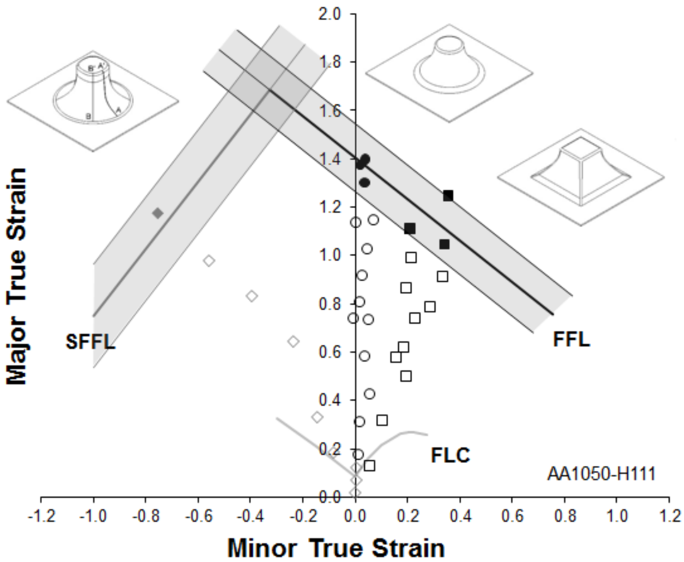

Figure 2.27: Results from Soeiro et al. [48]

2.3.2 Experimental setup

In principle, to carry out SPIF, one needs a forming tool that can be numerically controlled to form the rigidly clamped sheet metal. The forming tool can be controlled by a specialised robotic arm [40] or any CNC machining centre [6]. The tool trajectory can be achieved using a commercial CAD-CAM tool path generation.

The geometry of the forming tools have effect on the process and will be discussed later (in section 2.3.4). Figure 2.28 shows different geometries of forming tool used in SPIF: Flat end tool [50], hemispherical end tool [50], spherical end tool [51] and oblique roller tool [52].

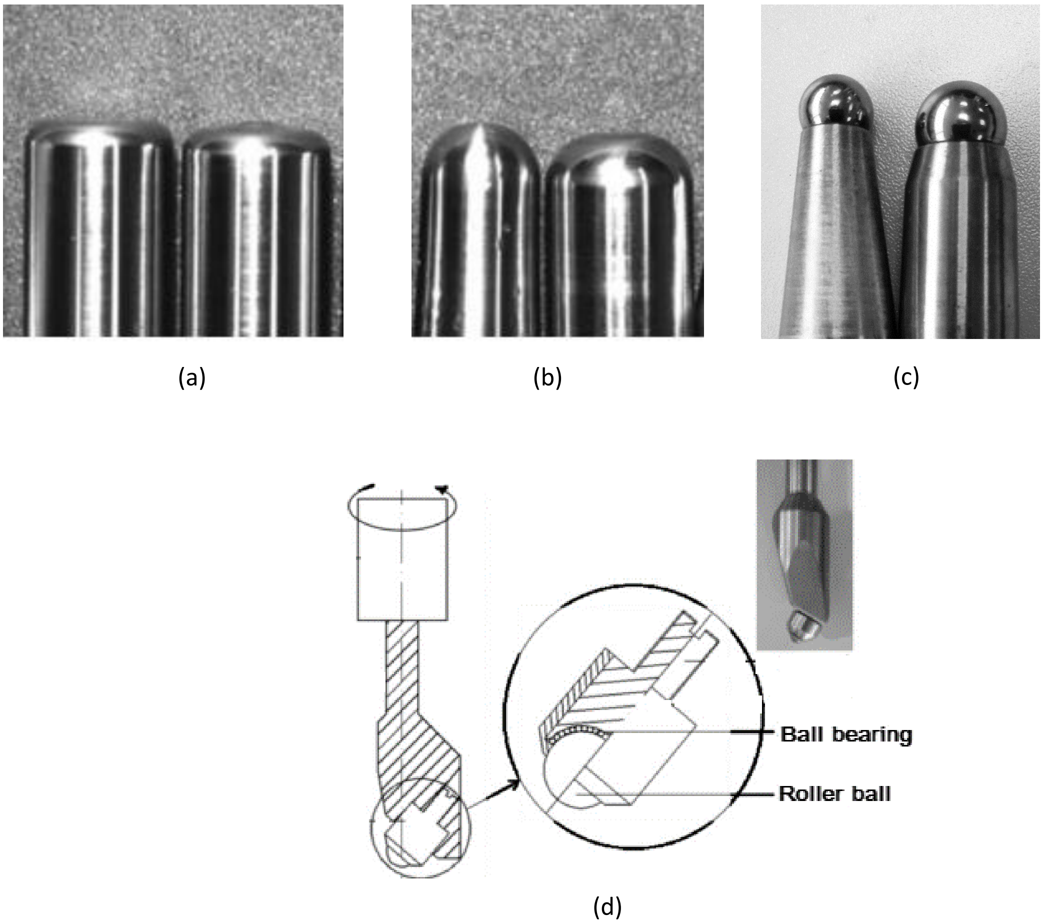

Figure 2.28: Types of forming tools used in SPIF: a) flat end forming tool (b) hemispherical end forming tool [50] *(c) Spherical end forming tool* [51] *and (d) Oblique roller forming tool* [52]

The sheet metal has to be rigidly clamped and for this, usually a rig is used with backing plate and the sheet is clamped between the rig and the blank-holder [6].

2.3.2 Advantages and disadvantages

The following advantages makes SPIF definitively convenient for prototype, custom, or even small batch production [53].

- ✓ Use of simple and universal forming tooling, thus no need of conventional dies, which also eliminates associated costs related to dedicated die and punch;
- ✓ A CNC machining centre can be used as machine-tool;
- ✓ When conventional CNC machine is used, the parts can be directly generated from CAD enabling easy and quick design changes;
- ✓ Lower forming forces involved due to incremental nature of the process;
- ✓ The part's dimension is only limited by the machine tool and not by the process;
- ✓ Increase in formability over conventional stamping and deep drawing sheet metal forming processes [49].

As is the case with all the processes, each one have pros and cons, same is the case with SPIF. Following are its disadvantages:

- ✗ Considerable thinning of the formed component [4];
- ✗ The forming time is considerably higher than conventional forming due to the incremental nature of the process;
- ✗ Complex strategies and/or multi-stages have to be used to achieve vertical/straight walls [54];
- ✗ Springback effect is significant and difficult to compensate [55].

2.3.3 Deformation and fracture Mechanism

The formability limits obtained in SPIF is above the FLC in comparison with conventional forming process. The reason for this increase is studied and the theories are proposed by many researchers. The major theories are discussed in this section.

Martins et al. [49] and Silva et al. [56] in 2008 suggested a theoretical model for the deformation mechanism in single point incremental forming. In these studies the physics of fracture at the transition between the inclined wall and the corner radius of the sheet was studied. The state of strain and stress in the small localized deformation was studied (see Figure 2.29). This theory is based on enhance – membrane analysis.

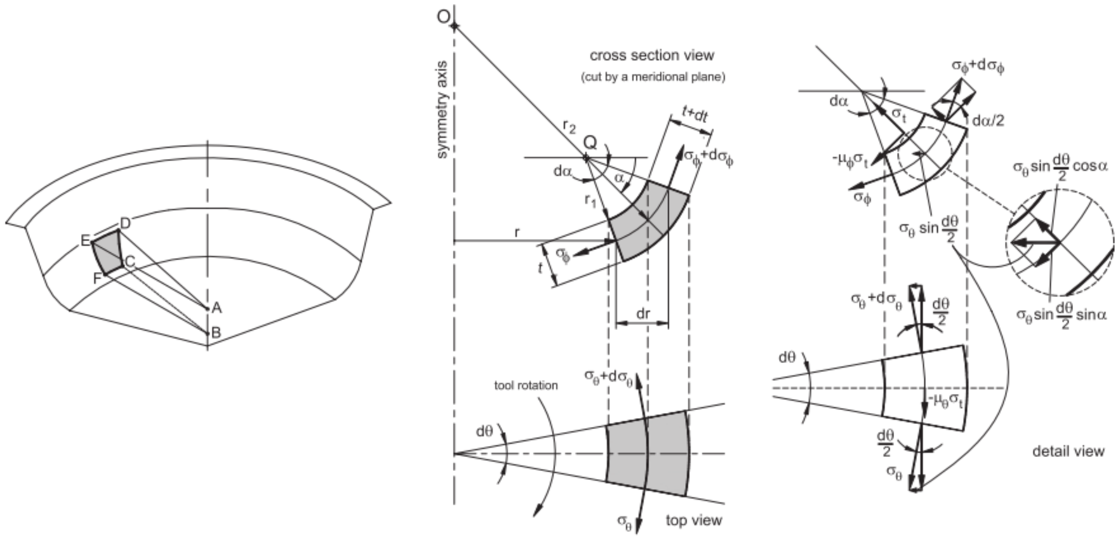

Figure 2.29: State of stress and strain for an element near fracture zone. [56]

The model is based on the experimental observation of the smear-mark interference between the tool and the surface of the sheet and is built upon membrane analysis. The analysis of the likely mode of material failure at the transition zone between the inclined wall and the corner radius of the sheet is conducted.

The cracks developed in the formed truncated conical shape and truncated pyramid shape (formed till fracture) are observed to be opened by meridional tensile stresses corresponding to the fracture by mode I of fracture mechanics. The Table 2.3 provides the strains and stresses along the principal directions that are derived from the analytical assumptions of SPIF.

Table 2.3: Results for state of stress and strain in localised plastic zones [56]

	Assumption	**State of strain**	**State of stress**	**Hydrostatic stress**
Flat and rotation symmetric surfaces	Plane strain conditions. (area marked by A and B in Figure 2.30)	$d\varepsilon_\emptyset = -d\varepsilon_t > 0$ $d\varepsilon_\theta = 0$ $d\varepsilon_t < 0$	$\sigma_\emptyset = \sigma_1 = \frac{\sigma_y}{1 + t/r_{tool}} > 0$ $\sigma_\theta = \sigma_2 = \frac{1}{2}(\sigma_1 + \sigma_3)$ $\sigma_t = \sigma_3 = \frac{-\sigma_y\, t}{t + r_{tool}} < 0$	$\sigma_m = \frac{\sigma_y}{2}\left[\frac{r_{tool} - t}{r_{tool} + t}\right]$
corners	Equal bi-axial stretching. (area marked by C in Figure 2.30)	$d\varepsilon_\emptyset = d\varepsilon_\theta > 0$ $d\varepsilon_t < 0$	$\sigma_\emptyset = \sigma_\theta = \sigma_1 = \frac{\sigma_y}{1 + 2t/r_{tool}} > 0$ $\sigma_t = \sigma_3 = \frac{-2\sigma_y\, t}{2t + r_{tool}} < 0$	$\sigma_m = \frac{2\sigma_y}{3}\left[\frac{r_{tool} - t}{r_{tool} + t}\right]$

Inclined walls	Uniaxial tension	$d\varepsilon_\emptyset > 0$ $d\varepsilon_t = d\varepsilon_\theta < 0$	$\sigma_{\emptyset D} = \sigma_{\emptyset C}\dfrac{r_c}{r_D} < \sigma_y$ $\sigma_\theta = \sigma_t = 0$	$\sigma_m = \dfrac{\sigma_\emptyset}{3}$

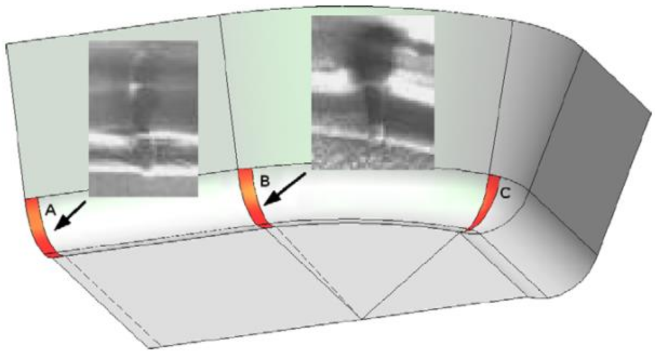

Figure 2.30: Instantaneous deformation zone and contact area between forming tool and workpiece during SPIF [49]

In 2009, Jackson and Allwood [57] proposed a stretching and shear theory in SPIF and TPIF. Strain deformation through the thickness of the specially prepared copper sheet were measured and compared with conventional stamping. The measurements showed that the deformation mechanisms of SPIF and TPIF are stretching and shear in the plane perpendicular to the tool direction, with shear in the plane parallel to the tool direction. Strain components increase on successive laps, and the most significant component of strain is shear parallel to the tool direction. Increasing stretching and shear perpendicular to the tool direction account for differences between the sine law prediction and measured wall thickness. This observed mechanism differed from the previously assumed pure shear mechanism.

In 2009, Emmens and Boogaard [58] presented a theory that the increased formability in SPIF is similar to that of increased formability seen when specimen is continuously bending under tension (CBT). The setup of this experiment is shown in Figure 2.31. In this test the sheet metal is uniaxially loaded and is simultaneously bend using three rollers as seen in Figure 2.31. Materials DC04, DC06, AA5182 and AA 6016 were used for this experiment. The authors found that this test replicates the local deformations phenomenon similar to that of SPIF. However for CBT it is observed that the bending radius has to be reduced significantly for better correlation.

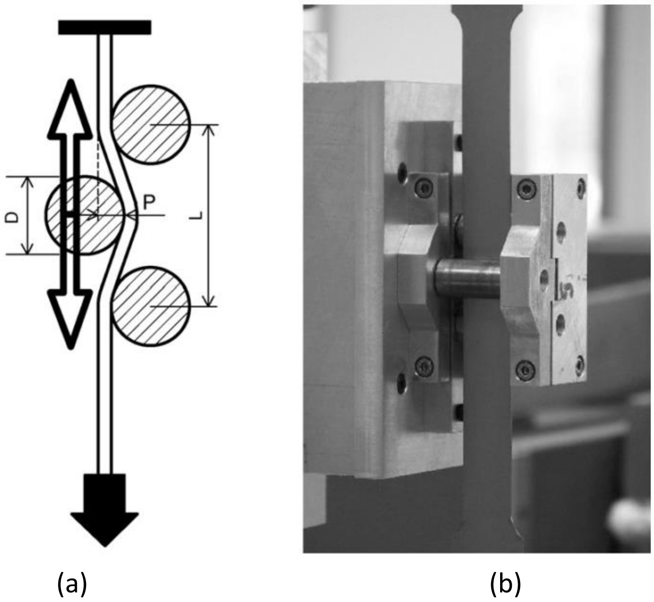

Figure 2.31: a) Schematic representation of continuous bending under tension test; b) Test setup [58]

In 2012, Malhotra et al., [59] developed a fracture model and used the finite element to predict the fracture in a truncated cone and a truncated pyramid shaped components. This model showed good agreement with the experiment. In this study along with fracture prediction, finite element deformation mechanism was compared with that of conventional forming. It was proposed that through the thickness shear and local bending of sheet around tool play an important role in fracture. Due to high bending around the tool, a greater damage accumulation is achieved in SPIF. This phenomenon led to the hypothesis of the "*noodle theory*". This theory proposes that the local nature of deformation is the primary reason for increased formability. This theory is schematically represented in Figure 2.32. The fracture history of conventional forming is presented in Figure 2.32a, Figure 2.32b and Figure 2.32c. In conventional forming the thinning is concentrated in single location and the fracture due to necking occurs at the same location. In case of SPIF the thinning deformation is distributed (Figure 2.32e) throughout the specimen due to the local incremental deformation nature of SPIF.

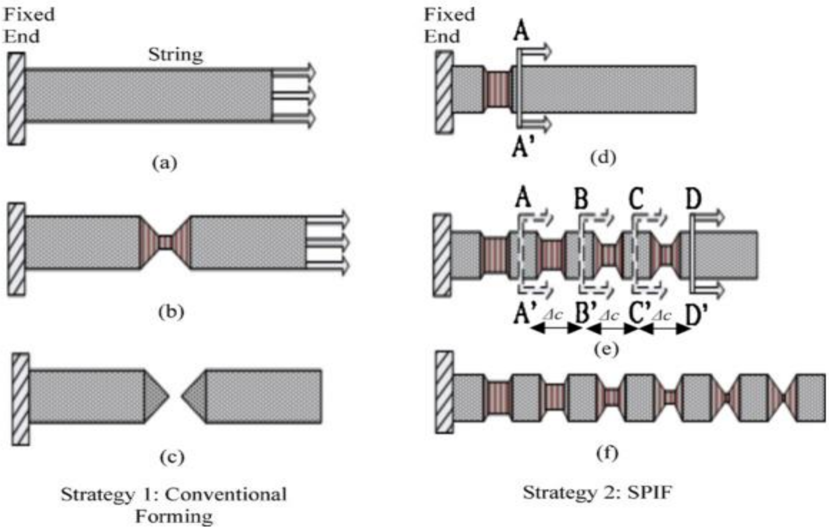

Figure 2.32: Schematic of noodle theory.[59]

2.4 Process Parameters in SPIF

The prominent factors that affect formability in case of SPIF are the forming tool diameter, the tool geometry, the step down, the feed rate, the spindle speed, and the material thickness. The effect of these process parameters are discussed in this section. The overall review of the effect of the process parameters of the formability of SPIF is presented in Table 2.4. The process parameters like lubrication and the tool path affect surface integrity of formed component. These parameters will be discussed in detail in the section 2.5.

From Table 2.4 we can conclude that in general when the thickness of the blank sheet is higher the formability is also higher. Hussain et al. [60] examined the influence of the tool radius (r_{tool}) to sheet thickness (t) ratio on failure, which can be said to preclude formability. The AA 1060 material is tested at two thicknesses, 0.7 and 2.6 mm, which is quite a large range – the largest difference between two successive thicknesses. They concluded that an optimisation of the r_{tool}/t ratio is needed to increase the formability, where r_{tool} is the forming tool radius and *t* is the sheet thickness.

The effect of the feed-rate is not comprehensively studied [61] and in some materials the increase in feed-rate causes decrease in formability while in some there is no effect (see Table 2.4).

Table 2.4: Effect of increase in following Process Parameters on formability in SPIF (adapted from [61]*)*

Paper	Material	Sheet thickness	Tool Diameter	Step-down	Feed rate	Spindle speed
Jeswiet, 2002 [62]	AA3003-O	↑	-	-	-	-
Kim, 2002 [7]	AA1050	-	-	↓	-	-
Strano, 2005 [63]	AA1050	-	↓	↓	-	-
Ham, 2006 [64]	AA3003-O	↑	↓	↓	↓	↑
Hussain, 2008 [65]	Pure-Ti	-	↓	↓	↓	-
Petek, 2009 [42]	DC05	-	↓	↓	-	-
Durante, 2011 [66]	AA7075-O	-	↓	↓	-	-
Silva, 2011 [21]	AA1050-H111	-	↓	-	-	-
Xu 2013 [67]	AA5052-H32	-	-	-	-	↑
Buffa 2013 [68]	AA1050-O, AA1050-H24, and AA6082-T6	-	-	-	-	↑
Shanmugantan, 2013 [69]	AA3003-O	↑	↓	↓	-	-
Golabi, 2014 [70]	SS304	↑	↓	↓	No effect	-
Centeno, 2014 [71]	SS304	-	↓	↓	-	-

↓ indicate decrease in formability and ↑ indicate increase in formability.

In general for the single point incremental forming of sheet metals when the forming tool diameter is increased the formability decreases. However Li et al. [72], showed that in case of AA7075-O the formability increases with increase in tool diameter. This study uses straight groove test to measure the formability whereas other studies use varying-angled truncated conical geometry to measure the formability. However, regarding the straight groove test, for which Durante et al. [66] have noted that, this type of test is not indicative of the actual deformation in SPIF.

The increase of the diameter of the tool leads to a distribution of stresses in a larger area of the workpiece, because the contact surface between the tool and the workpiece to be deformed is also larger. Silva et al. [21] found that the increase in tool diameter results in a decrease in the formability of the material based on the incremental forming tests with truncated conic and pyramidal geometries. The authors concluded that the increase of the diameter of the tool leads to a decrease in the forming angle and an increase in the stress triaxiality ratio (TR) (equation 2.20).

$$TR = \frac{\sigma_m}{\bar{\sigma}} \tag{2.20}$$

Where σ_m is hydrostatic stress and $\bar{\sigma}$ is effective stress.

In addition, the authors presented the influence of the tool diameter ratio on the thickness of the workpiece (t/r_{tool}), proposing a critical limit for this relationship that separates the fracture with the occurrence of necking and with the absence of this phenomenon (see Figure 2.33)

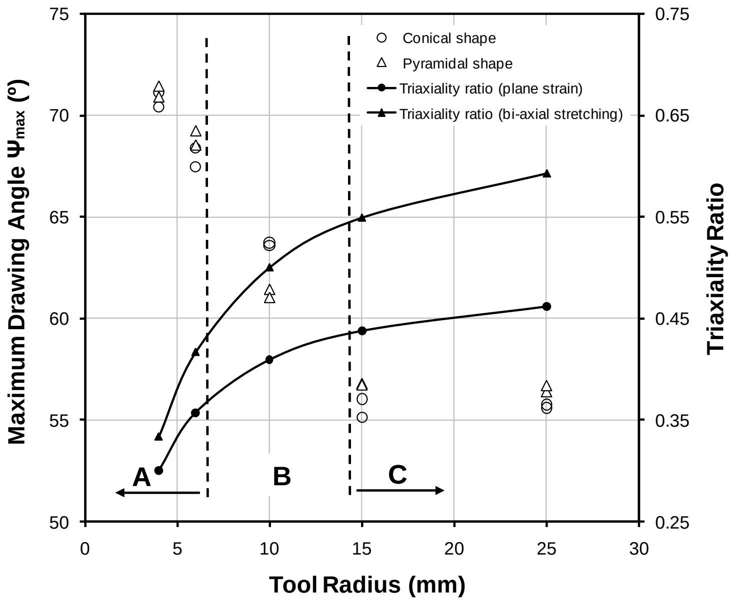

Figure 2.33: Graphical representation of effect of tool diameter in SPIF [21]

The geometry of forming tool also significantly affects the formability in SPIF. Roller/spherical forming tool and oblique rolling tool [52] leads to increased formability than compared to flat-end and hemispherical forming tool [73] of the same diameter.

The step down is the amount of forming depth taken by the forming tool after completion of one revolution. This is the second most prominent process parameter after the tool diameter, which affects formability. The majority of studies suggest that decreasing the step down increases formability whereas few [74] suggest that an increase in the step-down increases formability.

Spindle speed has significance in SPIF as this affects the friction coefficient between forming tool and the sheet metal. In general increasing the spindle speed increases the formability [61]. At a high value of the spindle speed, the heating, due to friction, causes the material to soften and advantageous microstructural changes may occur improving the formability [67], [68]. Non-rotating forming tool are detrimental to both formability and surface quality [66], [75]. And free to rotate or roller forming tool results to a minimum friction, reducing the surface roughness and the friction forces [68].

2.5 Lubrication in SPIF

In the conventional machining and the sheet metal forming processes, in general, lubrication assists to increase the quality of the final product. Similarly it is observed that there is a positive effect of the use of lubrication in SPIF to reduce the surface roughness [67], [76].

2.5.1 Effect on Surface roughness

Along with lubrication, the process parameters that affect the surface roughness in SPIF are: spindle speed, feed, step down, forming tool type, forming tool diameter, tool path or tool trajectory [77]. Increasing the tool feed and the step size increases the surface roughness of the component in SPIF. Increasing the spindle speed and the tool diameter leads to a decrease in the surface roughness.

Hussain et al. [78] studied the applicability of various lubricants (solid state and liquid state) in incremental forming of pure titanium (Ti). In this study it was observed that the paste of MoS_2 powder and white petroleum jelly gives an acceptable surface roughness in SPIF of pure Ti. Zhang et al. [76] analysed the effect of lubrication in the magnesium alloy hot forming, finding that a solid graphite or ceramic powder (MoS_2) delivers outstanding results, as well as a self-lubricating effect. For soft metals such as aluminium and low carbon steel, mineral oils will suffice to produce components with an acceptable surface quality [7].

One of the unique technique to obtain good surface roughness in SPIF is to use dummy sheet between the sheet to be formed and the forming tool [79].

2.5.2 Effect on formability

Lubrication has been primarily used in SPIF to reduce the tool wear [76], [78] and recently used in order improve the surface integrity [80]. It is interesting to note that even though all studies mentioned above have shown that the surface roughness improves when lubrication is used, study done by Kim and Park [7] shows negative effect of lubrication on the formability. This study however uses straight groove test to measure formability, which Durante et al. [66] have noted that this type of test is not indicative of the actual deformation in the SPIF. The effect of lubrication on the formability thus remains unexplored and it is important that the effect of lubrication on the formability of the material should be studied.

2.5.3 Surface Morphology and Microstructure study

Kim and Park [7] in their study of SPIF on A1050 sheet metal, observed under optical microscopy that no lubrication state led to scratches on the forming tool and led to more tool wear (see Figure 2.34). The study also stated that a spherical end tool improves formability limits in SPIF, rather than hemispherical tool. Hussain et al. [78] presented in their study, various combination of tool's material and lubrication to determine their suitability in SPIF of the commercially pure titanium sheet. They used scanning electron microscopy (SEM) to study the interaction between the tool and the sheet, and they concluded that the sheet surface coating was essential in order to achieve a better surface integrity (see Figure 2.35) with a HSS tool material and a lubricant which is a combination of molybdenum disulphide and petroleum jelly in a specific quantity.

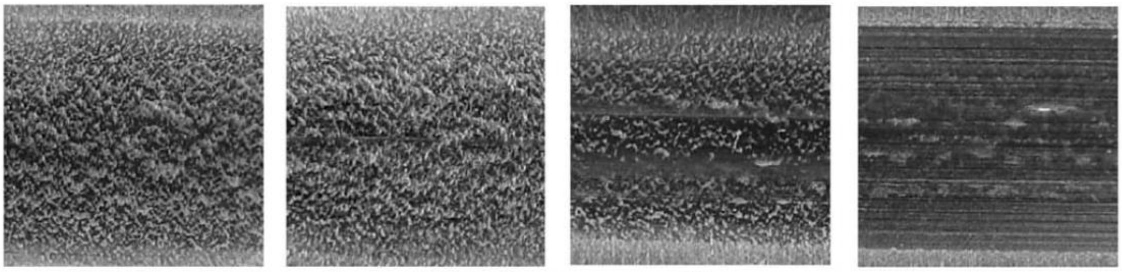

(a) (b) (c) (d)

Figure 2.34: Optical images of surfaces formed: (a) Spherical end tool with lubrication, (b) Spherical end tool without lubrication, (c) Hemispherical end tool with lubrication,(d) Hemispherical end tool with lubrication.[7]

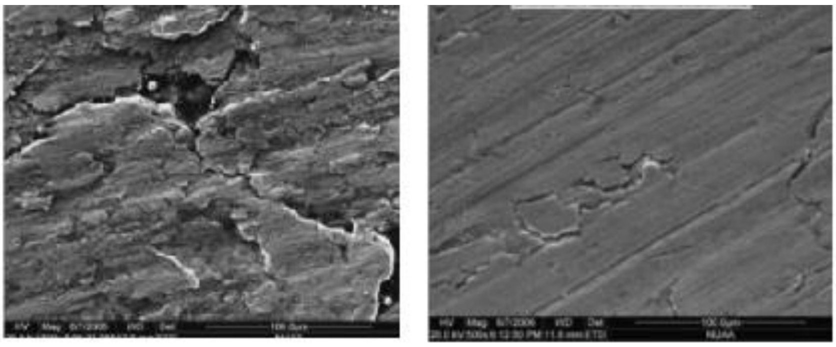

(a) (b)

Figure 2.35: SEM image of formed surface: a) Without surface coating, b) With surface coating [78]

Zhang et al. [76] investigated a suitable lubricant and lubricating methods for warm SPIF of magnesium alloy AZ31 sheet. As lubrication a $K_2Ti_4O_9$ whisker along with the solid graphite or MoS_2 powder-coated porous ceramic coating by pulsed anodic oxidation was used. SEM was used to study the formed sheet surface and it was observed that above mentioned lubrication coating technique gave a good lubrication performance.

Apart from studying lubrication/tribological aspects, SEM is also used to understand various phenomenon. Shanmuganatan et al. [69] used SEM to study the grain of a single point incrementally formed Al3003(O) sheet and observed an increase in strength of the sheet is due to the fragmentation of the grains.

Hamilton and Jeswiet [81] studied the microstructure of a single point incrementally formed Al 3003-H14 sheet using SEM and SEM revealed that there is change in the grain size observed in the formed component and this is greatly influenced by the step size. The reason for this change remains undiscussed. Ben Hmida et al. [82] studied the effect of the initial grain size in single point incremental forming of copper. In this study it was concluded that when the ratio between the sheet thickness and the initial grain size decreased the mechanical properties of the copper decreased and also the formability.

2.6 Finite element analysis for SPIF

Finite element analysis can be helpful to analyse the forming forces and predict springback [50]. The most important task in Finite element analysis (FEM) for SPIF is to select an appropriate element type and the allocation of mesh. A very fine mesh is necessary to be used in the case of numerical simulation of SPIF as the tool-blank interface is very small and this will led to an increase in the computation time. Numerical simulation in case of SPIF is thus very time consuming and complex. Ambrogio et al. [83] used explicit model in place of implicit model and reduced the computational time. The use of explicit model also eliminated the convergence problem caused when implicit models are used. The major drawback however, in using an explicit model is the accuracy of formed geometry is not good. In SPIF the final component geometry is drastically different than the initial blank, and the component undergoes high deformation. This means that the meshing strategy considered for initial stage is not useful for the last stage, instead it causes distortion of the elements. For this reason adaptive remeshing is used in SPIF [50].

The comparative properties of element types majorly used in numerical simulation of SPIF are listed in Table 2.5.

Table 2.5: Aspects of Elements (adapted from [50]*)*

Element type	**Thickness prediction**	**Force prediction**	**Through the thickness shear**	**Flow of material**	**Computational time**
Shell	good	good	bad	bad	less
Solid	good	good	good	good	very high
Solid-shell	average	average	average	average	average

2.7 Applications

The applications of SPIF range widely from medical to aerospace components. This process is particularly appropriate when the component is to be produced in small batch and prototypes because SPIF causes significant saving on the material and the energy when compared with the conventional forming process. In this section the various applications of the SPIF are presented.

Honda used incremental forming to manufacture a limited series of replacements component (see Figure 2.36) for a sport car in collaboration with Amino in 2002 [29]. The replacement component was car hood and were produced with SPIF as a small batch was to be manufactured. Amino produced a panel with pyramid shapes on single A1050 sheet metal (see Figure 2.37a) to check the feasibility of this process on the selected car-body material. Amino has also provided a custom solution to the TOYOTA iQ-GRMN car model by producing formed car model logo on car body (see Figure 2.37b) and sharpening the features using SPIF of mounting boss on side panel of car (see Figure 2.37c) [84].

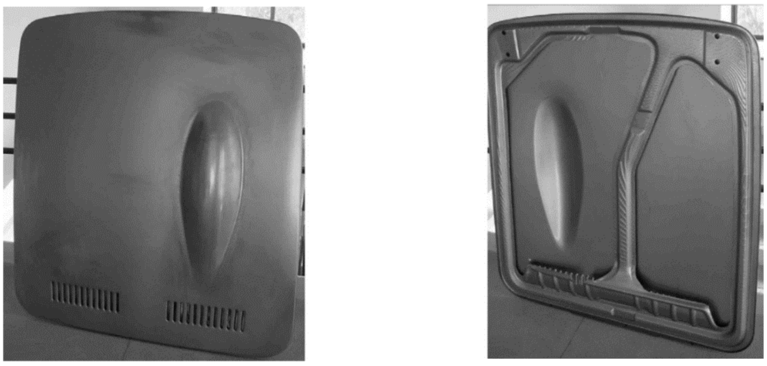

(a) (b)

Figure 2.36: a) top view of component; b) bottom view of component; produced by Amino for Honda [29]

(a) (b) (c)

Figure 2.37: Application developed by Amino: a) Variety of pyramid shapes, b) Logo mark on Door panel of TOYOTA iQ-GRMN, c) Mounting boss on side panel of TOYOTA iQ-GRMN [84]

Some applications are also in the field of aerospace, like producing aerodynamic cones and pressure sensor casing for an airflow management system [50] (see Figure 2.38).

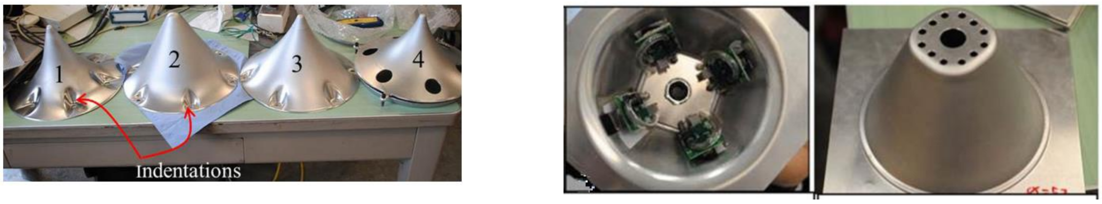

(a) (b)

Figure 2.38: a) aerodynamic cones; b) sensor casing for airflow management system [50]

The aerodynamic cones and pressure sensor casing were to be produced in different dimensions to check for their reliability. Manufacturing them with conventional stamping process would have required to produce die and punch for each dimension. Using SPIF time, energy and resources were saved.

The dimensional needs of medical replacement part are very specific to the patient and only one part is required. The use of incremental forming to produce these parts is therefore most appropriate. Thus incremental forming is proven to be very useful in the medical field. Medical parts produced by SPIF are: an ankle support [85], a cranial plate [86], a dental crown [87], facial implants [88], and a denture plate [89] (see Figure 2.39).

(a) (b) (c)

Figure 2.39: a) Cranial plate [86]*; b) facial implant* [88]*; c) denture plate* [89]

Some other useful applications produced using SPIF are: custom manufacture of a solar oven, a vehicle headlight, an automobile heat/noise shield, a motorbike gas tank, the automobile body panels, a silencer housing, an architectural bespoke formwork, the decorative panels, the reflectors, the casings for lightings, a housing for aerospace, a bathroom sink [39], the ship hull plates [6], [87]. Figure 2.40 shows some of the above mentioned applications of SPIF.

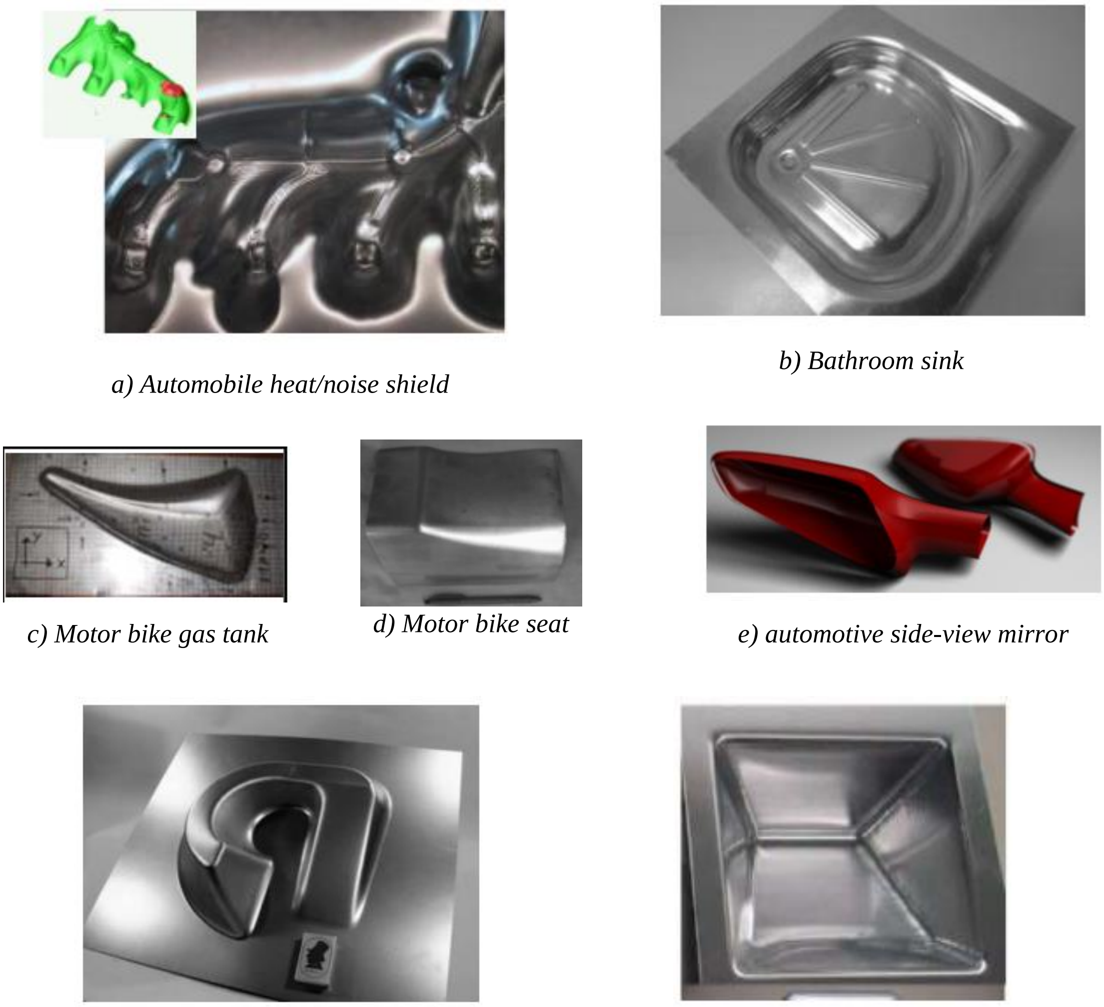

a) Automobile heat/noise shield

b) Bathroom sink

c) Motor bike gas tank

d) Motor bike seat

e) automotive side-view mirror

f) Automobile Silencer housing

g) Solar oven component

Figure 2.40: Incremental forming applications (adapted from [6] *and* [39]*)*

From above examples we can conclude that the SPIF is a very versatile process and is economical to use when small batch is to be manufactured. This process also facilitates the rapid prototyping of sheet metal as the manufacturing time involves only SPIF process and no lead time is required for tooling.

Chapter 3 **Experimental setup**

This chapter begins with the description of the material and method used for material characterization, the different tests used to characterize the necking and fracture limits and the methodology to find fracture properties i.e. specific essential work of fracture (fracture toughness). Later the SPIF setup, its process parameters and lubrication conditions along with the plan of experiments for SPIF are presented. The last section explains the equipment used to measure and study different parameters like initial dimensions, after fracture dimensions, the grids, the surface roughness, part geometry and the microstructure.

3.1 Material

The material used for this study is an oxygen-free 99.9% copper sheet, cold rolled with 0.8 mm thickness. Copper is one of the important non-ferrous materials due to its good mechanical properties and is thus suitable for general applications. Copper has high ductility and malleability, is a good conductor of heat and electricity along with good corrosion resistance. Due to these properties Copper is used to produce electric wires, architectural and civil applications, jewellery, household utensils, heat exchangers and house decorations. As it is biofouling resistance it finds its application in ship building, offshore oil and gas stations.

Copper has high density and has face centred cubic lattice structure. Copper sheet used in this study has a multicrystalline structure. The use of multicrystalline materials to study plastic deformation mechanisms gives a better understanding of the plastic deformation behaviour [90]. The chemical composition of the copper sheet used for this study is presented in Table 3.1.

Table 3.1: Chemical composition of the Copper sheet

Element	Cu	Bi	O	Pb
% composition	99.9	0.0005	0.04	0.005

3.2 Material characterization and Formability determination

This section describes the tests used to determine the mechanical characterisation and formability characterisation. The tensile test and the bulge test are used to determine the stress-strain curve. The tensile test, the shear test, the staggered test, the double notch tensile test, the nakajima test and the bulge test are used to determine both formability limits by necking and formability limits by fracture. The experimental plan for these tests are described in this section.

3.2.1 Tensile test

The tensile test is one of the most common ways to obtain the material properties. This test allows finding the stress-strain curve as well as points in the second quadrant of the Forming Limit Diagram (FLD). The tensile test allows the determination of mechanical properties of the sheet metal, such as tensile strength, hardening coefficient, % elongation, yield stress, anisotropy coefficient, elastic yield stress, modulus of elasticity and the hardening law of the material.

The tests were carried out on the universal test machine INSTRON model 4507 according to ASTM E8 / E8M - 09 standard (2013) [13], using HRDE (High Resolution Digital Extensometer) strain gauges, which measure longitudinal and transverse deformations. The force and displacements values were obtained by means of a load cell and a displacement transducer respectively and a PC (see Figure 3.1a) equipped with a data acquisition system which records and displays the load and the displacement values resulting from the test.

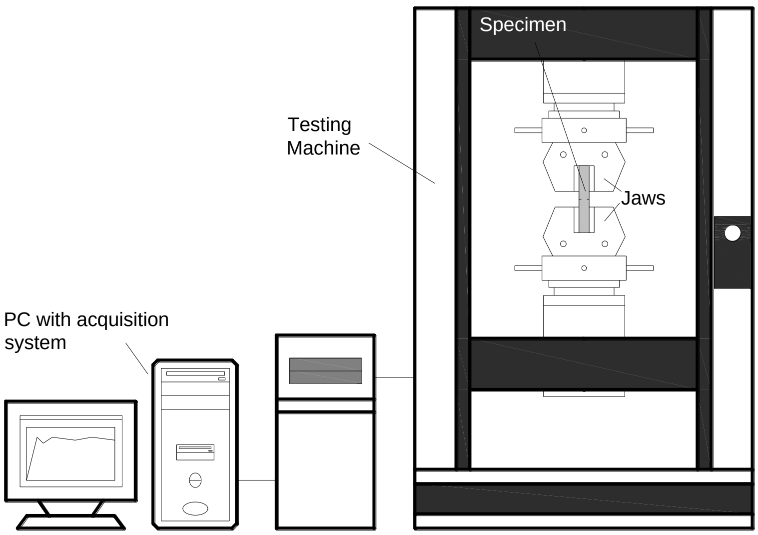

a)

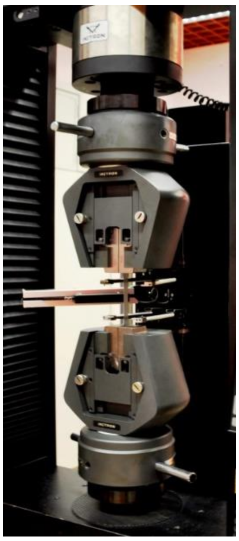

b)

Figure 3.1: a) Schematic representation of the experimental apparatus and b) photograph showing a tensile specimen mounted between the jaws of an INSTRON model 4507 machine.

The geometry of the test specimens (produced according to the ASTM E8 / E8M - 09 (2013) standard [13]) used to perform the tests is given in Table 3.2, as well as the quantity of test specimens tested. The copper test specimens used in tensile test were obtained from sheet cut at 0°, 45° and 90° relative to the rolling direction and have a thickness of 0.8 mm. They were cut by wire electric discharge machining (wire-EDM).

Table 3.2: Reference dimensions of test pieces used for tensile test and respective test plan

Angle with Rolling direction	Quantity of specimens	Dimensions (mm)	Specimen geometry
0º	5	$b_0 = 13$ $l_c = 57$ $l_0 = 50$ $w = 19$ $r = 76$	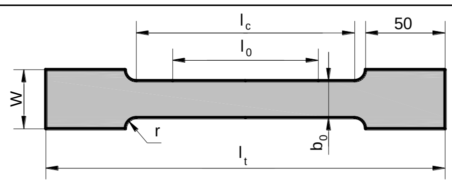
45º	5		
90º	5		

The specimens were electrochemically etched with a grid size of 2 mm interlaced circles. The details for the electrochemical etching of grids are presented in section 3.4.

3.2.2 Double notch tensile test

The double notch tensile test (DNTT) specimens with varying ligament lengths (a) (see Table 3.3) are used to determine the fracture toughness [14]. This specimen causes fracture by mode I of fracture mechanics in the ligament. The fracture strain obtained from this specimen lies in the plane-strain deformation region on Fracture Forming limit Line (FFL) in the principal strain space (FLD). The test specimens used with the varying the ligament lengths (a) are presented in Table 3.3.

Table 3.3: Reference dimensions of test pieces used for tensile test and respective test plan

Angle with rolling direction	Quantity of Specimens	Dimensions (mm)	Specimen geometry
0º	10	$l_0 = 150$ $w = 50$ $t = 3$ $a = 5, 10, 15,$ 20 and 25	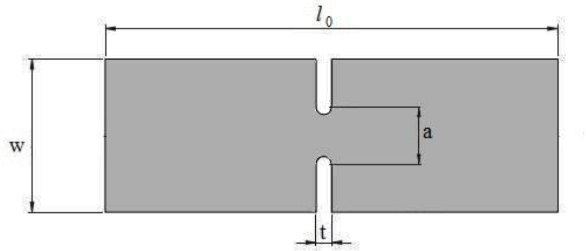
90º	10		

The copper test specimens used in the DNTT tests were obtained from sheet cut at 0° and 90° relative to the rolling direction and have a thickness of 0.8 mm and they were cut by wire-EDM. Using the force vs displacement curve for different ligament size, the value for fracture toughness (*R*) fracture by mode I was calculated. The methodology of fracture toughness calculation is presented in section 2.1.3.

3.2.3 Shear test

Shear test specimen can be used to determine the fracture properties when the specimen fractures by mode II of fracture mechanics. Isik et al. [5] introduced the V-slit shear specimen and Shouler and Allwood [16] introduced the C-slit shear specimen for these fracture properties determination. Both these specimen induces fracture by mode II when uni-axially loaded on an universal testing machine. These specimen gives fracture points on the SFFL in the FLD. The geometry of the test specimens and the plan of experiment is presented in Table 3.4.

Table 3.4: Reference dimensions of test specimens used for shear test and respective test plan

Angle with Rolling direction	**Quantity of specimen**	**Dimensions (mm)**	**Specimen name and geometry**
0º	12	$l_0 = 235$ $w = 25$ $t = 1$ $a = 1, 2, 3, 4, 6, 8$	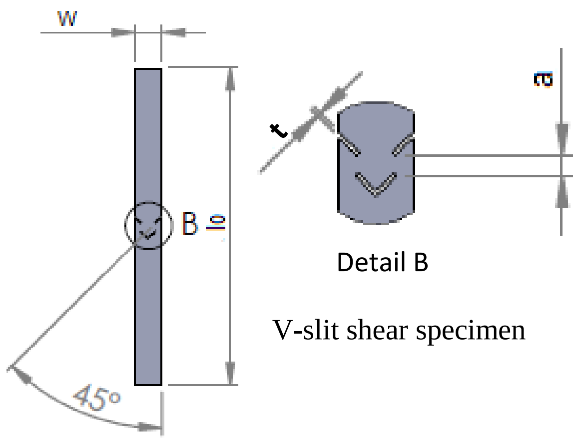 V-slit shear specimen
90º	12		
0º	10	$l_0 = 235$ $w = 40$ $t = 1$ $a = 2, 3, 5, 6, 8$	

0°	10	$l_0 = 160$ $\mathrm{w} = 52$ $\mathrm{t} = 2$ $\mathrm{a} = 2, 3,$ $4, 6, 8$	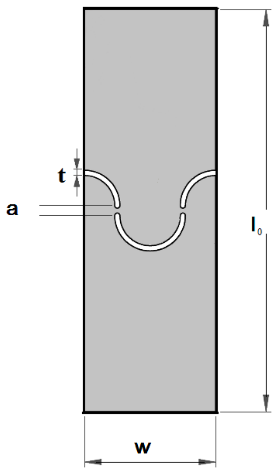	C-slit shear specimen

The copper test specimen used in shear test were obtained from sheet cut (using wire-EDM) at 0° and 90° relative to the rolling direction and have a thickness of 0.8 mm. The specimens then were uni-axially loaded on the universal testing machine, INSTRON model 4507. Using the force vs displacement curve for different ligament lengths, the value for fracture toughness (*R*) for fracture by mode II was calculated. The methodology used to find *R* is presented in section 2.1.3.

3.2.4 Staggered test

Double notch tensile specimens provide fracture points on the FFL and the shear specimens provide fracture points on the SFFL. In order to investigate the transition region between FFL and SFFL, staggered test specimens are evaluated in this study. Cotterell et al. [15] used the staggered double notch tensile test (s-DNTT) specimens with varying ligament lengths to determine the fracture toughness in mixed mode I&II of fracture mechanics. This specimen causes fracture by mixed mode I&II in ligament area when subjected to uni-axial loading in universal testing machining. Along with s-DNTT specimen a variation of C-slit shear specimen, i.e. staggered C-slit shear specimen (s-CS) was used in this study to induce fracture by mixed mode I&II of fracture mechanics. The s-CS specimen is presented in Table 3.5 along with its dimensions. In s-CS specimen the slits are not in-line but are deviated, unlike C-slit shear specimen (see Table 3.4).

The test specimens used with varying ligament lengths (a) and plan of experiments are presented in Table 3.5.

Table 3.5: Reference dimensions of test pieces used for staggered test and respective test plan

Angle with Rolling direction	Quantity of Specimen	Dimensions (mm)	Specimen name and geometry
0º 90º	10 10	$l_0 = 150$ $w = 50$ $t = 3$ $a = 5, 10, 15, 20, 25$ $d = 5, 10, 15, 20, 25$ for all cases, $a = d$	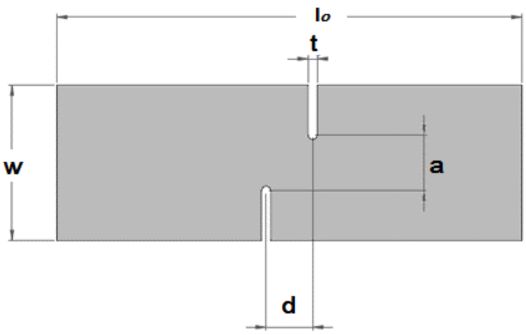 s-DNTT Specimen
0º	10	$l_0 = 160$ $w = 52$ $t = 2$ $a = 2, d = 1$ $a = 2, d = 2.5$ $a = 3, d = 1$ $a = 5, d = 2.5$ $a = 8, d = 2.5$	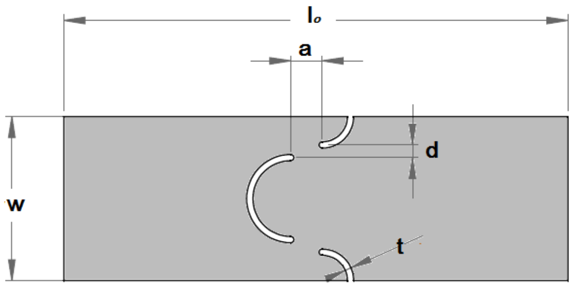 s-CS Specimen

The copper test specimen used to fracture by mixed mode I&II test were obtained from sheet cut (using wire-EDM) at 0° and 90° relative to the rolling direction and have a thickness of 0.8 mm. The specimens then were uni-axially loaded on the universal testing machine, INSTRON model 4507. Using the force vs displacement curve for different ligament size, the value for fracture toughness ($R_{I\&II}$) for fracture by mixed mode I&II was calculated. The results are presented in section 4.2. The methodology used to obtain R is explained in section 2.1.3.

3.2.5 Bulge test

The hydraulic biaxial bulge tests were performed on an universal sheet testing machine, designated by Erichsen Model 145/960, available at Instituto Superior Técnico (IST) - Lisbon, (see Figure 3.2a) and an in-house designed Bulge machine, available at Instituto de Engenharia Mecanica e Gestão Industrial (INEGI), Porto, (see Figure 3.2b). HBM position transducer (Hottinger Baldwin Messtechnik) and a MGC data acquisition system is used in the IST based bulge machine. A LVDT transducer and LabView interfaced acquisition system is used in the INEGI based bulge machine.

(a)

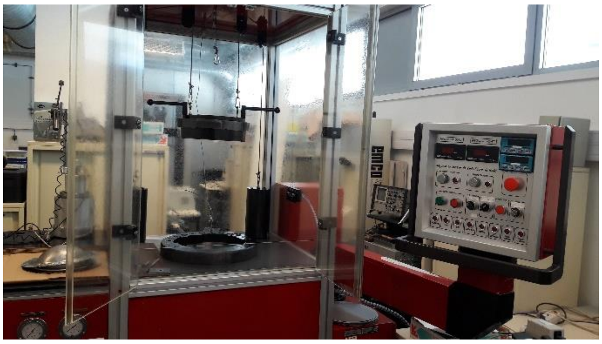

(b)

Figure 3.2: Bulge test machine available at: a) IDMEC, IST-Lisbon and b) INEGI, Porto

During the tests, values were acquired for the force and the displacement. Throughout the test the height of the polar zone was continuously recorded through a position transducer and the pressure value through a pressure transducer which is then converted into force. The pressure and the position acquisition are achieved through a PC equipped with a data acquisition board and software. The objective of the bulge test is to achieve the fracture strains and the necking strains in the first quadrant of the FLD. The bulge test induces biaxial strains whereas the tensile test induces uniaxial strain, thus bulge test can also be used to acquire biaxial stress-strain curve to determine the material hardening law.

This test was performed using circular sheet specimens. Specimen and die geometries as well as the experimental plan for each of the geometries are presented in Table 3.6. For the bulge test done on machine available at INEGI, Porto the specimen sheet diameter of 250 mm was used and for the bulge test done on machine available at IST, Lisbon the specimen sheet diameter of 175 mm was used.

Table 3.6: Reference geometry for bulge test specimen and respective test plan

Die geometry	**Quantity of specimen**	**Example of geometry to be formed**	**Specimen sheet geometry**
Die geometry: Circular D=180 mm	3		

Die geometry: Elliptical Major to minor diameter ratio =100:80	3		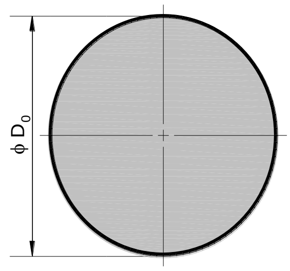 D_o = 250 mm
Die geometry: Elliptical Major to minor diameter ratio =100:60	3		
Die geometry: Circular D=120 mm	2		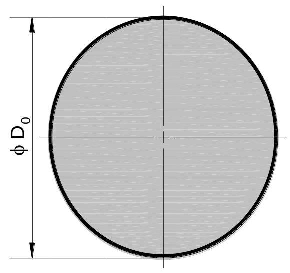 D_o = 175 mm

The copper bulge sheet test specimens were electrochemically etched. The procedure and the grid used for this test are presented in section 3.4. The initial thickness of the specimen is 0.8 mm. Specimen sheet was clamped tightly in the hydraulic bulge machine and then subjected to biaxial tension using very high oil pressure until the sheet cracks.

3.2.6 Nakajima test

The Nakajima tests were performed on the universal sheet testing machine, Erichsen Model 145/960 (see section 3.2.5). The geometries and dimensions of the test specimens used for the tests are presented in Table 3.7.

The copper Nakajima test specimens were electrochemically etched (see section 3.4). The initial thickness of the specimen is 0.8 mm.

Table 3.7: Reference geometry for Nakajima specimen and experimental plan

Quantity of specimen	Dimensions (mm)	Specimen geometry
12 (2 specimens for each radius, R)	$D_0 = 210$ $R = 40, 50, 57.5,$ $65, 72.5, 80$	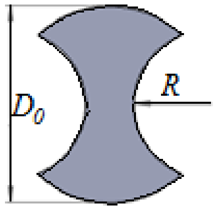

3.3 Single Point Incremental Forming setup

In this section the experimental setup including the machine tool, the forming tool and the clamping rigs for SPIF is described in detail.

3.3.1 Machine tool

The single point incremental forming was performed on a Flexi-optima 5 axis machining centre with a Fagor 8065 controller. The sheet is incrementally formed by a forming tool controlled by CNC code. The sheet was rigidly clamped on a rig using a blank holder (see Figure 3.3). The rig also supports a backing plate below the sheet formed by the forming tool.

To obtain the helical tool trajectory, a CAD / CAM program was used with a postprocessor, allowing the conversion of the program information from the PC to the machine tool controller (see section 3.3.5).

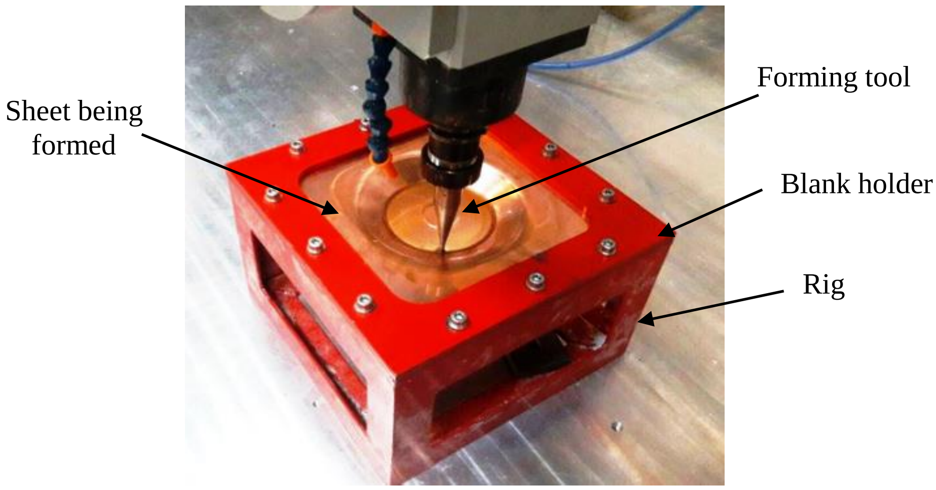

Figure 3.3: Sheet formed by forming tool and rigidly clamped on rig

3.3.2 Forming tool

Three different forming tool materials with different diameters were used to determine the effect of tool material on the tool wear in SPIF. Table 3.8 lists these tool materials along with their hardness.

Table 3.8: Tool material and their hardness

Number	Material	Hardness
1	40CrMnNiMo 8-4-6 steel (PM300)	310 HB
2	CK40 steel	421 HB
3	Tungsten-carbide	2550 HV

The forming tools used in this study are presented in Table 3.9. These tools are used to study the effect of different tool diameter, geometry, tool material on the formability limits for single point incremental forming of copper sheet.

Table 3.9: List of forming tool used in this study

<table>
<tr><th>Tool geometry</th><th>Tool diameter (mm)</th><th>Tool material</th><th>Image of forming tool</th></tr>
<tr><td rowspan="2">Spherical end tool</td><td>10 and 12</td><td>Tungsten-carbide</td><td>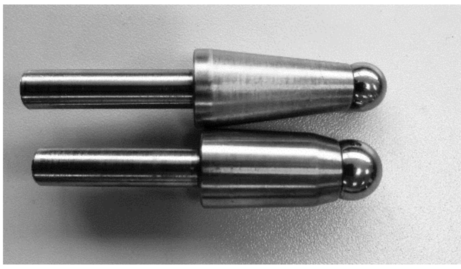</td></tr>
<tr><td>10</td><td>PM 300</td><td>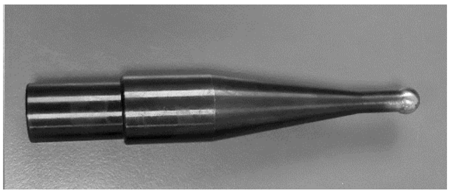</td></tr>
</table>

Hemispherical end tool	6, 8, 10 and 12	PM 300	
	6 and 8	CK 40	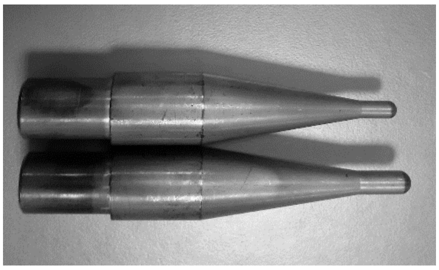

3.3.3 SPIF clamping system

In this section the rigs used to clamp the copper sheet metal for single point incremental forming are described. The geometries formed, using the rig (presented in Figure 3.4) used to clamp, are the truncated pyramid, cone and 4 lobe shaped cone.

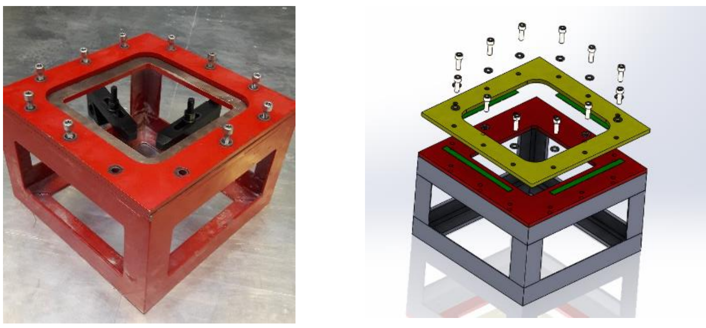

(a) (b)

Figure 3.4: a) Rig with square backing plate, b) Exploded view of square backing plate rig

The rig has max forming area of 220 mm X 220 mm for square backing plate rig and maximum forming area of 220 mm diameter for circular backing plate. For forming application larger than above mentioned area another rig, shown in Figure 3.5, is used.

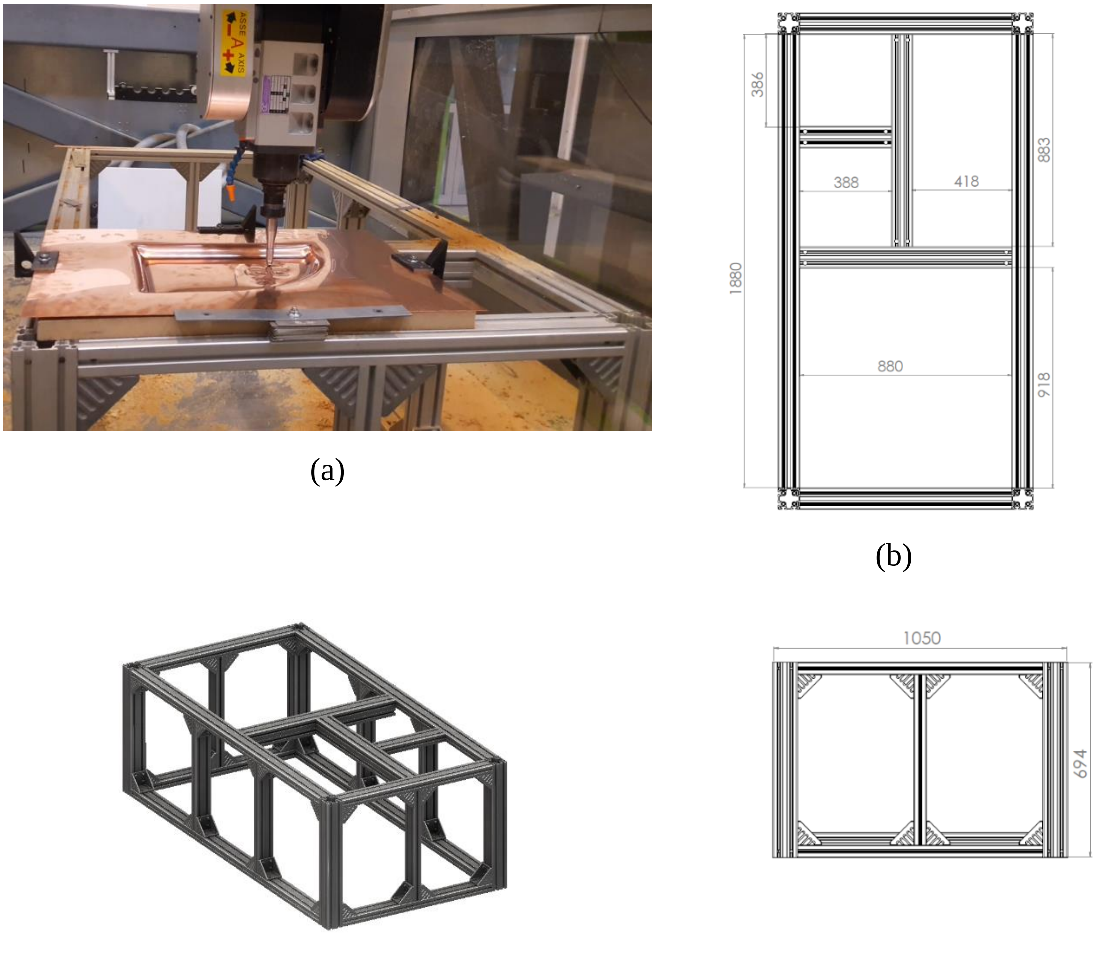

(a) (b) (c) (d)

Figure 3.5: a) Rig used to single incrementally form application for SPIF, b) Top view of the jig, c) Isometric view of jig, d) Side view of the jig

3.3.4 Lubrication

In conventional machining and sheet metal forming processes, in general, lubrication assists to increase the surface quality of the final product. Similarly it is observed that there is a positive effect of the use of lubrication in Single point incremental forming. The surface roughness decreases. In this study, different lubrication conditions (presented in Table 3.10) were used in order to study the effect of the lubrication on the surface roughness and consequently on the formability of the material.

Table 3.10: Lubrications used for the study

Lubrication condition	Lubricant reference	Chemical composition	Base	State	Viscosity (mm/s²) at 40°C
1	Copaslip from Molyslip	15% hydrated Mg silicate + 15% Copper flakes + 15% hydrocarbon polymer + oil	Mineral oil	Paste	96.2

2	AS 40 from Molyslip	40% MoS_2 + 15% graphite powder + 25% EP lithium grease + oil	Petroleum oil	Thick liquid	na
3	Weicon Ni Special	20% Ni powder + 10% Calciumhydroxide + oil	Mineral oil	Paste	na
4	Weicon montage	20% ceramic powder + 10% Aluminiumpulver + oil	Mineral oil	Paste	185
5	Castrol Magnaglide D68	Refined mineral oil	na	Oil	68
6	no Lubrication	na	na	na	na

The paste-state lubrication was spread over the sheet before the forming process whereas the oil state lubrication is sprayed over the sheet before the forming process.

3.3.5 Formed geometry and tool-path

Different geometry induces different deformation states and the wide range of possible deformation in the principal strain space can be covered. Three geometries for SPIF where used to determine the formability limits of copper using SPIF. The three geometries are presented in Table 3.11.

Table 3.11: Different geometries formed using single point incremental forming

Part geometry	Quantity	Deformation mode	Initial sheet dimension
Conical geometry: 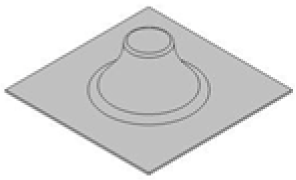	5	Plane strain deformations along the wall of the cone	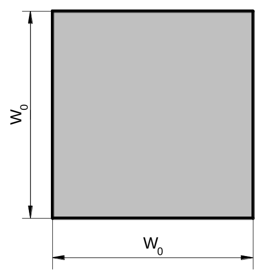 $w_0 = 250\ mm$
Pyramid geometry: 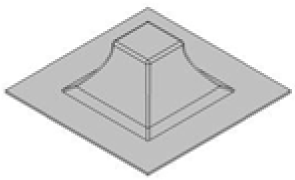	5	Equi-biaxial deformation on the corners and plane strain deformation along the walls	
4-lobe geometry: 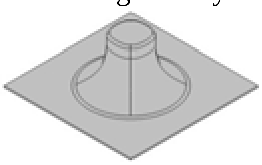	5	Pure shear in the corners and plane strain deformation along the walls	

The forming parameters (presented in Table 3.12) were kept constant throughout the experiments to determine the formability limit. The results are presented in section 4.5.

Table 3.12: Process parameters used to determine formability of copper using SPIF

Spindle speed	**Feed rate**	**Step down**	**Tool path**
Free rotation	1000 mm/min	0.15 mm	Helical

To develop CAD model of the geometries the SOLIDWORKS® software was used. The details of the drawings are presented in Table 3.13. The initial blank sheet dimensions (250 mm X 250 mm) were the same for all the geometries. All the geometries start with inclination of 30º along the depth direction for 10 mm and then the angle gradually increases as the curvature increases. The curvature is defined by a radius of 63.5 mm for all the geometries.

Table 3.13: Detail drawing of single point incrementally formed geometries

<table>
<tr><th></th><th>Conical geometry</th><th>Pyramid geometry</th><th>4-lobe geometry</th></tr>
<tr><td>Top view</td><td>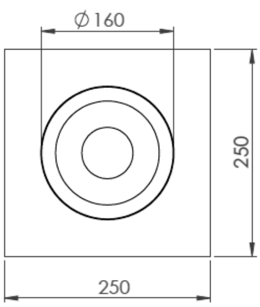
</td><td>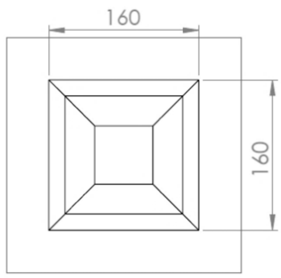
</td><td>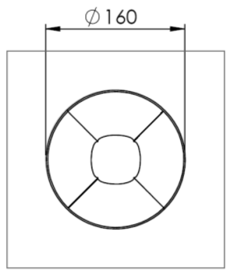
</td></tr>
<tr><td>Side view</td><td>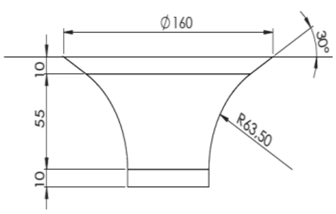
</td><td>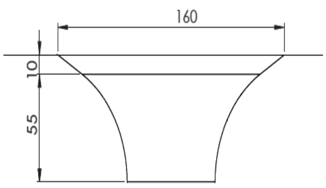
</td><td>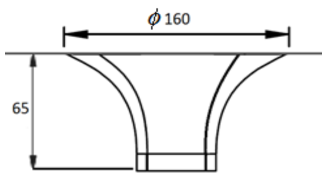
</td></tr>
</table>

The tool path for SPIF was generated using the MasterCAM® (version: X7) CAM software. The MasterCAM software does not have an incremental forming feature to develop the tool path so the *finishing- counter* feature of the software was used with ball end mill tool (see Figure 3.6). The spindle speed throughout this study was kept at 0 rpm but the spindle was set free to rotate under friction.

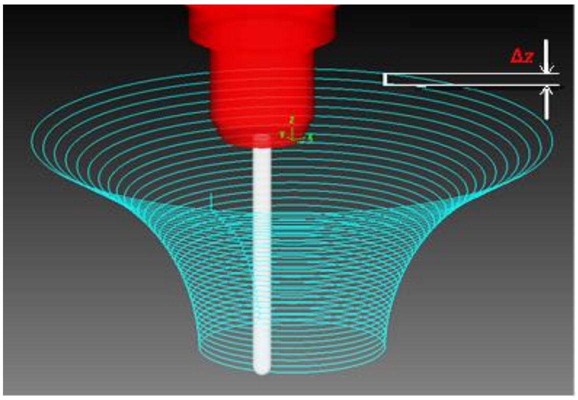

Figure 3.6: Generated tool path for conical geometry.

The step down, Δz is the incremental forming depth taken by the forming tool for each step and is represented in Figure 3.6.

3.4 Circular grid etching

The circular grids are marked on the sheet specimen to determine the principal strains. In order to have a clear marking on the sheet, electrochemical etching was used for grid marking. Electrochemical etching is advantageous because this process does not affect the mechanical properties of the marked sheet. The electrochemical etching methodology used for the copper sheet is as follows,

1) The copper sheet is properly cleaned by alcohol to remove any oxide layer or dust.
2) The sheet is connected to the positive anode of the electrochemical machine as seen in Figure 3.7. The grid stencil is placed over the sheet.
3) The cotton cloth is moistened with the electrolyte and is placed over the grid stencil.
4) The electric roller connected to negative cathode of the electrochemical machine is rolled over the sheet area to be etched.
5) After the sheet is electrochemically etched with grid the sheet is rinsed with a neutralizer to stop further chemical reaction. The selection of electrolyte and neutralizer is based on the material to be etched. For copper ME08 electrolyte with N2 neutralizer was used.

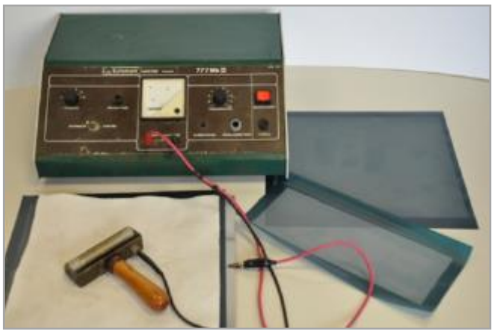

Figure 3.7: Electrochemical etching setup

The different types of circular grids used in this study are presented in Table 3.14. As in the tensile test the necking zone is small, the small sized (2 mm) grid was used. In case of bulge test the specimen with small dimension (Ø 175 mm) small sized (2 mm) grid was used and the specimen with larger dimension (Ø 250 mm) bigger sized (5 mm) grid was used. In case of the SPIF the deformation is higher and circular non-interlaced grids are helpful as they provide distinct grid measurement.

Table 3.14: Different types of circular grids etched on the copper specimen

Test	**Type and dimension of grid**	**Marked grids**
Tensile test	Inter-laced circles $d = 2\,mm$	
Bulge test	Inter-laced circles $d = 2\,mm$	
	Inter-laced circles $d = 5\,mm$	
Nakajima test and SPIF	Circular grids $d = 2.5\,mm$	

3.5 Digital Image Correlation

The necking failure limits (FLC) was obtained using circle-grid analysis. This technique is not suitable to measure the failure strain in case of shear specimen as the fracture region i.e. ligament area is very small. Further the interpolation concept to determine the fracture strains cannot be applied as the major and minor strain paths do not follow bell curve in case of shear specimen.

For these reasons Dantec® Digital Image Correlation (DIC) system was used to measure the necking failure strains (FLC) of shear specimens (see Figure 3.8). The specimen were speckled with white and black paint coloured patterns to provide contrast.

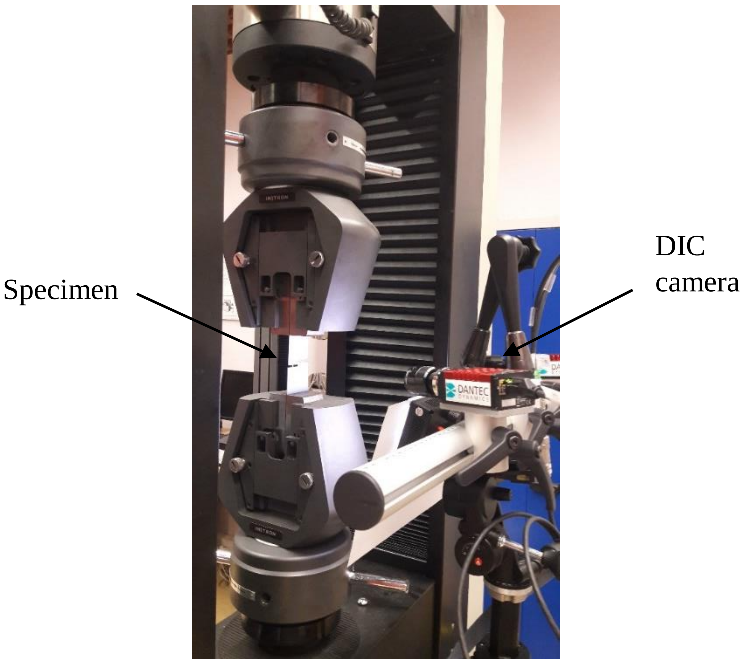

Figure 3.8: Experimental setup for staggered shear specimen with Dantec® Digital image correlation on INSTRON universal testing machine

3.6 Measurement systems

In this section the measurement systems used during this study are discussed. Specialised equipments were used to measure strains, thickness, height, roughness, geometry of formed components and the microstructure.

3.6.1 Circle grids measurement

The deformed grids (usually elliptical) are measured after the tests to determine the strains. In this study the grids are measured using a semi-automatic grid measuring technique. The methodology to calculate principal strains using circle grid is presented in section 2.1.1. The GPA® (version 3.0) software was used to analyse the deformed grids. In this technique the calibrated 3-com Home connect camera (Figure 3.9a) captures the deformed elliptical grid. The major and minor axes of this grid are processed by this software and the major and minor strains are plotted (Figure 3.9b).

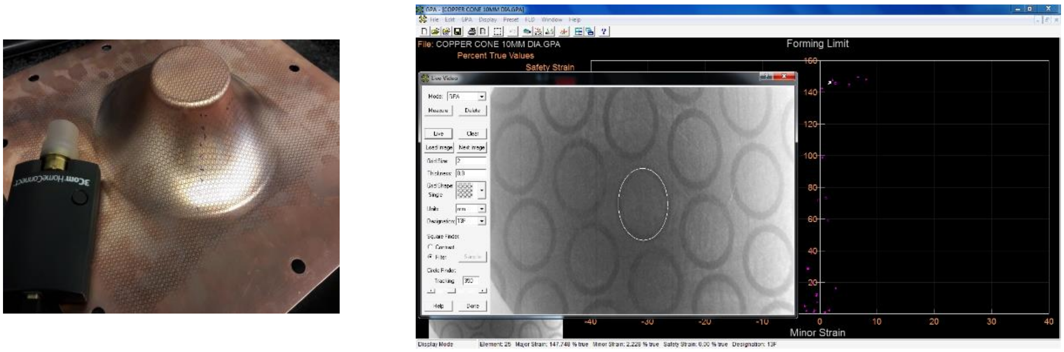

(a) (b)

Figure 3.9: GPA setup. a) GPA camera, b) GPA software processing the deformed grid

3.6.3 Thickness and width measurements

The thickness and width of test specimen are required to be measured before and after the fracture, in order to calculate the fracture strain points. The thickness of fractured test specimen is in the order of 100 μm and to measure this, precise and accurate measuring equipment of that order is required. The test specimens were cut in the deformation zone to measure the thickness under optical microscope. In order to measure the thickness of final fractured specimen, optical microscope (see Figure 3.10a) with a built-in digital camera using Motic Images Plus 2.0 ® software was used. This microscope's software allows measuring the thickness from the picture taken from the microscope's camera. The accuracy of this microscope is 0.1µm. To measure the initial width of ligament and the final width of fractured ligament, Mitutoyo® 176-901-1A Toolmaker's Microscope (see Figure 3.10b) was used. The accuracy of this microscope is 1µm.

(a) (b)

Figure 3.10: Optical microscope used in this study. a) Microscope used to measure thickness, b) microscope used to measure width

To reduce the error of measurement, for each specimen multiple measurements (more than 5) were recorded and the average value of these measurements was used for the analysis.

3.4.4 Angle measurement

The maximum forming angle (ψ_{max}) for SPIF can be determined by measuring the fracture depth in the conical geometry [47]. For this the depth at which fracture appears, d, is measured using a height calibre (see Figure 3.11). This fracture depth is correlated with the cone CAD geometry by drawing a vertical line of dimension *d*. Then the end of vertical line is projected on the curvature of the cone (see Figure 3.11b). For the given component, the angle at this intersection is the maximum forming angle, ψ_{max}.

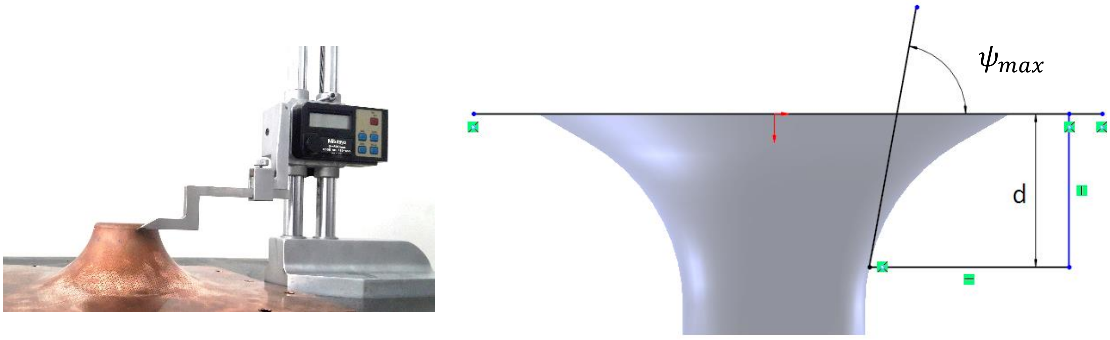

(a) (b)

Figure 3.11: Methodology to calculate maximum forming angle, a) fracture depth measurement using height calibre, b) relating fracture depth to the maximum forming angle using SOLIDWORKS®

3.6.5 Roughness measurement

The surface roughness in terms of average roughness (R_a), 10-point mean roughness depth (R_z) and maximum roughness depth (R_{max}) was measured to investigate the effect of lubrication on the surface integrity of the formed component. To analyse the surface finish of incrementally formed parts, the roughness was measured from the internal surface, where the tool was in contact with the formed the component. The formed component was cut into longitudinal narrow stripes, which allowed surface roughness measuring pin to touch the surface area properly and enabled the pin to move freely on the surface (on both upper and lower region). Roughness test is performed using HOMMELWERKE LV-50 roughness measurement equipment (see Figure 3.12).

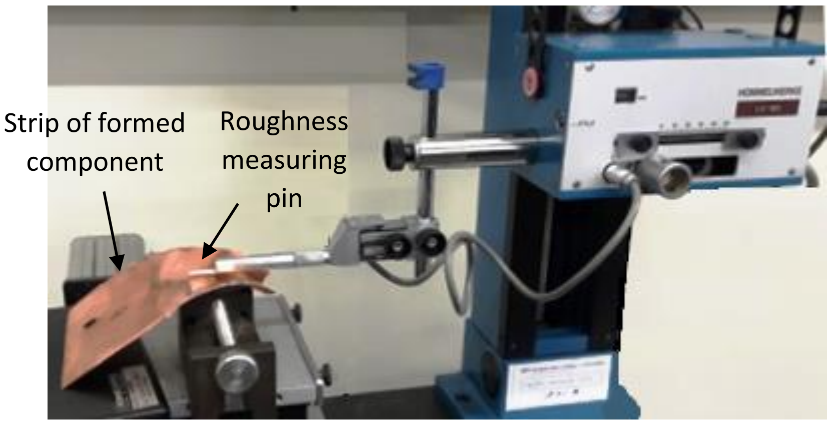

Figure 3.12: Machine used to measure the surface roughness of the formed conical geometry

3.6.6 Profile determination

The profile of the formed component was measured in order to study the effect of lubrication on the dimensional accuracy of the formed conical geometry. To measure the profile the MITUTOYO® (BX303) Coordinate Measuring Machine (CMM) was used (see Figure 3.13). Points on the profile were measured using ball tip stylus with point positioned approximately less than 5 mm apart. The points were then plotted on the graph and compared with the CAD drawing.

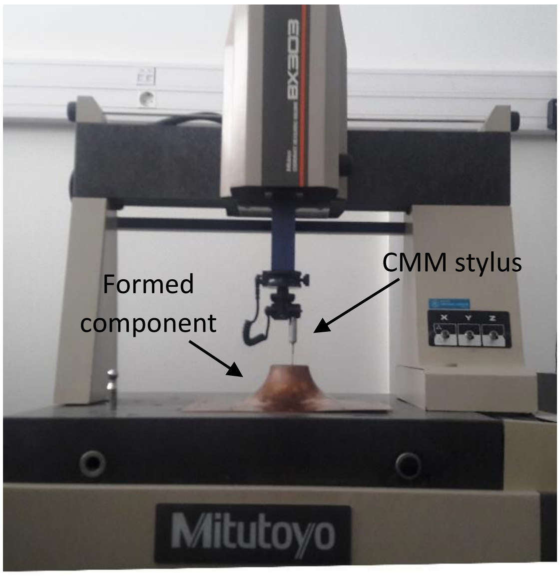

Figure 3.13: Coordinate measuring machine used to generate the formed profile

3.6.7 Microscopic analysis

Scanning electron microscope (SEM) was used to study the surface morphology of the formed component. In this study, the surface was observed to understand the effect of lubrication on the surface morphology and effect of different tool diameter on the surface. The SEM was conducted on a Scanning Electron Microscope with X-Ray Microanalysis (brand: JEOL® JSM 35C) available at University of Porto (see Figure 3.14a) and Analytical FEG-SEM: JEOL 7001F with Oxford light elements EDS detector and EBSD detector available at IST, Lisbon (see Figure 3.14b). The specimens for SEM analysis were cut from various locations of the single point incrementally formed conical geometry along the depth direction. Care was taken so as to not scratch or contaminate the surface. To avoid oxidation of the copper specimens, oil was sprayed on the specimens. Before preparing the specimen, the rolling direction and the tool path was noted.

(a) (b)

Figure 3.14: Scanning electron microscope available at, a) University of Porto, b) IST, Lisbon

In order to study the effect of lubrication on the grain size and shape, the grains boundaries were evaluated before and after the single point incremental forming. The specimens were obtained from fracture zone (lower region) and as received sheet metal. The specimens were mechanically polished along with a solution of OP-S suspension with acid. A solution of dilute hydrogen peroxide with ammonia was used to etch the specimen so that the grain boundaries were visible. The grain boundaries were observed under a metallurgical microscope – Olympus® PMG3+ DP25 (see Figure 3.15) available at INEGI.

Figure 3.15: Metallurgical microscope used to observe the grain boundaries of the specimens

Chapter 4 **Results and discussion**

In this chapter the results obtained from the experiments are presented and the implications of those results are discussed in detail. This chapter begins with the material and the fracture characterization. Later, the formability limits by necking and by fracture are presented. The effect of process parameters on the formability in the SPIF is also discussed. Later the microstructure analysis is discussed and at the end of the chapter application of the formability limits and the SPIF applications are presented.

4.1 Material Properties

In this section the material properties obtained from the tensile and the bulge tests are presented. The stress-strain curves obtained from tensile tests (specimens cut in 0º, 45º and 90º with respect to rolling direction of the copper sheet metal) is presented in Figure 4.1.

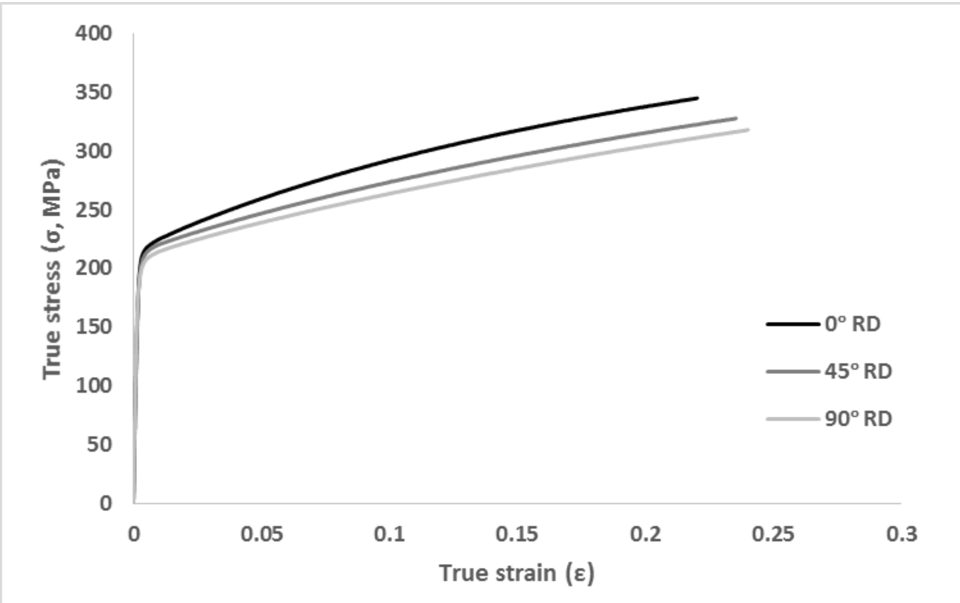

Figure 4.1: True stress-strain curve for copper obtained from tensile test

It can be observed from Figure 4.1, that the true stress-strain curve for all test specimens (cut in 0º, 45º and 90º with respect to rolling direction) are similar in nature. The curve for specimen with 0º rolling direction lies slightly above than that of specimen with 90º rolling direction. The mechanical properties obtained from tensile test are presented in Table 4.1.

Table 4.1: Material properties of copper

Angle with rolling direction	Modulus of elasticity, E (GPa)	Yield stress, σ_Y (MPa)	Ultimate tensile stress, σ_{UTS} (MPa)	Elongation, A (%)	Normal anisotropy coefficient	Planar anisotropy coefficient
0º RD	109.43	213.24	343.52	24.17	0.79	
45º RD	109.49	207.62	327.49	27.11	1.19	
90º RD	128.96	207.06	326.77	28.20	0.74	
Mean values	**141.33**	**208.89**	**331.32**	**26.65**	**$\bar{r}$ =0.98**	**Δr= -0.43**

The normal anisotropy ($\bar{r}$) of copper is 0.98 which indicate a very less deviation of material properties in different directions with respect to rolling direction. The negative value of planar anisotropy suggests that thinning is more prominent when specimen cut in 45º with respect to rolling direction is loaded than when specimen cut in 0º or 90º with respect to rolling direction is used.

The standard uniaxial tensile test cannot provide a range of stable uniform strain and is restricted to almost half than that obtained from biaxial bulge tests [91]. In order to ascertain the material law precisely, the biaxial true stress-strain was obtained from hydraulic bulge test.

The true strain-strain curve obtained using hydraulic bulge test is presented in Figure 4.2 along with true stress-strain curve obtained from tensile test.

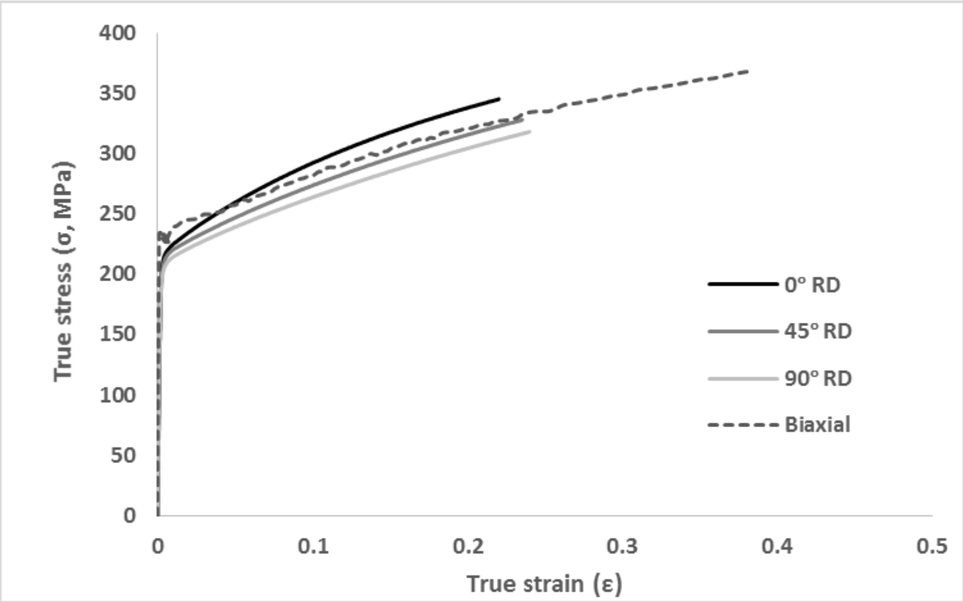

Figure 4.2: Biaxial true stress-strain curve for Copper obtained from Bulge test

It can be observed from Figure 4.2 that the maximum strain in case of stress-strain curve obtained from tensile test has the value of 0.23 whereas the maximum strain in case of stress-strain curve obtained from bulge test has the value of 0.38. This means that additional information on the strain hardening property is obtained from the stress-strain curve obtained from the bulge test. The material law is obtained by applying mathematical approximation technique to the true stress-strain curve obtained from the bulge test. Table 4.2 presents the material laws obtained for copper using different empirical relationships.

Table 4.2: Material property using different empirical relationships

Ludwik - Hollomon or Power law	Swift law	Voce law
$\sigma = 427.56\ \varepsilon^{0.1719}$	$\sigma\ = 457.35(0.0752 +\ \varepsilon)^{0.2747}$	$\sigma = 230.02 + 201.02\ (1 -\ e^{-3.025\ \varepsilon})$

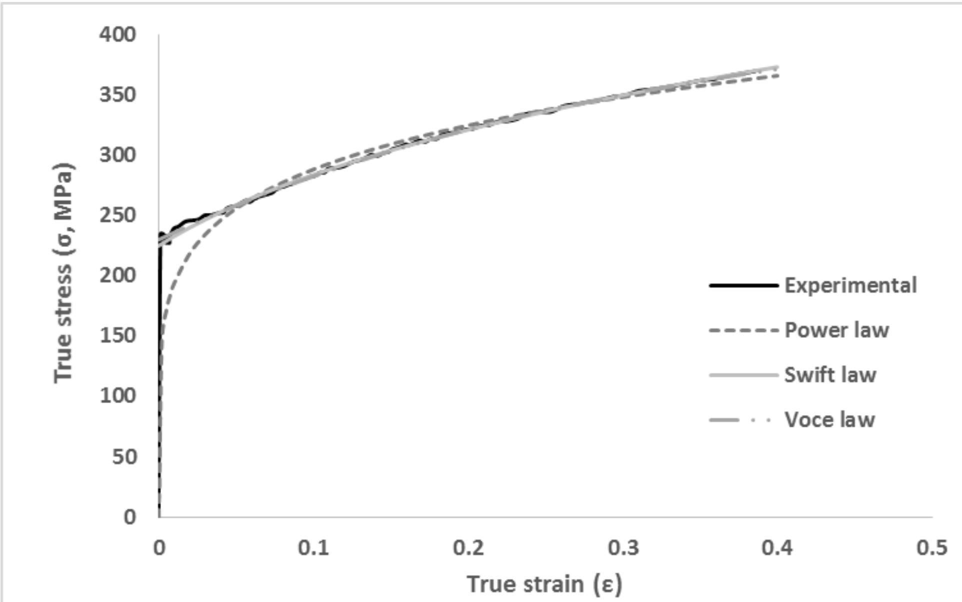

Figure 4.3: Comparison of different material laws with the experimental stress-strain curve

The Swift law and the Voce law, both describe the material law accurately (see Figure 4.3). The curve obtained from Voce law fits the experimental stress-strain curve with the confidence of 99.88% and Swift law fits the experimental stress-strain curve with the confidence of 99.86%.

4.2 Fracture toughness

In this section fracture toughness obtained for fracture by mode I, mode II and mixed mode I&II of fracture mechanics are presented. The methodology used to calculate these values is presented in section 2.1.3.

Fracture toughness for fracture by mode I of fracture mechanics was obtained using double notch tensile test (DNTT) specimens, for which the experimental plan is presented in Chapter 3. The specimen fractured along the ligament, as shown in Figure 4.4.

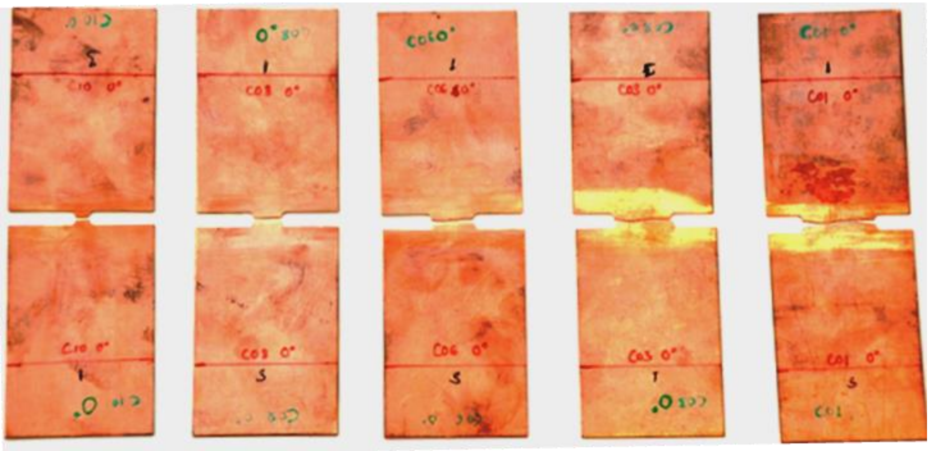

(a) (b) (c) (d) (e)

Figure 4.4: Double notch tensile test specimens after fracture with ligament size a) 5 mm, b) 10 mm, c) 15 mm, d) 20 mm and e) 25 mm

The force-displacement curves obtained for the DNTT specimens from the experiment, are presented in Figure 4.5.

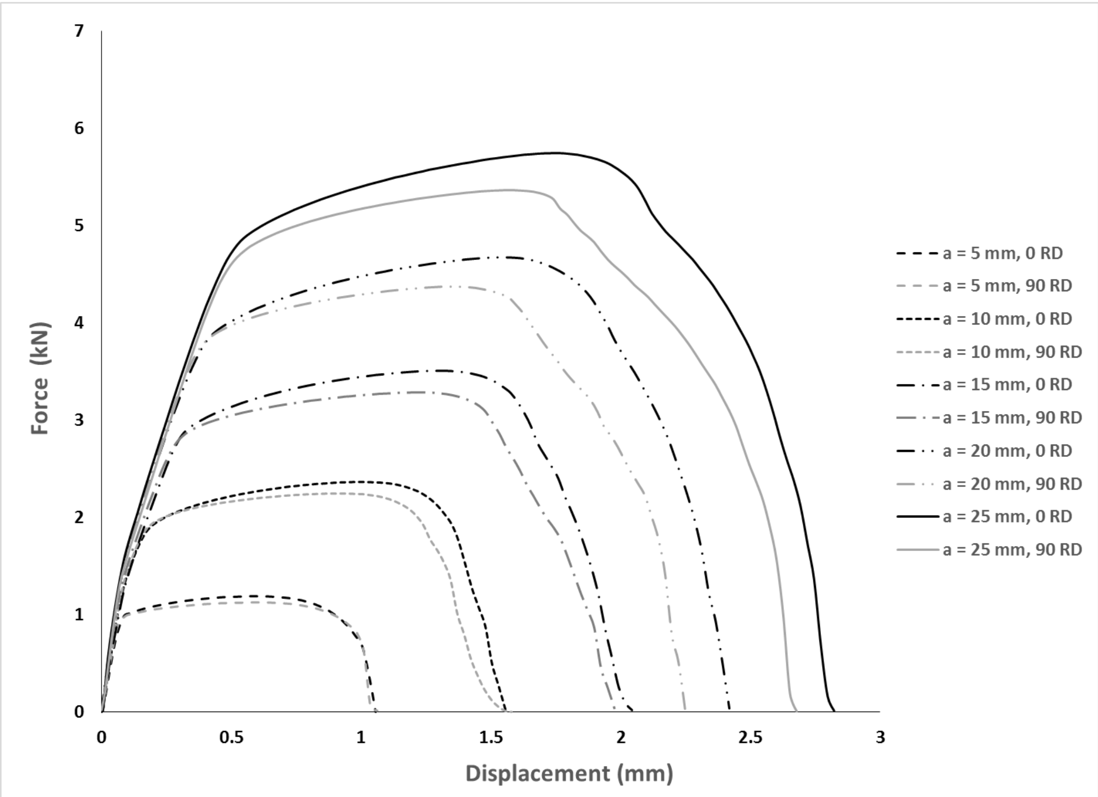

Figure 4.5: Force-displacement curve obtained from experiment for DNTT specimen

The ‘a’ in the legend of Figure 4.5, indicate the ligament length for the specimen, ‘0 RD’ indicate that the specimen was cut in 0º with respect to rolling direction and ‘90 RD’ indicate that the specimen was cut in 90º with respect to rolling direction. It can be observed from Figure 4.5, that the effect of orientation of rolling direction is minimal for the smaller ligament lengths (a = 5 mm and 10 mm). As the ligament length increases the area under force-displacement curve also increases. The area under the force-displacement curve is the energy required for the plastic deformation and for the fracture.

The methodology to obtain the value of fracture toughness from the given force-displacement curve is presented in section 2.1.3. The linear curve fitting was done to obtain the fracture toughness from the points obtained on the energy per unit area vs ligament size graph and is presented in Figure 4.6. The value of y-coordinate where the linear curve intercepts the y-axis is considered the fracture toughness, R_I.

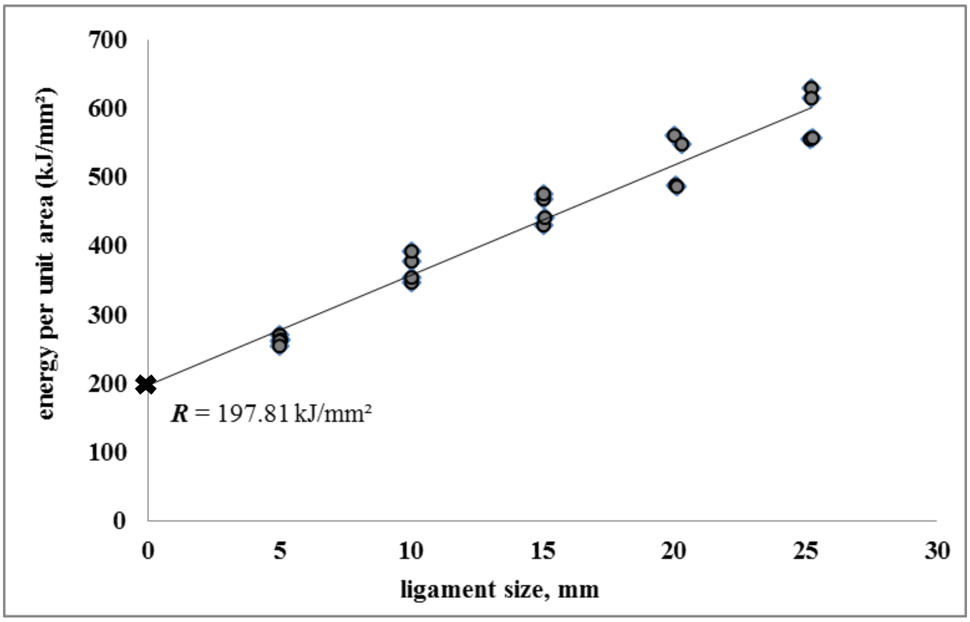

Figure 4.6: Fracture toughness calculation for fracture by mode I of fracture mechanics

The essential work of fracture or the fracture toughness, R_I for copper when the fracture is by mode I of fracture mechanics is 197.81 kJ/mm^2.

Fracture toughness for fracture by mode II of fracture mechanics was obtained by means of V-slit shear specimens and C-slit shear specimens, presented in Chapter 3 along with the experimental plan.

The C-slit shear specimens fractured along the ligament for a = 2, 3, 4 and 6 mm, as shown in Figure 4.7a. The V-slit shear specimens with a = 1, 2 and 3 mm fractured along the ligament (see Figure 4.7b) but specimens with higher ligament length (a = 4, 6 and 8 mm) did not fracture in the ligament area (see Figure 4.7c and Figure 4.7d). The fracture did not propagate in the ligament direction but perpendicular to the ligament. This perpendicular fracture propagation was because of the fact that the fracture propagates in path which offers least resistance, and the less area in perpendicular direction (to the ligament) offers the path of least resistance. To overcome this problem the V-slit shear specimen with increased width was designed and the fracture propagated in the ligament direction.

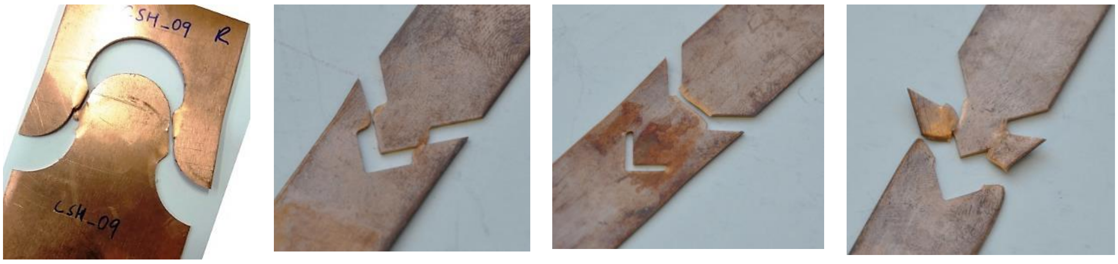

(a) (b) (c) (d)

Figure 4.7: Shear specimens, a) C-slit shear specimen with ligament size 6 mm, b) V-slit shear specimen with ligament size 2 mm, c) V-slit shear specimen with ligament size 8 mm, d) c) V-slit shear specimen with ligament size 4 mm

The force-displacement curves obtained for the shear specimens from the experiment, are presented in Figure 4.8.

The ‘a’ in the legend of Figure 4.8, indicate the ligament length for the specimen, ‘0 RD’ indicate that the specimen was cut in 0º with respect to rolling direction and ‘90 RD’ indicate that the specimen was cut in 90º with respect to rolling direction, ‘V sh’ indicate the V-slit shear specimen (with width = 25 mm), ‘n V sh’ indicate the V-slit shear specimen (with width = 40 mm) and ‘C sh’ indicate the C-slit shear specimen.

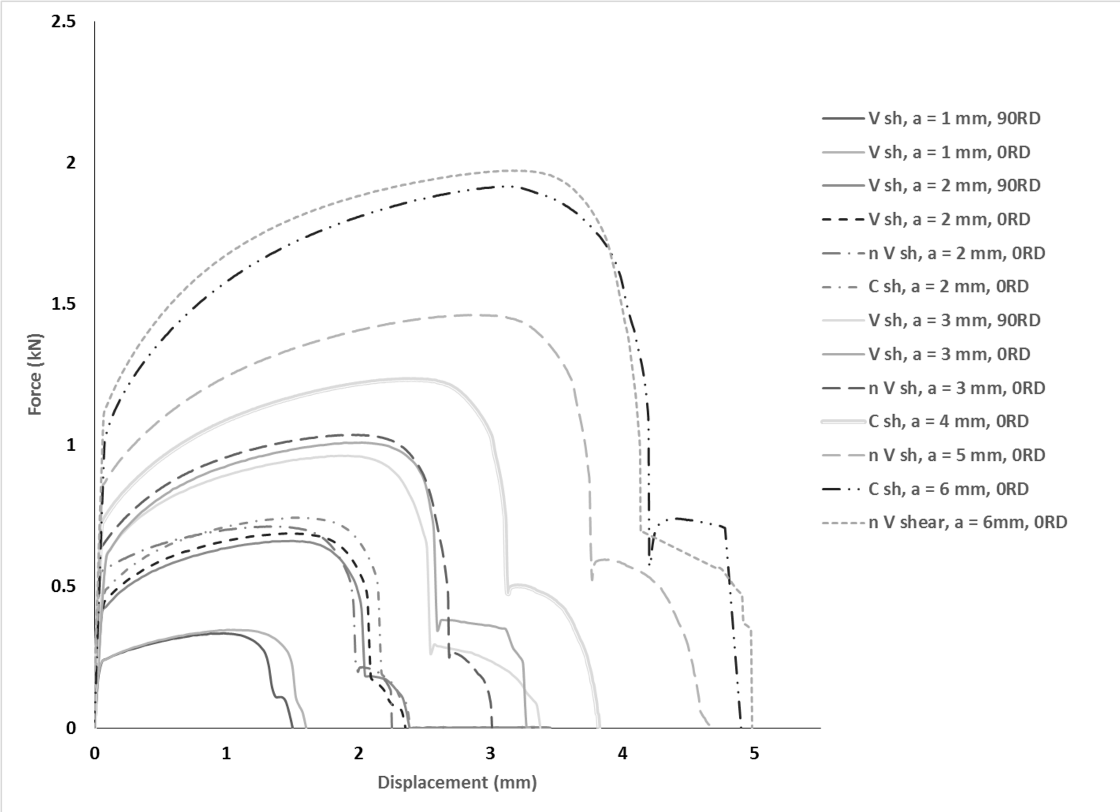

Figure 4.8: Force-displacement curve for shear specimen obtained from experiment

It can be observed from Figure 4.8, that the effect of orientation of rolling direction is minimal for the smaller ligament lengths (a = 1, 2 and 3 mm). As the ligament length increases the area under force-displacement curve also increases. The area under the force-displacement curve is the sum of energies required for the plastic deformation and for opening the crack (or fracture). Another important observation in the Force-displacement curve is the slight increase in force before fracture, and this is because the specimens have two ligaments and both of them do not fracture at the same time.

The methodology to obtain the value of fracture toughness from the given force-displacement curve is presented in section 2.1.3. The linear curve fitting was done in order to obtain the fracture toughness for fracture by mode II of fracture mechanics, and is presented in Figure 4.9. The value of y-coordinate where the linear curve intercepts the y-axis is considered the fracture toughness, R_{II}.

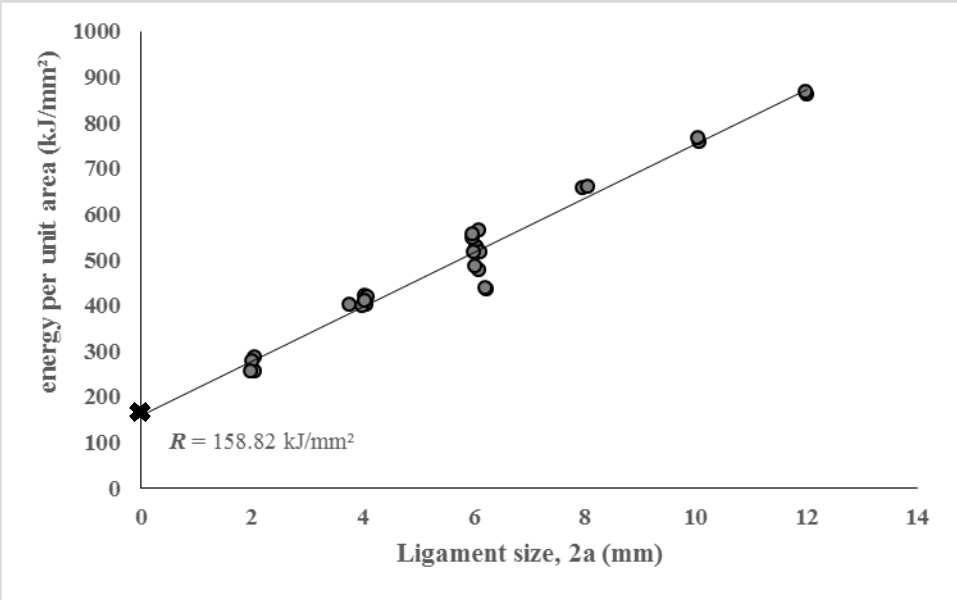

Figure 4.9: Fracture toughness calculation for fracture by mode II of fracture mechanics

The essential work of fracture or the fracture toughness, R_{II} for copper when the fracture is by mode II of fracture mechanics is 158.82 kJ/mm^2.

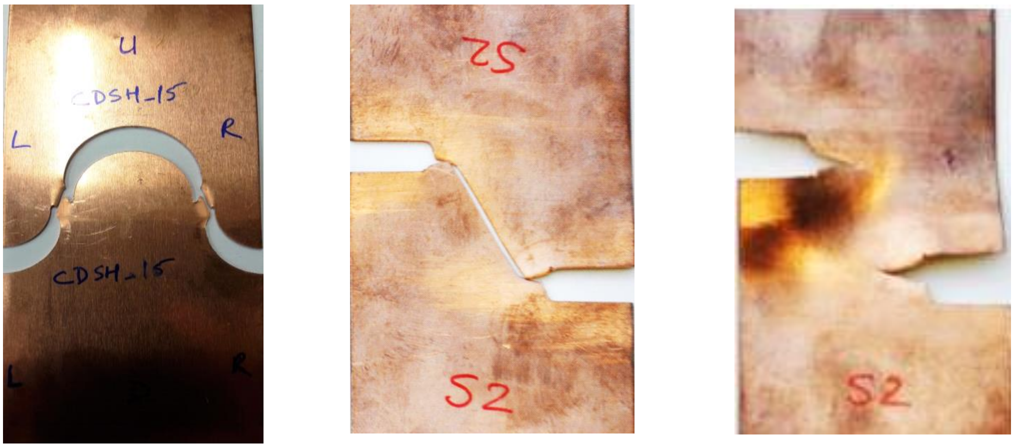

(a) (b) (c)

Figure 4.10: Staggered specimen fractured by mixed mode I&II of fracture mechanics, a) staggered C-slit specimen with ligament size 2 mm and deviation of 2.5 mm, b) staggered DNTT with ligament size 15 mm and c) staggered DNTT with ligament size 20 mm

To obtain fracture toughness for fracture by mixed mode I&II of fracture mechanics staggered DNTT and staggered C-slit specimens were used. The experimental plan is presented in Chapter 3. The staggered C-slit shear specimen (s-C-slit specimen) fractured along the ligament (see Figure 4.10a). The staggered DNTT (s-DNTT) specimen fractured along the ligament (see Figure 4.10b) for a = 5, 10 and 15 mm, whereas did not fracture along ligament direction for a = 20 and 25 mm. The force-displacement curves obtained for s-DNTT specimens are presented in Figure 4.11.

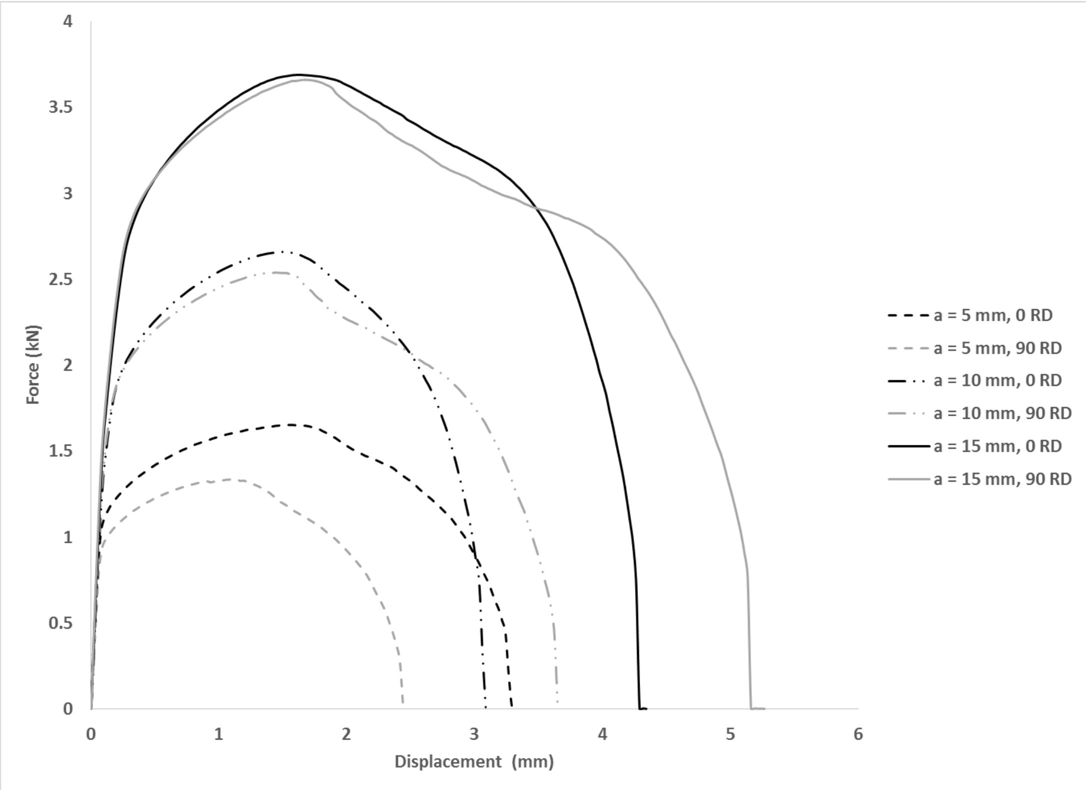

Figure 4.11: Force-displacement curve for s-DNTT specimens obtained from experiment

The orientation of rolling direction affected the force-displacement curve and the obtained fracture toughness, R_{II} = 350.4 kJ/mm^2, is very high. The fracture principal strains obtained from staggered DNTT specimens lied far below the Shear Fracture Forming Limit (SFFL) and Fracture Forming Limit (FFL). Thus the results obtained from staggered DNTT are not satisfactory and were discarded. For calculating fracture toughness and fracture strain for fracture by mixed mode I&II of fracture mechanics only staggered C-slit specimen were used.

The force-displacement curves obtained for the s-C specimens from the experiment, are presented in Figure 4.12. It can be observed from Figure 4.12, that as the ligament length increases the area under force-displacement curve also increases. The area under the force-displacement curve is the sum of energies required for the plastic deformation and for the fracture. Another important observation in the Force-displacement curve is the slight increase in force before fracture, and this is because the specimens have two ligaments and both of them do not fracture at the same time

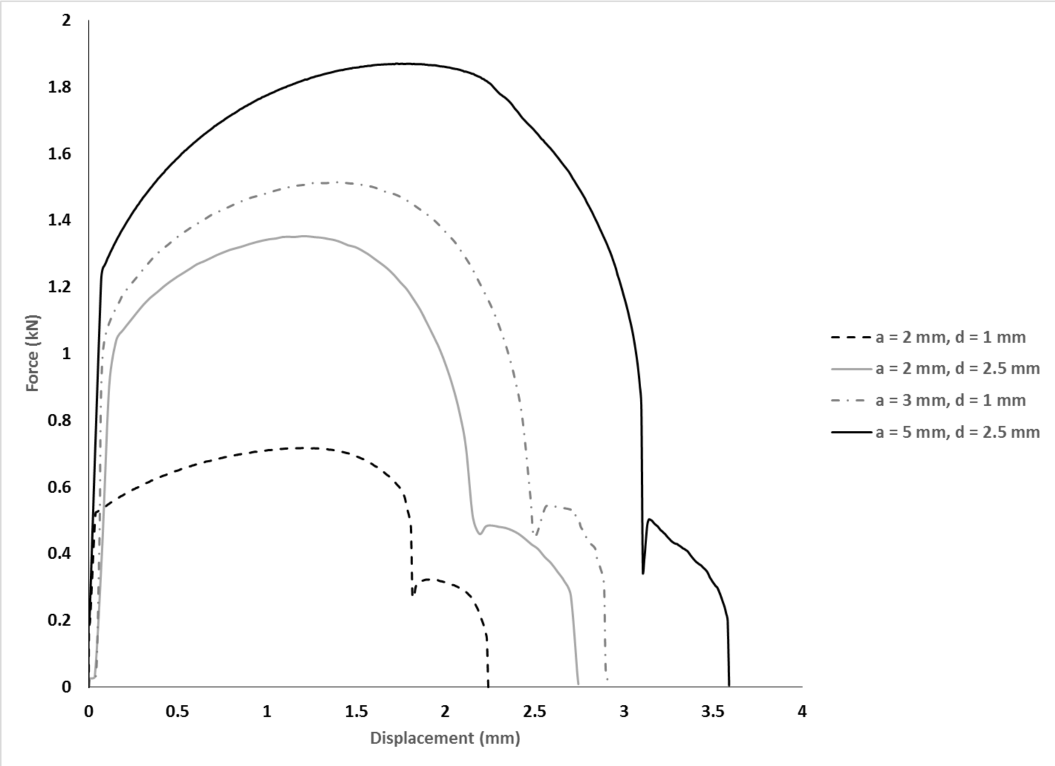

Figure 4.12: Force-displacement curve obtained for staggered C-shaped specimen

The methodology to obtain the value of fracture toughness from the given force-displacement curve is presented in section 2.1.3. The linear curve fitting was done in order to obtain the fracture toughness for fracture by mixed mode I&II of fracture mechanics, and is presented in Figure 4.13. The value of y-coordinate where the linear curve intercepts the y-axis is considered the fracture toughness, $R_{I\&II}$.

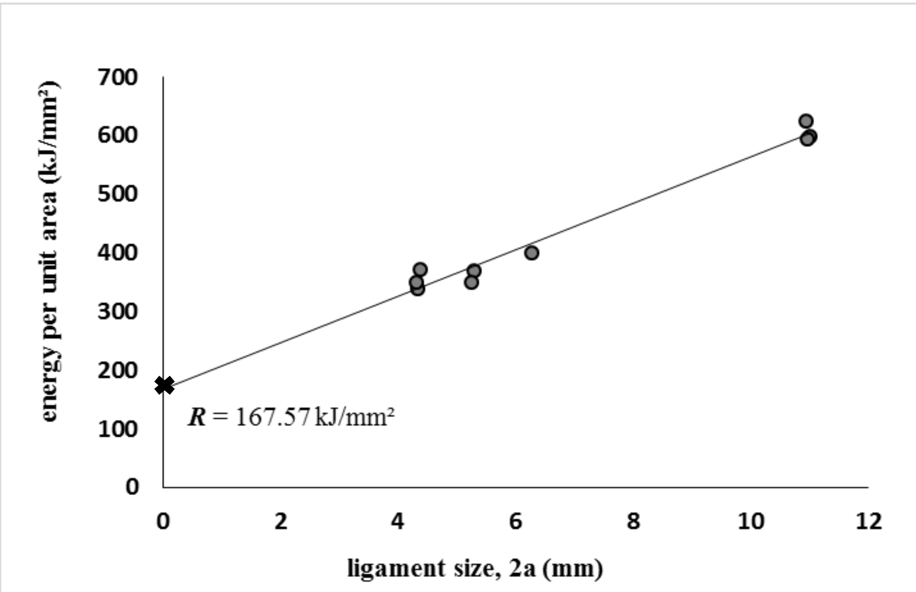

Figure 4.13: Fracture toughness calculation for fracture by mixed mode I&II of fracture mechanics

The essential work of fracture or the fracture toughness, $R_{I\&II}$ for copper when the fracture is by mixed mode I&II of fracture mechanics is 167.57 kJ/mm^2.

All the values of fracture toughness for copper in different modes of fracture are presented in Table 4.3.

Table 4.3: Values of fracture toughness

Property	**Mode I**	**Mode II**	**Mixed Mode I&II**
Fracture toughness (kJ/mm^2)	197.81	158.82	167.57

The value of fracture toughness is minimum when the fracture occurs by mode II of fracture mechanics and is maximum when the fracture occurs by mode I of fracture mechanics. The value of fracture toughness for fracture by mixed mode I&II of fracture mechanics lies between R_I and R_{II}.

4.3 Formability limits by necking and fracture

In this section the forming limit curve (FLC), the fracture forming limit (FFL) and the shear fracture forming limit (SFFL) obtained using tensile, DNTT, Nakajima, bulge, shear and staggered test are presented. The methodology to obtain the forming limits is explained in detail in Chapter 2.

Figure 4.14 shows the FLC and the SFFL strain points for copper obtained using shear and staggered specimens. ‘V-shear’ in the legend indicate the V-slit shear specimen points, ‘C-shear’ in the legend indicate the C-slit shear specimen, ‘staggered C-shear’ indicate the s-C slit shear specimen strain points and ‘staggered DNTT’ indicate s-DNTT fracture strain points on the FLD. It can be observed that the s-DNTT fracture strain points lie far below the SFFL and are incorrect. Thus these specimen are not very good to determine the fracture strain points for copper sheet metal.

The solid filled mark in Figure 4.14 indicate the corresponding limiting fracture strain point for the given limiting localization strain. They are connected by dashed line representing the changes in strain paths towards plane strain conditions.

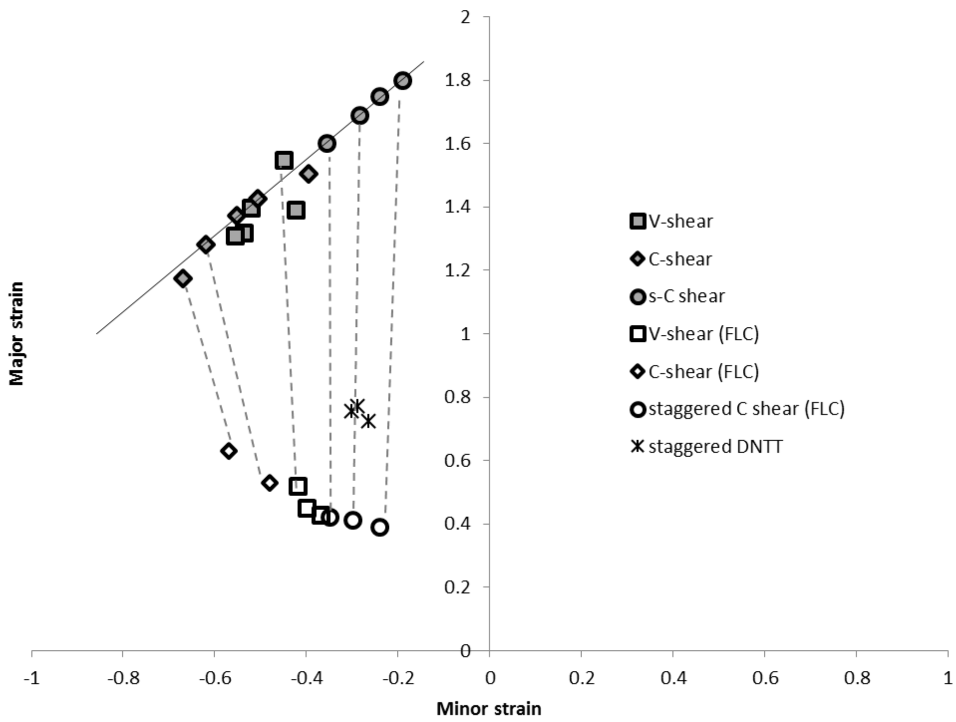

Figure 4.14: Failure strain points obtained for shear specimen and staggered shear specimens

The graphical interpretation of the points lying on the SFFL in FLD is presented in Figure 4.15. It can be observed that as the ligament size of the shear specimen increases the fracture strain shift towards right side on the SFFL in FLD.

The fracture strain points obtained from C-slit shear specimen with smaller ligament size (i.e. 2 mm and 3 mm) lie lower towards left side (approx. $\varepsilon_2/\varepsilon_1 =$ -0.5) on the SFFL. As the ligament's size increase the strain points rise towards the right side on the SFFL. The V-slit shear specimen's fracture strain points almost lie in same region (approx. $\varepsilon_2/\varepsilon_1 =$ - 0.36) for all the ligament size unlike the fracture strains of C-slit shear specimen, which are spread out on the SFFL (from region $\varepsilon_2/\varepsilon_1 =$[-0.5,-0.27]). The staggered C-slit shear specimen's fracture strain points lie higher up, towards right side ($\varepsilon_2/\varepsilon_1 =$ -0.14) on the SFFL. This shift of shear specimen from $\varepsilon_2/\varepsilon_1 =$ -0.5 to $\varepsilon_2/\varepsilon_1 =$ -0.14 on SFFL is due to the fact that the ligament's loading changes from almost pure shear ($\alpha =$ -1) to mixed mode ($\alpha = 0$).

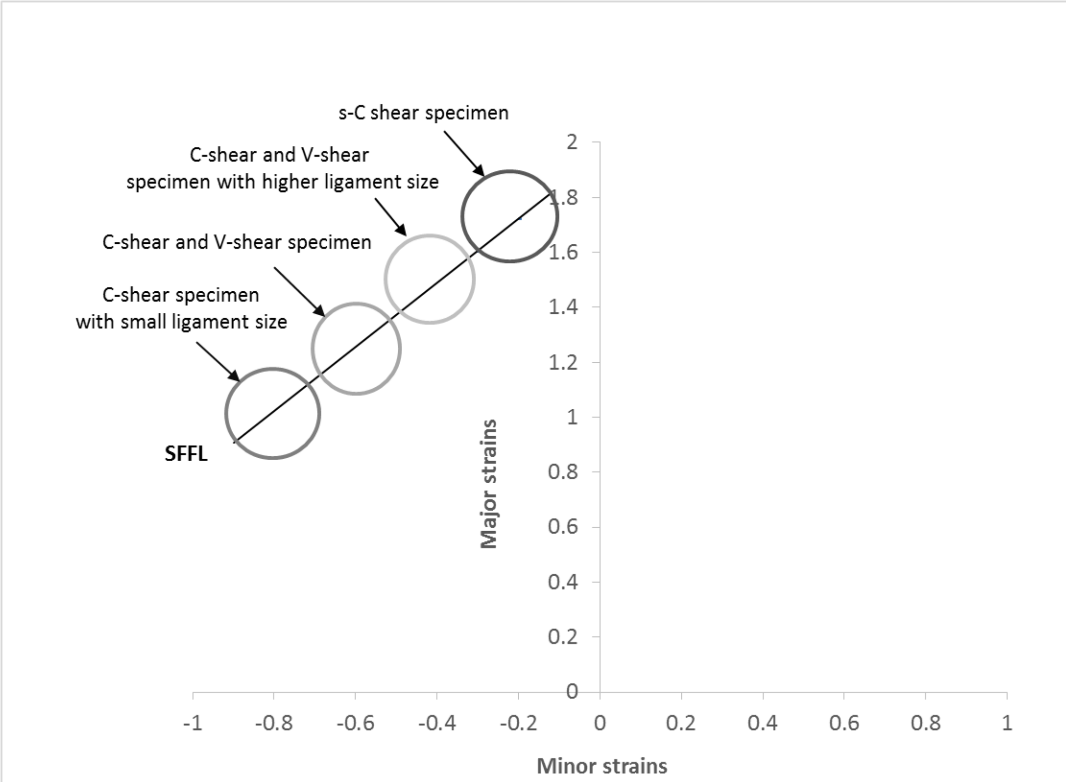

Figure 4.15: Graphical interpretation of fracture strains on SFFL obtained from shear and staggered specimens

The circle grid technique was used to measure the necking failure strain points of the tensile, the bulge and the nakajima specimens. The DIC system was used to determine the necking failure strain points for V-slit, C-slit and s-C slit shear specimens. The methodology used to determine the fracture strain points in presented in section 2.1.2 and was used to determine fracture strain points of all the specimens. The obtained FLD with SFFL and FFL is presented in Figure 4.16.

From Figure 4.16 we can observe that the FFL and SFFL lie far above FLC. This indicate the higher ductility of the material. The solid filled markers in Figure 4.16 indicate the corresponding limiting fracture strain point for the given limiting localization strain connected by dashed lines that represent the changes in strain paths towards plane strain conditions.

The expression for the FFL and the SFFL are:

$$\text{FFL: } \varepsilon_1 = -1.923\varepsilon_2 + 1.548 \quad (4.1)$$

$$\text{SFFL: } \varepsilon_1 = 1.205\varepsilon_2 + 2.033 \quad (4.2)$$

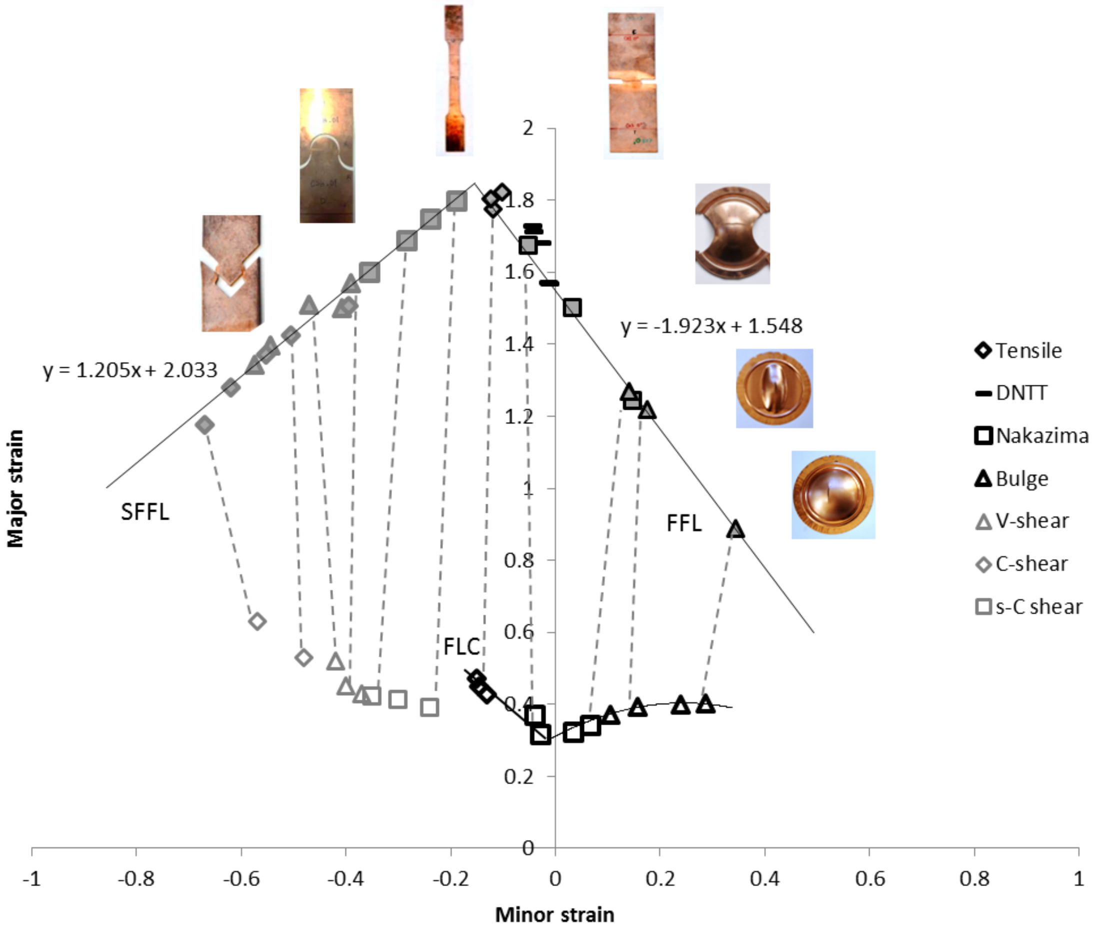

Figure 4.16: Forming limit diagram with forming limit curve, fracture forming limit and shear fracture forming limit lines obtained for copper

In the Forming Limit Diagrams (FLD) (see Figure 4.16) it is observed that the SFFL is linear and is approximately perpendicular to FFL. It also shows that the intersection of SFFL and FFL is that of intersection of two lines with fracture strain loci obtained from mixed mode I&II of fracture mechanics, lie in the this intersection region.

The slope of FFL theoretically should be -1 [5]. But the slope of FFL obtained from the FLD (see Figure 4.16) shows slope of -1.92. The slope of FFL is prominently deviating from theoretical value but is consistent and coherent from all the tests performed to obtain the FFL. The slope of SFFL theoretically should be +1 [5]. The slope obtained from both FLD shows slope of 1.20 which is close to theoretical values.

4.4 Formability limits by SPIF geometries

In this section the SPIF forming limits is discussed. The experimental setup and experimental plan is explained in Chapter 3. The strain paths for each geometry used and its corresponding fracture strain (marked with solid fill markers on graph) are presented in Figure 4.17.

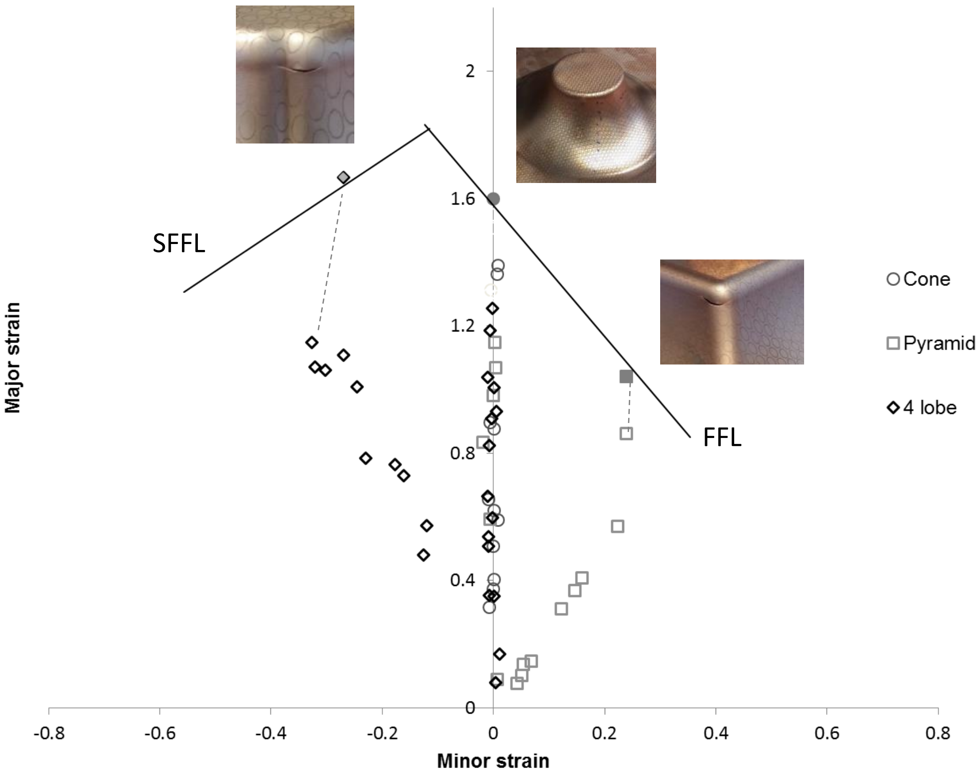

Figure 4.17: Forming limit diagram containing Fracture forming limit and Shear fracture forming limit obtained for copper using single point incremental forming

It can be observed from Figure 4.16 and Figure 4.17 that the forming limits for SPIF can be characterised by FFL, obtained from conventional sheet metal test like tensile test, bulge test and Nakajima test and SFFL, obtained by shear and staggered tests.

It can be observed from Figure 4.17 that the strain path for truncated conical geometry formed till fracture is in plane strain zone. This means that the principal minor fracture strain is ideally zero. The principal major fracture strain thus can be assumed to be formability indicator in the case of truncated conical geometry.

4.5 Effect of process parameters on formability limits in SPIF

In this section the effect of the various process parameters, like forming tool diameter, tool geometry, tool material, feed rate, step down and lubrication on formability of SPIF is discussed. The experimental setup and work plan is presented in Chapter 3. In order to analyse these effects a truncated conical geometry with varying angle [47] was considered and to quantify its formability the test were performed till fracture. To measure the formability the principal major strain at fracture was used.

4.5.1 Effect of forming tool on formability

Two different forming tool geometries (hemispherical end and spherical end forming tool presented in section 3.3.2) were used with different tool diameters to study the effect of the forming tool on the formability. The effect is graphically presented in Figure 4.18.

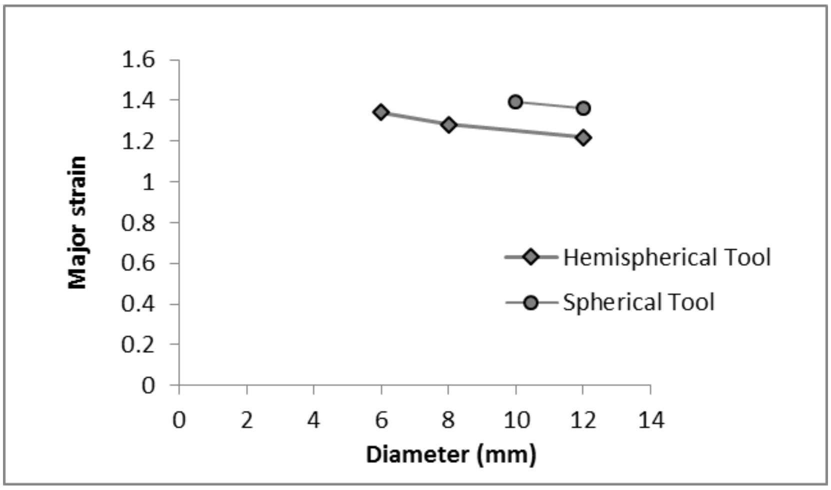

Figure 4.18: Effect of the tool diameter on the formability in single point incremental forming

It can be observed from Figure 4.18 that when the spherical end tool is used the formability is higher compared to hemispherical end forming tool, for the same diameter. As the forming tool diameter increases the formability decreases. This is because as the radius of tool approaches the component radius the advantage of increased formability due to localised deformation is not available [21], [24].

In order to study the wear effect of the forming tool in SPIF three different materials, PM300, CK40 steel and tungsten-carbide (discussed in section 3.3.2) under the same process parameters (presented in Table 4.4) were used to form the truncated conical shape. No lubricant was used for all the tool conditions. Microscopic images of the tool tips after test were taken to understand the wear of tool. Figure 4.19 depicts the tool tip images after the forming.

Table 4.4: Process parameters used for the experiment

Spindle speed	Feed rate	Step down	Tool path
Free rotation	1000 mm/min	0.15 mm	Spiral

In the case of PM300 (Figure 4.19d) and CK40 (Figure 4.19e), it is visible a significant copper adhesion on the tool tip due to the fact that copper is the softer material. The tool wear and material adhesion for the tungsten-carbide forming tool (Figure 4.19f) is much lower than the two other forming tools (Figure 4.19d and Figure 4.19e). The use of tungsten-carbide as tool material to form Copper sheet metal almost completely avoids adhesion and is thus recommended.

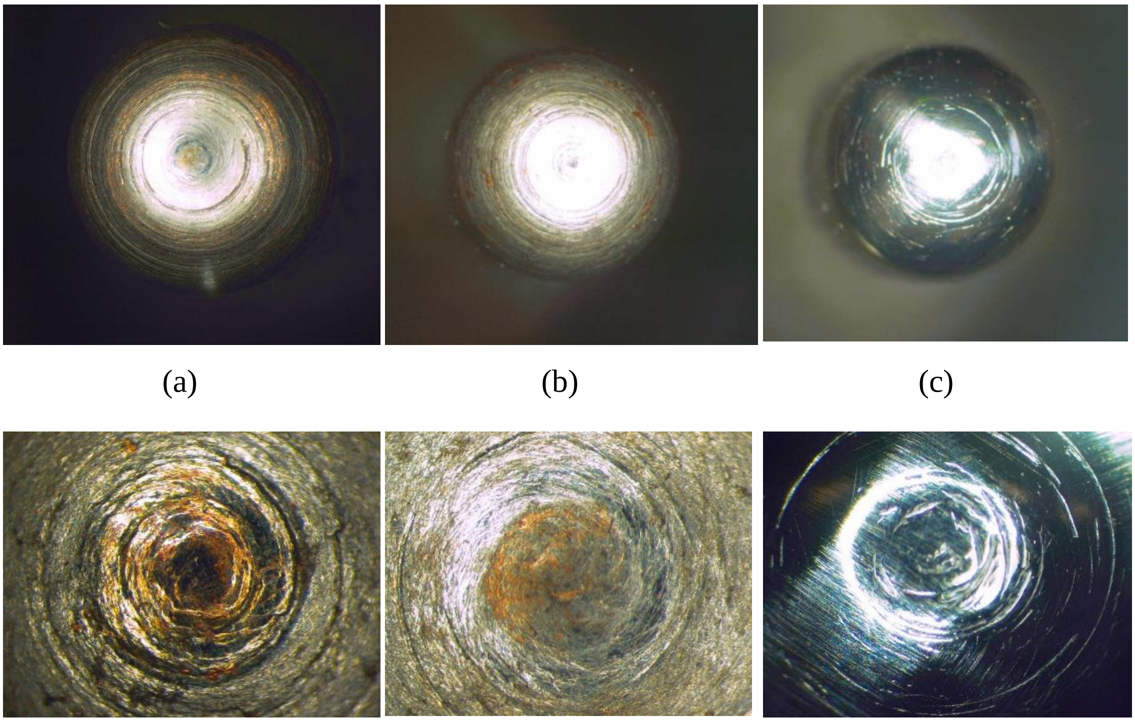
(a) (b) (c)
(d) (e) (f)

Figure 4.19: Microscopic image of the tool tip a) PM300, b) CK40, c) Tungsten-carbide, d) PM300 (3x), e) CK40 (3x) and f) Tungsten-carbide (3x)

The effect of tool material (PM300 and Tungsten-carbide) on the formability in SPIF was evaluated and the results are presented in Figure 4.20.

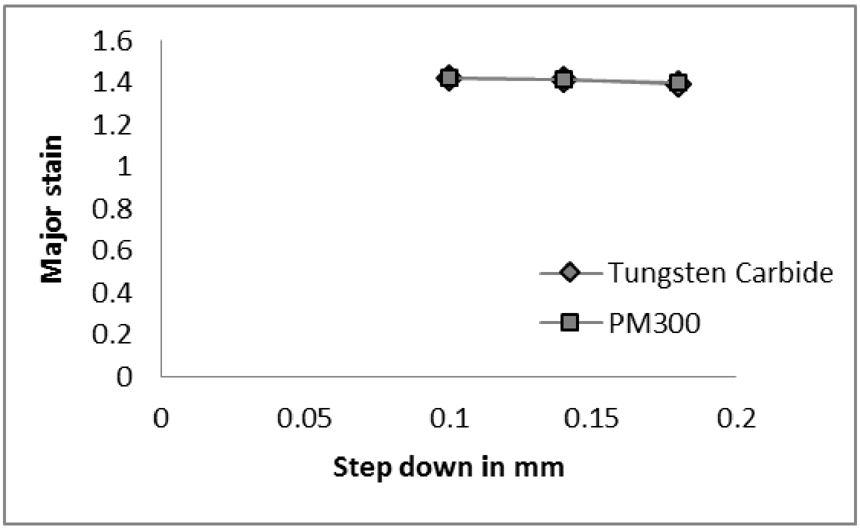

Figure 4.20: Effect of tool material on SPIF formability

It can be observed from Figure 4.20 that formability limits for copper does not have any effect when the forming tool material is changed.

4.5.2 Effect of step down on formability

In order to evaluate the effect of the step down on the formability limits in SPIF, a truncated conical geometry was formed till fracture for three different step downs, viz. 0.1 mm, 0.14 mm and 0.18 mm. When the step down more than 0.18 mm was used the machine exceeded the maximum axial force. A step down smaller than 0.1 mm would increase the forming time considerably. Thus the minimum step down of 0.1 mm and maximum of 0.18 mm was used for the experiments. The effect of the step down on formability is presented in Figure 4.21.

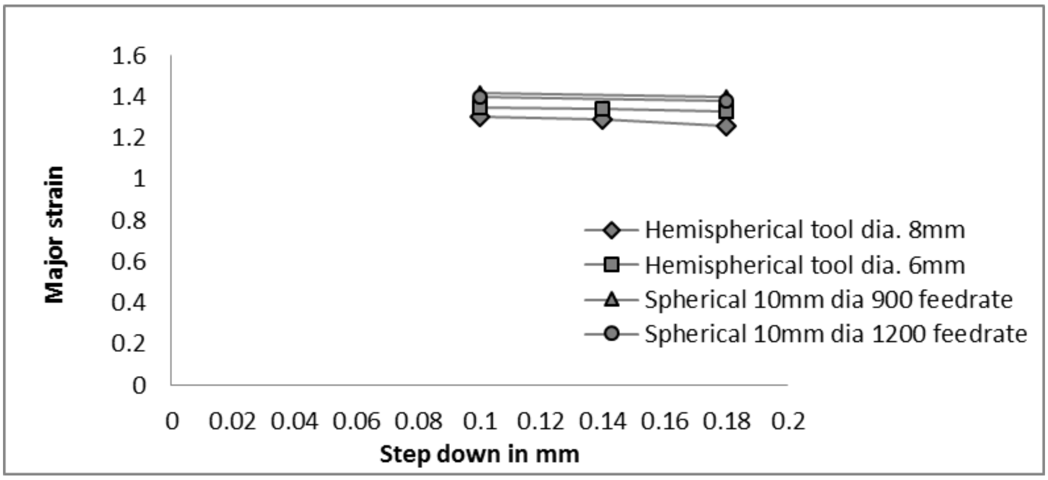

Figure 4.21: Effect of Step down on the formability

It can be observed from Figure 4.21 that when the step down is increased the formability decreases. When the step down is increased the tool-sheet contact area increases causing the decrease in formability. Lower step down causes more progressive deformation which is helpful to increase formability limit in SPIF [61].

4.5.3 Effect of feed rate on formability

To investigate the effect of feed rate on the formability in SPIF, a truncated conical geometry was formed till fracture, for three different feed rates, viz. 900 mm/min, 1050 mm/min and 1200 mm/min. The effect of increase in feed rate on the formability is presented in Figure 4.22.

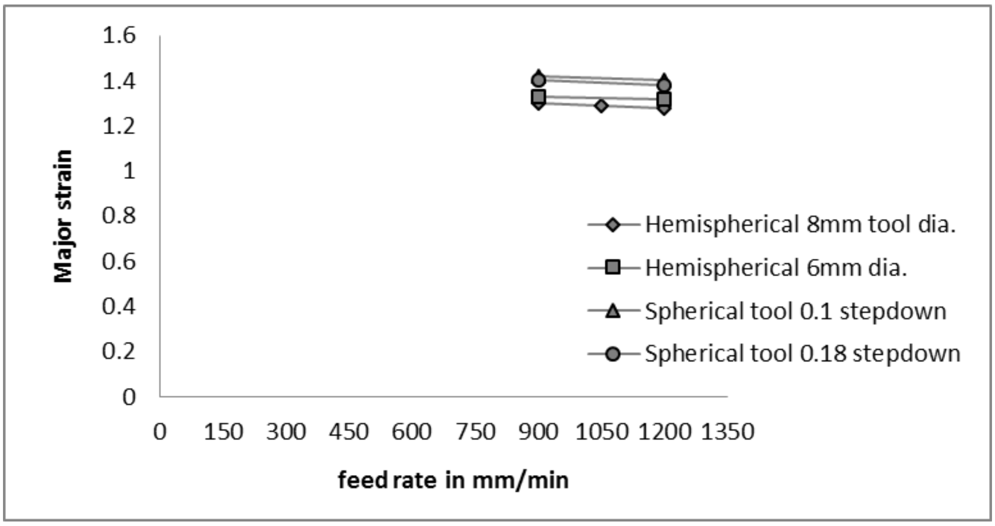

Figure 4.22: Effect of feed-rate on formability

There is no significant deviation in formability when the feed rate is increased. Slight decrease might reflect the fact that when the strain rate in sheet metal increases the work hardening area decreases (i.e. total plastic deformation decreases) [61].

4.5.4 Effect of lubrication on formability

Different lubrication conditions as described in Chapter 3 where used to determine the effect of lubrication on formability and surface roughness. The effect of the studied lubrication conditions on formability is presented in Table 4.5, in terms of major fracture strain and maximum forming angle.

Table 4.5: Effect of different lubrication conditions on the formability

Lubrication condition	Major fracture strain	Maximum forming angle (ψ in deg)
1	1.34	76.1
2	1.34	76.5
3	1.34	76.9
4	1.34	76.4
5	1.35	77.4
6	1.33	76.0

It can be inferred from Table 4.5 that there is no significant effect of lubrication on the resultant fracture strains. However lubrication condition 5, has a negligible positive effect on the fracture strain. Also it can be observed from Table 4.5, that there is no significant effect of lubrication on maximum forming angle. However lubrication condition 5, has a negligible positive effect on the maximum forming angle.

As the truncated conical geometry formed in this study is symmetrical, analysing only one profile along the component surface is sufficient to judge the effect of the lubrication on the final geometry (see Figure 4.23). Here it was observed that there was no significant effect of lubrication on the profile. Figure 4.23 presents the formed geometry for each lubrication condition and the corresponding CAD geometry. The formed geometry is significantly deviating from the CAD model and this is due to spring-back effect.

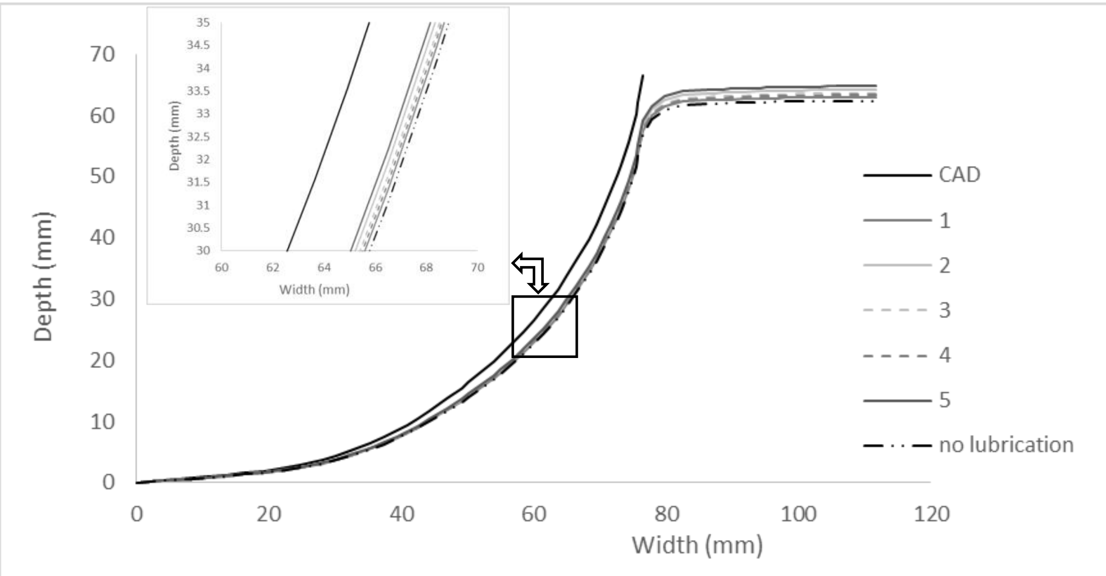

Figure 4.23: Effect of different lubrication conditions on the profile deviation of a section in the truncated conical geometry formed using SPIF

4.5.5 Effect of lubrication on the surface roughness

In order to study the effect of different lubrication conditions conical geometry was formed till fracture using Tungsten-carbide 12 mm spherical ball end forming tool.

For all lubrication conditions, there is no effect of lubrication condition on the fracture strains, maximum forming angle and the deformed profile (i.e. on formability). In case of lubrication condition 2 (AS40), there were visible stains on the surface of formed component, thus this lubrication condition is not recommended for copper sheet metal forming.

It was observed that the surface roughness, measured from internal side of the component (the side with forming tool contact), varied substantially in the Upper and the Lower region (see Figure 4.24). The surface roughness values at both these locations are presented in Table 4.6, for all lubrication conditions.

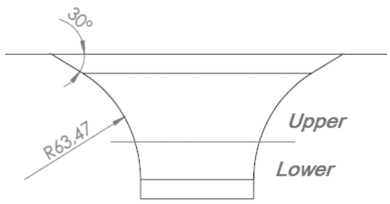

Figure 4.24: Truncated conical geometry indicating upper and lower region

Table 4.6: Effect of different lubrication conditions on surface roughness

Lubrication condition	**Quantity of Lubricant (g)**	**R_a (µm)**		**R_z (µm)**		**R_{max} (µm)**	
		Upper region	Lower region	Upper region	Lower region	Upper region	Lower region
undeformed	-	0.102		0.573		0.74	
1	25.81	0.695	0.965	4.273	4.980	5.413	6.650
2	31.93	0.567	1.010	3.267	6.317	3.870	8.303
3	37.69	0.422	0.517	2.513	3.687	2.730	5.323
4	45.06	0.435	0.496	2.640	3.537	3.293	4.700
5	18.96	0.393	0.465	2.043	3.247	2.507	4.217
6	no lubrication	0.720	1.020	4.310	5.220	5.650	6.820

Where, R_a is average roughness, R_z is the 10-point mean roughness and R_{max} is the largest single roughness depth with evaluated length.

From Table 4.6 it can be inferred that the surface roughness increases after the SPIF process, as expected. It was observed that the surface roughness in the Lower region, i.e. near the fracture zone is higher than that of the corresponding Upper region for all lubrication conditions. In order to better understand this variation, SEM analysis for all the lubrication conditions and regions of the specimen was conducted. Figure 4.25 and Figure 4.26 provide the SEM images at the Upper and the Lower regions for all the lubrications conditions, respectively.

4.6 Surface morphology and Microstructure Analysis

It can be inferred from the SEM images (Figure 4.25 and Figure 4.26), that the increase of the surface roughness at different regions (Upper and Lower) is because of the development of ‘valleys’ along the grain boundary, known as ‘fragmentation’, in the Lower region (indicated in Figure 4.27).

The values of R_z and R_{max} (from Table 4.6) provide an estimation of depth of the developed fragmentation. It can be observed that the depth of fragmentation is affected by the lubrication state. One of the aspects that affect the fragmentation is the contact between the tool and the sheet. The parameter that affects these aspects will affect the fragmentation depth as well.

The lubrication conditions where the lubricant is in paste state i.e. lubrication conditions 1, 2, 3 and 4, the tool marks are more visible and may suggest these type of paste lubricants need special application technique in order to improve its presence between tool and sheet interface to reduce tool marks. The surface roughness is best when lubrication condition 5 (i.e. mineral oil) is used for SPIF of copper sheet metal. It is visible that lubrication conditions 5, show scarcity of tool marks and this also contribute to a lower surface roughness.

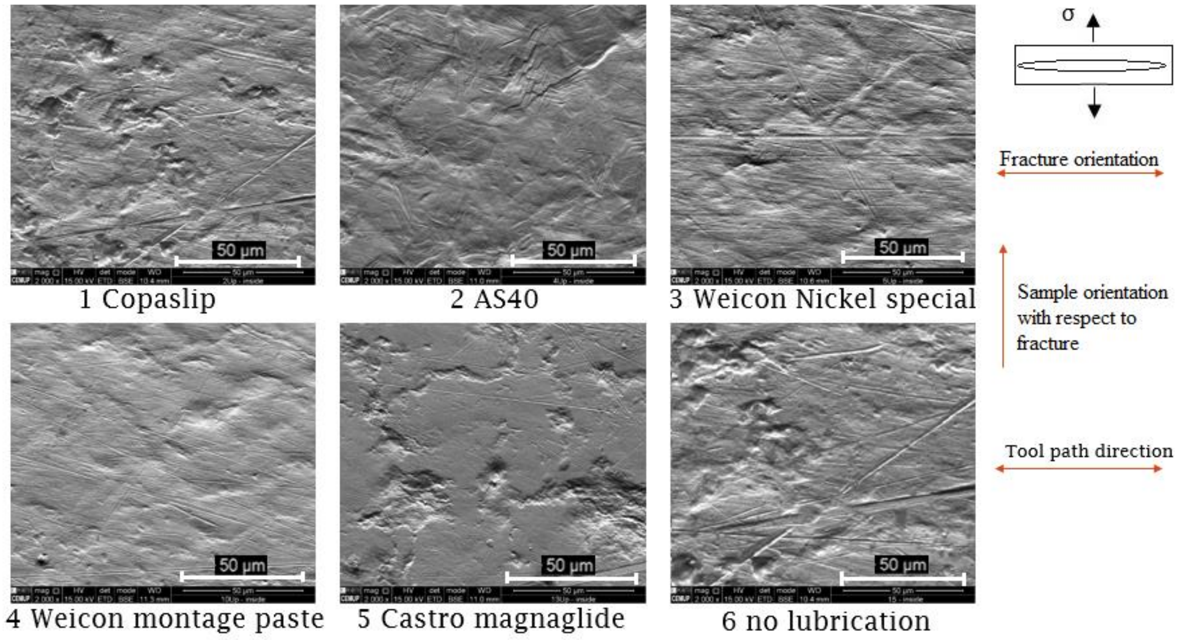

Figure 4.25: SEM images of specimen from inner upper side of formed component under different lubrication conditions

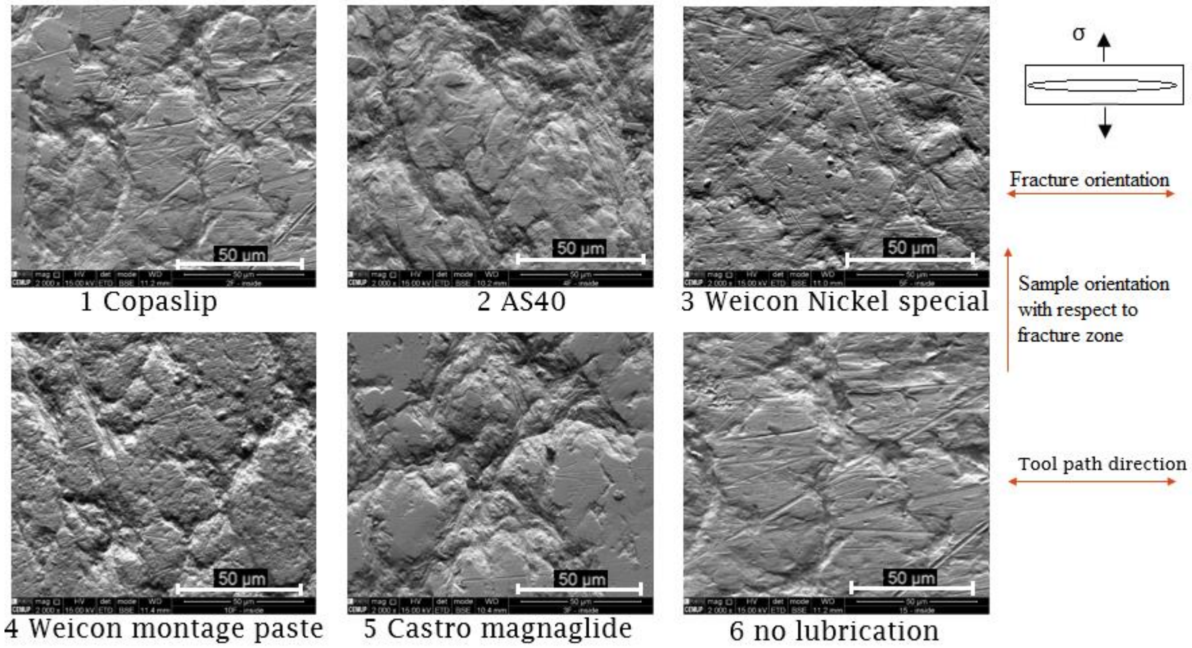

Figure 4.26: SEM images of specimen from inner lower side of formed component under different lubrication conditions

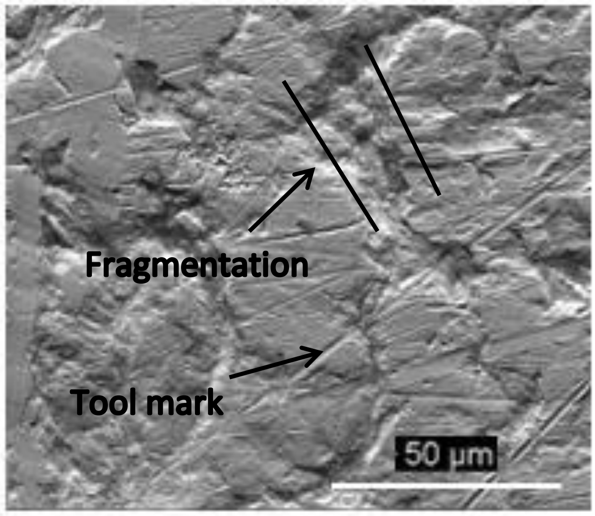

Figure 4.27: SEM (2000x) of Lower region to indicate fragmentation and tool mark

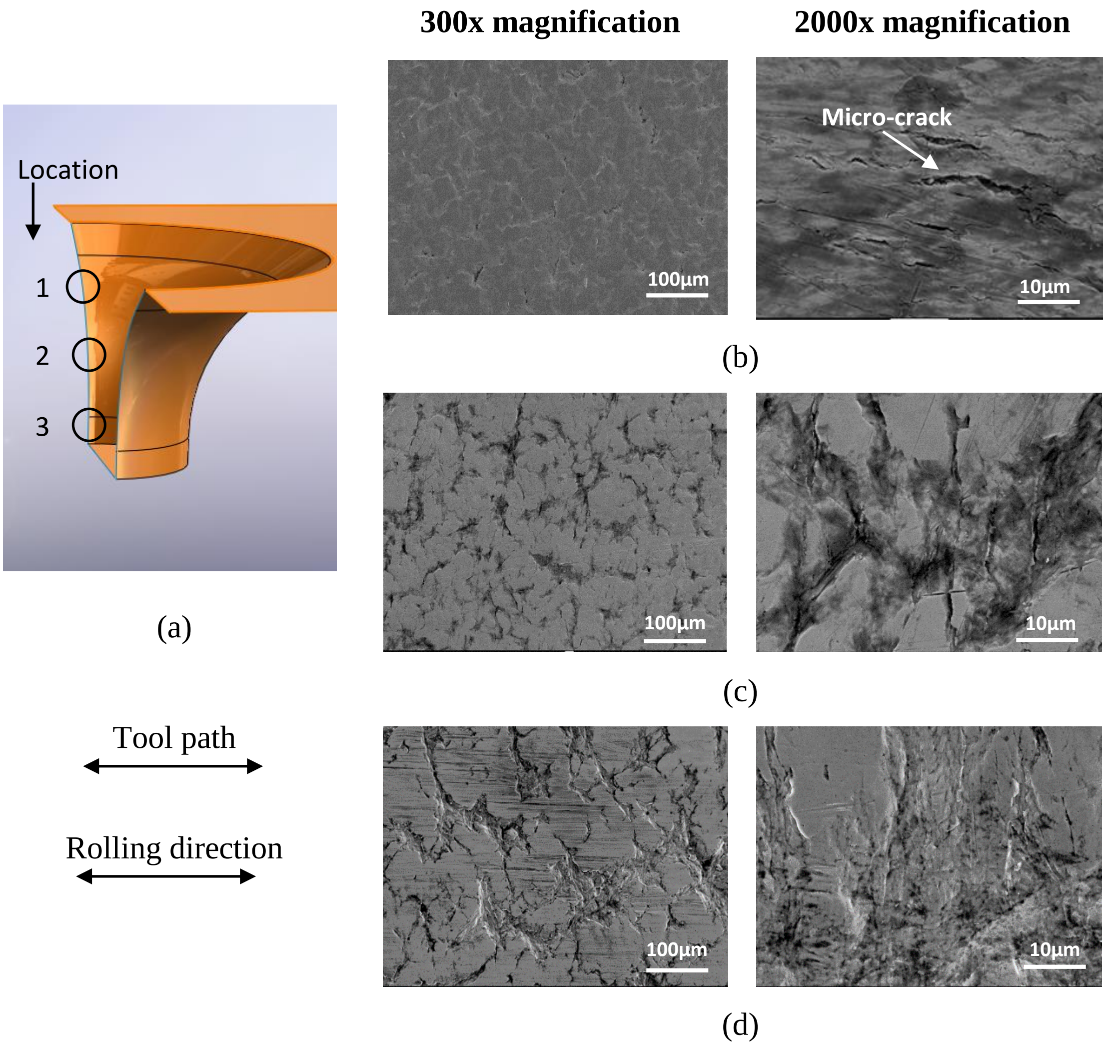

Figure 4.28: a) Sample locations taken for SEM from inner side of formed component; b) SEM for location 1; c) SEM for location 2; d) SEM for location 3

The SEM analysis of the fractured truncated conical SPIF components was performed along the depth of the wall, in order to evaluate different strain levels. The strains for each location are presented in Table 4.7. Figure 4.28 presents the schematic representation of the component and the location from where the SEM images where taken. The SEM samples were obtained from the inner side of the component, where the spherical end forming tool (diameter 10 mm) was in contact with the surface.

Table 4.7: Corresponding strains at different depths as shown in Figure 4.28a

Location	Major strain	Minor strain
1	0.19	-0.021
2	0.93	-0.020
3	1.39	0.016

From the SEM images shown in Figure 4.28, we can observe that all the locations have fragmentation microstructures, and these become more prominent when moving towards the facture area, from location 1 (Figure 4.28b) to location 3 (Figure 4.28d). It can also be observed that at location 1 (Figure 4.28b) micro-cracks start developing.

With the aim to investigate the influence of the tool contact on the surface microstructure, samples were taken from inner (surface with tool contact) and outer side (surface with no tool contact), see Figure 4.29.

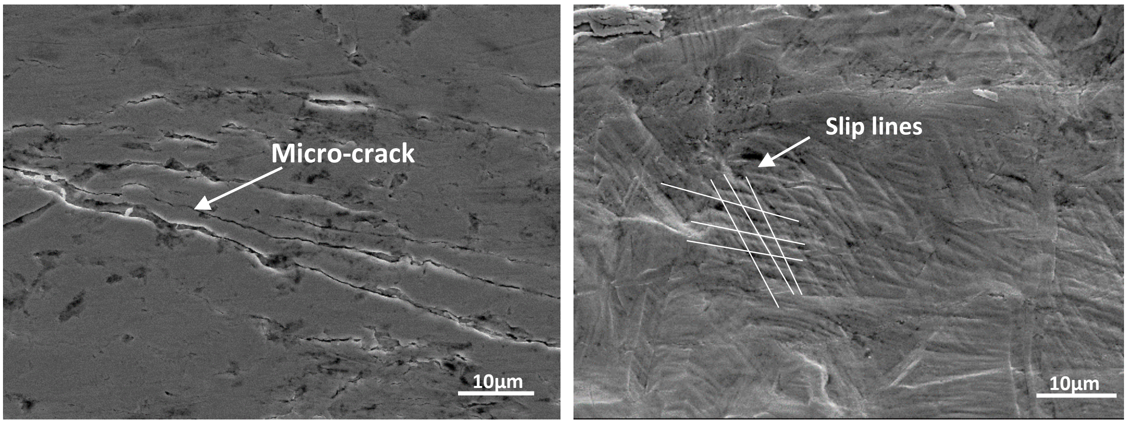

(a) (b)

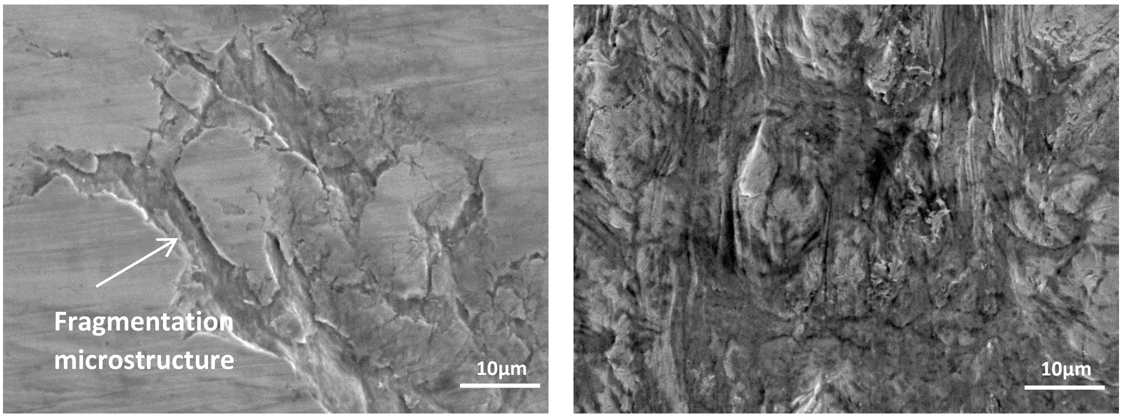

(c) (d)

Figure 4.29: SEM image (scale of 10µm) from location 1 a) inside, b) outside; and location 3 c) inside, d) outside

The SEM images taken from the inner surface shows micro-cracks at location 1 (Figure 4.29a) and a fragmentation microstructure that increases with an increase in strain (Figure 4.29c). The outer surface SEM images show the formation of slip lines at location 1 (Figure 4.29b) which leads to the fragmentation microstructure formation at location 3 (Figure 4.29d). The set of activated slips lines (Figure 4.29b) indicate a complex or multi-directional loading [92], and it can be concluded that the SPIF deformation mechanism is not only due to pure tension or pure shear. This can be related with observed stress-triaxiality in the SPIF [21].

The fracture area was observed under the SEM, and is presented in Figure 4.30.

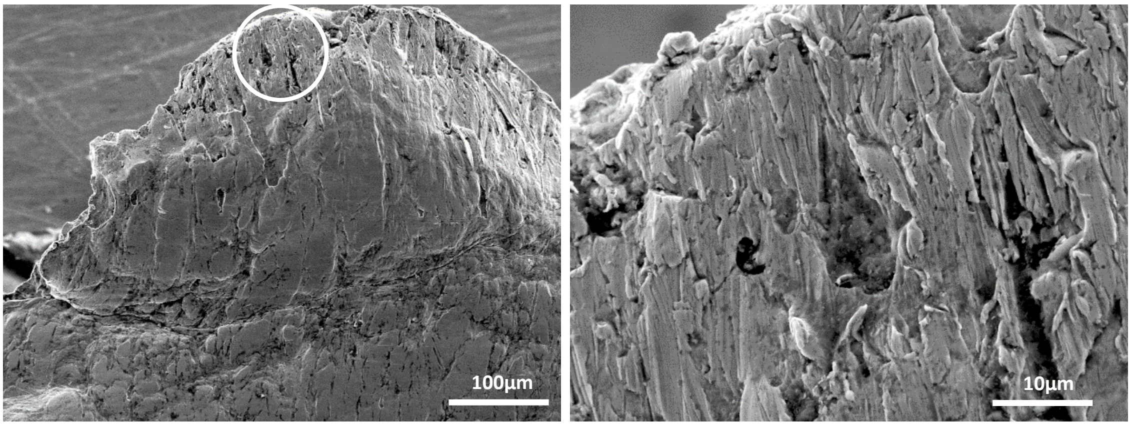

(a) (b)

↕ Rolling direction ↔ Tool path

Figure 4.30: a. SEM image at fracture zone; b) magnification of circled zone in Figure 4.30a

Figure 4.30a reveals several micro-cracks caused by cyclic loading which led to considerable damage. The alignment of the fracture ligaments are is that of ductile fracture, which confirms the fracture by mode I of fracture mechanics typical for truncated conical SPIF geometries [24]. From the SEM analysis at the fracture area, it can be concluded that the fracture has a ductile nature and it does not have serration [93] typical from fatigue failure.

In order to evaluate the influence of the tool diameter on the surface microstructure, truncated cones with two different tool diameters (spherical end forming tool of 10 mm and 12 mm diameter) under identical forming parameters where formed using SPIF. The formability results for the two conditions are presented in Table 4.8.

Table 4.8: Formability results for different tool diameters

Tool diameter	r_{part}/r_{tool}	ψ_{max}	ε_1	ε_2
10 mm	16.00	76.99°	1.39	0.016
12 mm	13.33	75.48°	1.36	0.010

Where, r_{part}/r_{tool} is the ratio between the part radius and tool radius, ψ_{max} is the maximum forming angle, ε_1 is the maximum principal major strain and ε_2 is the principal minor strain.

The results, as seen in Table 4.8, show a slightly higher formability when the 10 mm diameter forming tool is used.

Figure 4.31 presents the SEM analysis near the fracture area (location 3) from inner side for the both (10 mm and 12 mm forming tool diameter) experiments.

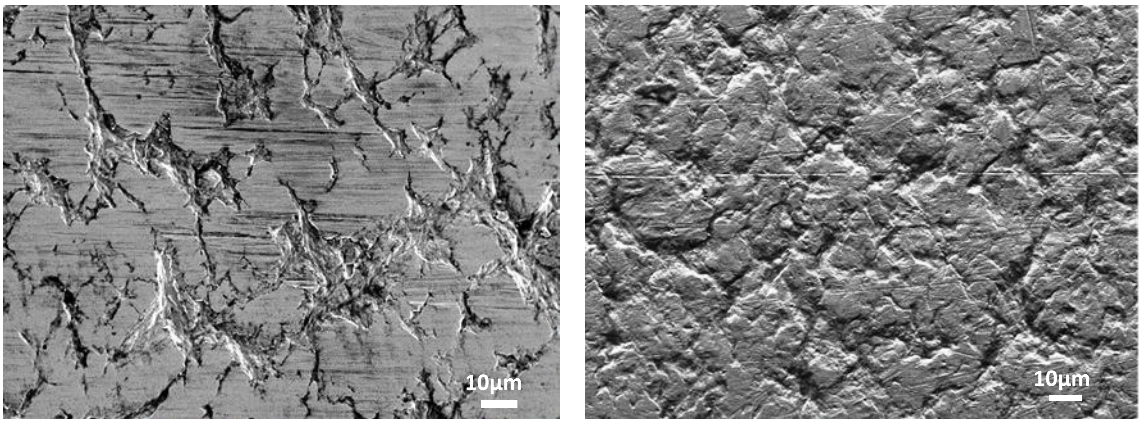

(a) (b)

Figure 4.31: Surface microstructure a) for 10 mm dia. tool; b) for 12 mm dia. tool

It can be observed from Figure 4.31 that the density of the fragmentation has increased with an increase of the tool diameter, verifying that the radius of curvature of the formed crystal lattice, which is a function of the radius of forming tool, is directly proportional to the resultant fragmentation density [94]. Having a smaller fragmentation density resulting from the deformation with a 10 mm tool diameter, it is possible to accommodate more plastic deformation before fracture, which may lead to an increase of formability as shown in Table 4.8.

It can be concluded from the SEM study that the cyclic loading causes considerable damage in SPIF, which may result in reduced reliability of the component as damage is cumulative. The activated slip system in the microstructure indicates that SPIF has complex and multidirectional loading and the fragmentation microstructures become more prominent as the strain level increases.

4.7 Effect on grain structure

The specimens were obtained from the initial undeformed copper sheet metal and from the fracture zone (lower region). The observation of the grain structure was made along longitudinal cross-section and transverse cross-section of the obtained specimens. The grain boundaries were evaluated and it was observed that the lubrication state did not have any significant effect on the shape and size of the deformed grain structure. Grain structures for lubrication condition 5 (mineral oil) are presented in Figure 4.32.

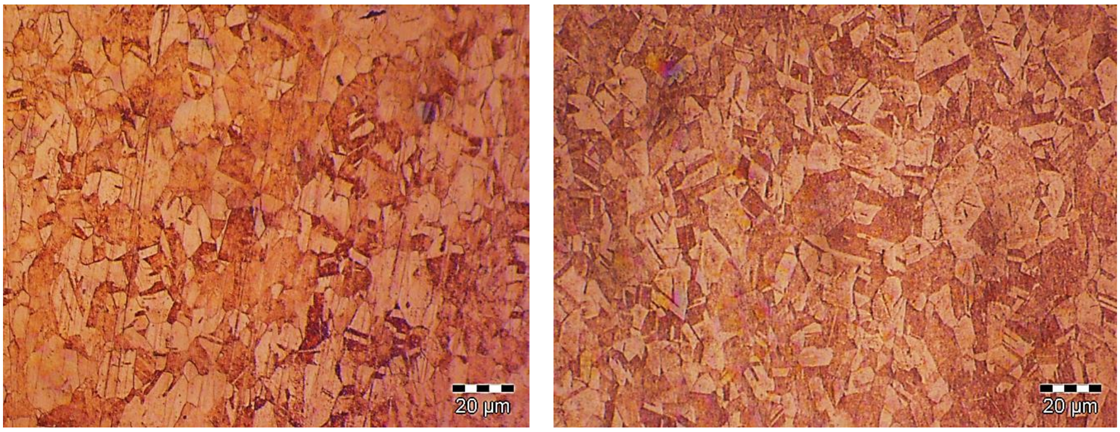

(a) (b)

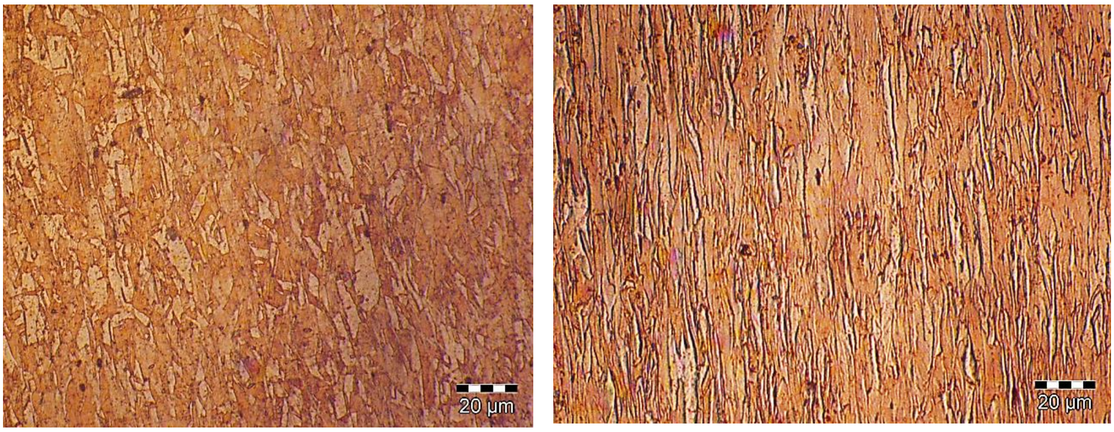

(c) (d)

Figure 4.32: Microscopic image of the grain structures of undeformed specimen from (a) Transverse direction and (b) Longitudinal direction; and lower region from (c) Transverse direction and (d) Longitudinal direction

It can be observed that the grain structures of the lower region of the specimen exhibit elongation (see Figure 4.32c and Figure 4.32d). The grains in transverse direction undergo minor elongation whereas the grains in longitudinal direction has large amount of elongation. This elongation corresponds to the principal major strain. The principal major strain in this case was 1.38.

4.8 Application

Three complex geometries, decoration leaf, vortex decoration bowl and prototype of ship hull, were formed using SPIF to validate the utility of FFL and SFFL for copper. The process parameters were selected in order to obtain the maximum formability (from section 4.5). The spherical end forming tool geometry with 10 mm diameter was used as it provided the maximum formability. The feed rate of 900 mm/min and step down of 0.1 was used to take advantage of higher formability. Mineral oil was used as the lubrication.

4.7.1 Decoration leaf

The decoration leaf as shown in Figure 4.33 was formed using SPIF. Different areas (see Figure 4.34) of the leaf generate various strain paths in the first quadrant of FLD. The strain path was below the FFL and the component was successfully formed without any fracture.

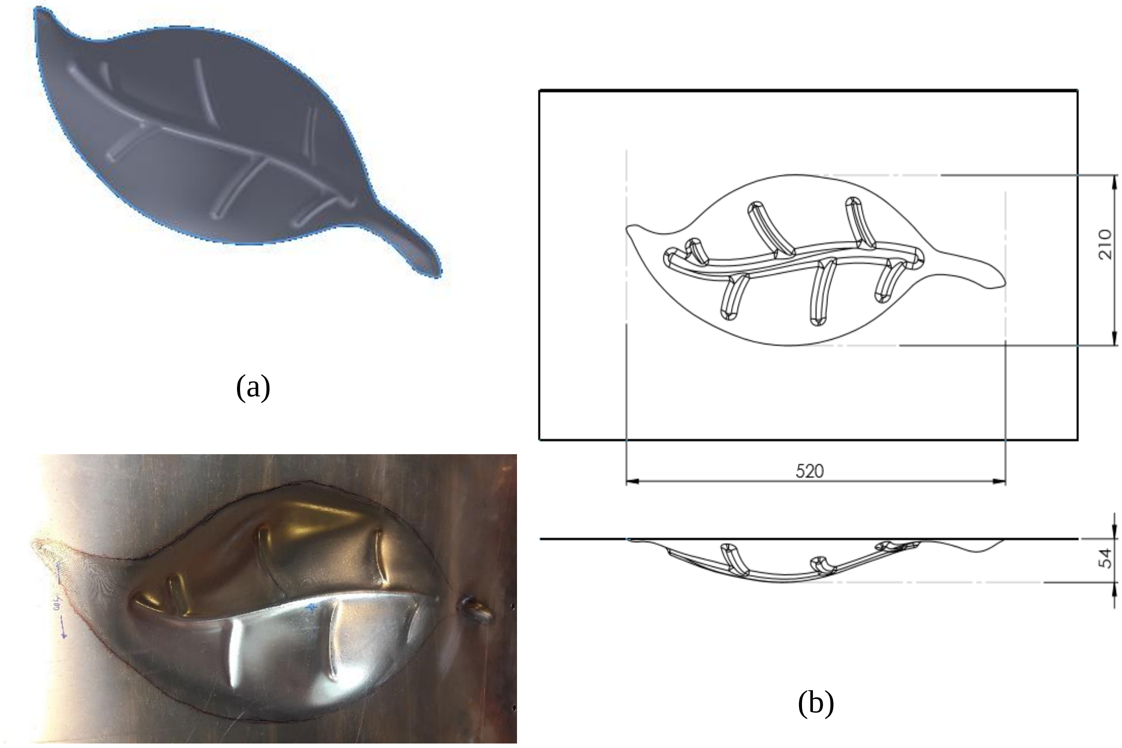

(c)

Figure 4.33: Decoration leaf, a) Isometric view, b) top and side view with dimensions in mm and c) resulting SPIF decorative leaf

Four features (see Figure 4.34) from the formed decoration leaf where evaluated for strain path using circle-grid technique.

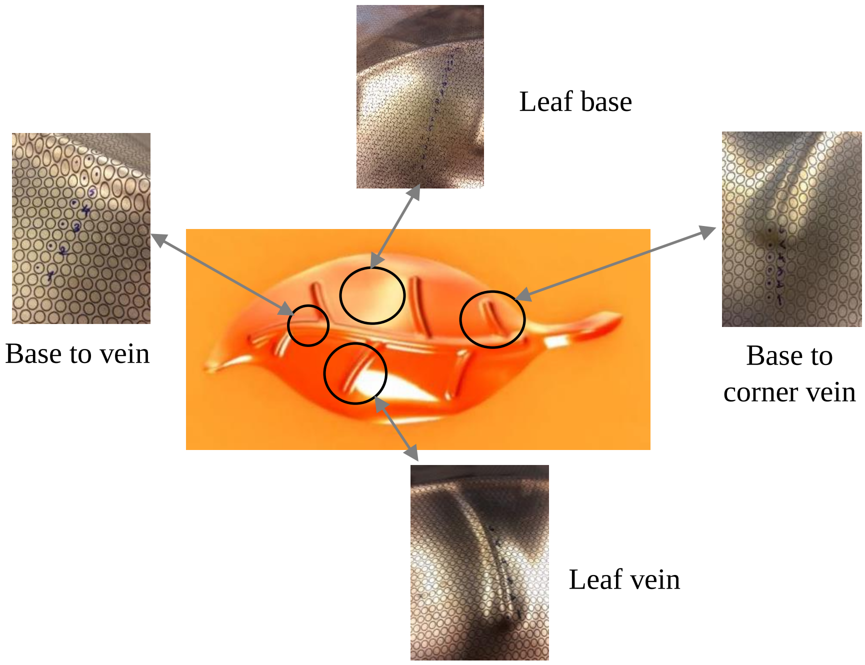

Figure 4.34: Features of decoration leaf selected to evaluate the strain path

Figure 4.35 presents the strain path followed by the points on the features of the decoration leaf. It can be observed from FLD (Figure 4.35) that, all the points lie in the first quadrant, i.e. feature follows the plane and the bi-axial strain deformation. Some of the points in the FLD are very close to the FFL but they do not fracture. This validates that points lying below FFL curve are safe and will not fracture.

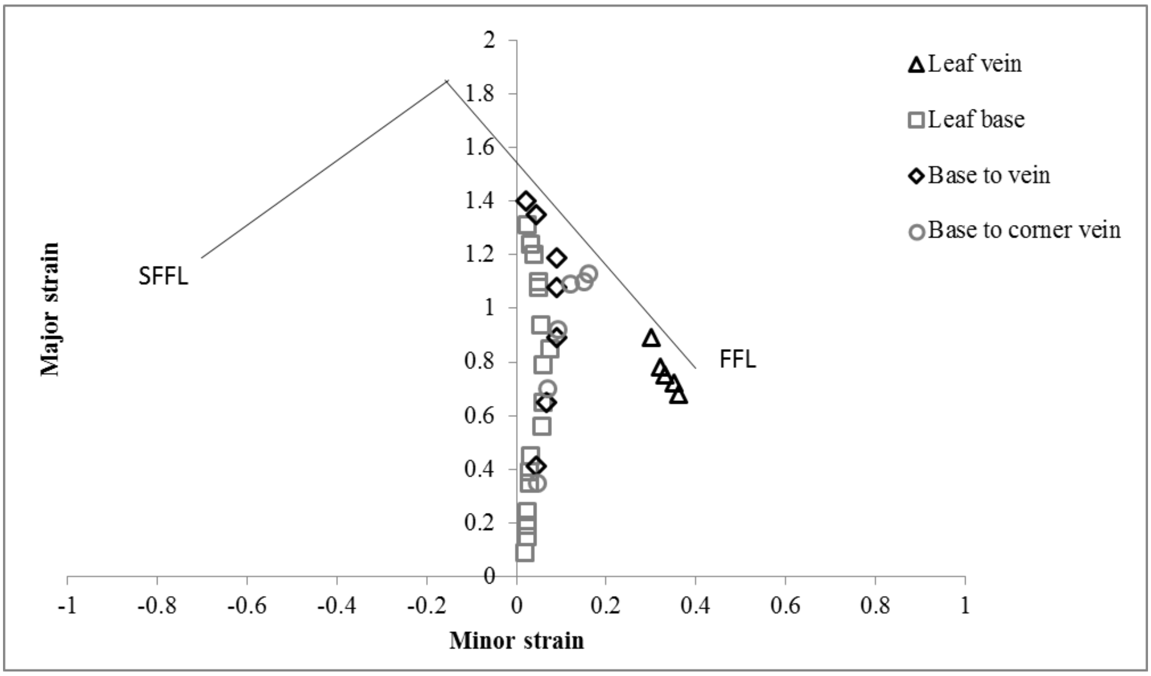

Figure 4.35: Strain path for different areas of decoration leaf in forming limit diagram

4.7.2 Vortex decoration bowl

The vortex decoration bowl, (see Figure 4.36) was formed using SPIF. This component produces strain points in both first and second quadrant. Thus this component can be used to validate both SFFL and FFL. The component was successfully formed without fracture.

Two features, side wall and vortex region (see Figure 4.37), from the formed vortex decoration bowl where evaluated for strain path using circle-grid technique. The side wall feature generated plane strain deformation and vortex region generated deformation in uniaxial region (see Figure 4.38). The measured strain points were found to be below SFFL and FFL are safe and without fracture.

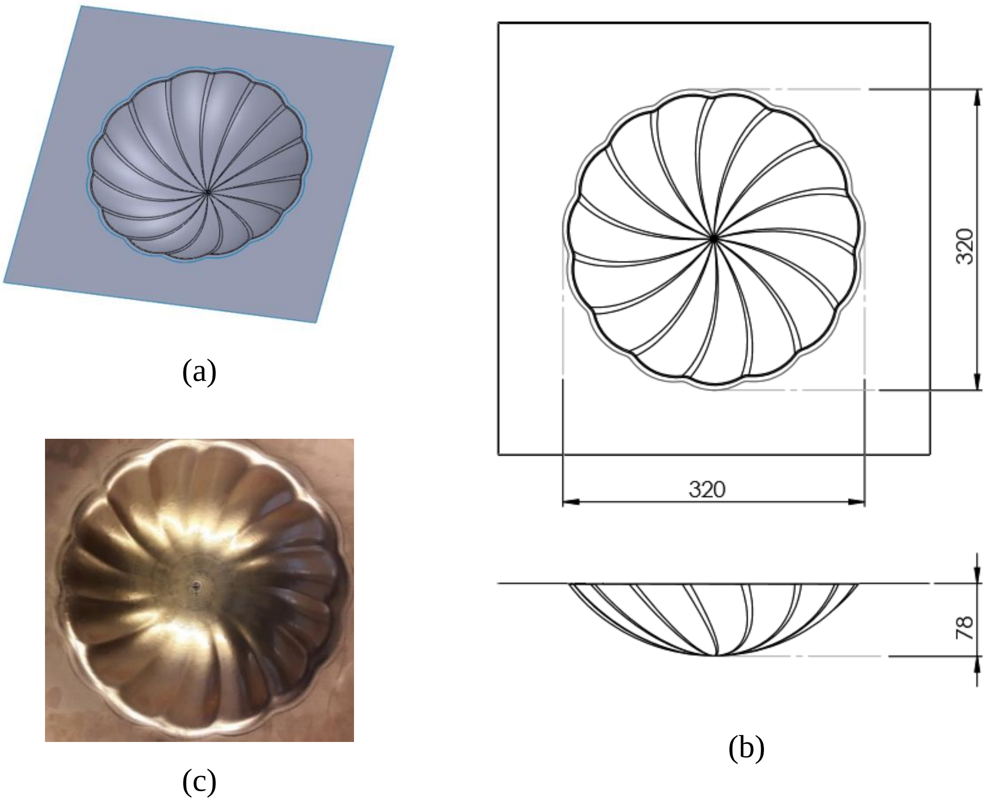

Figure 4.36: Vortex decoration bowl, a) Isometric view, b) top and side view with dimensions in mm and c) resulting SPIF decorative leaf

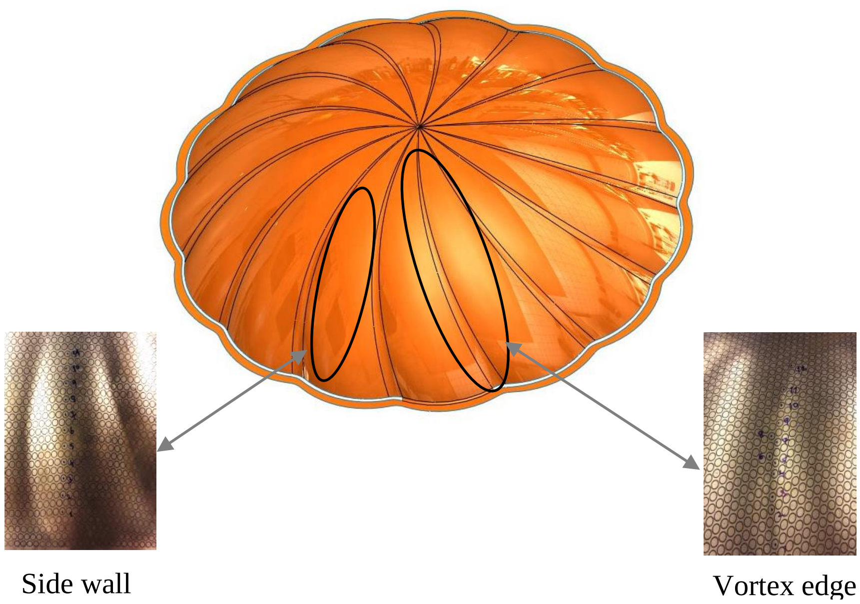

Figure 4.37: Features of vortex decoration bowl selected to evaluate the strain path

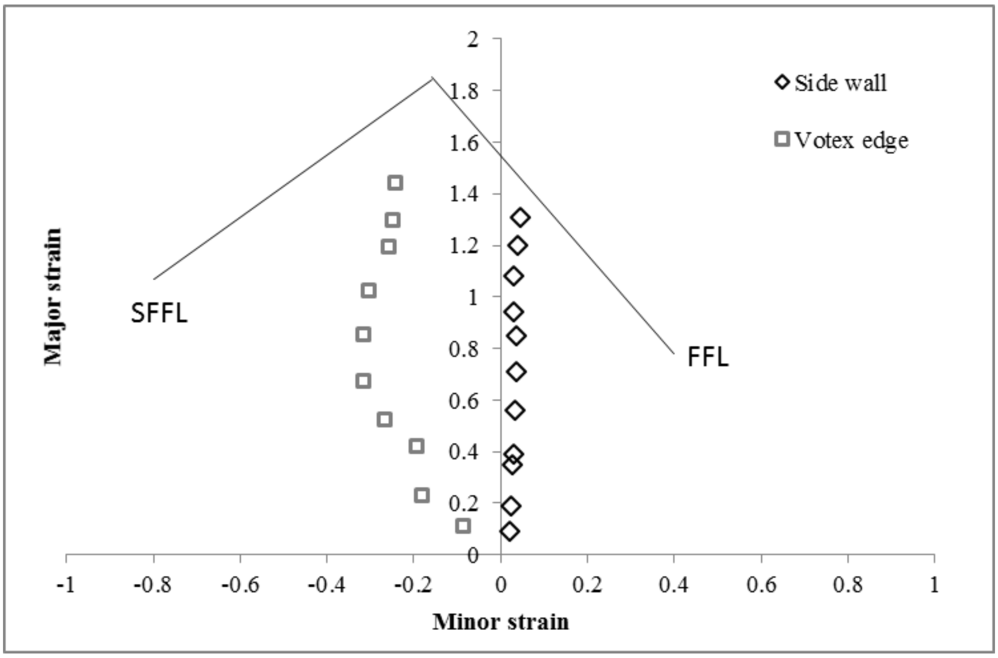

Figure 4.38: Strain path for different areas of the vortex decoration bowl in forming limit diagram

4.7.3 Prototype of Ship hull

The prototype of a ship hull (see Figure 4.39) was formed using SPIF. The component however, fractured in two areas (Figure 4.39c). This two areas, i.e. hull side and hull front (identified in Figure 4.40) has the maximum slope of 60º, which lie within the maximum forming angle limit of 76.99º (see Table 4.8) for the given copper sheet metal.

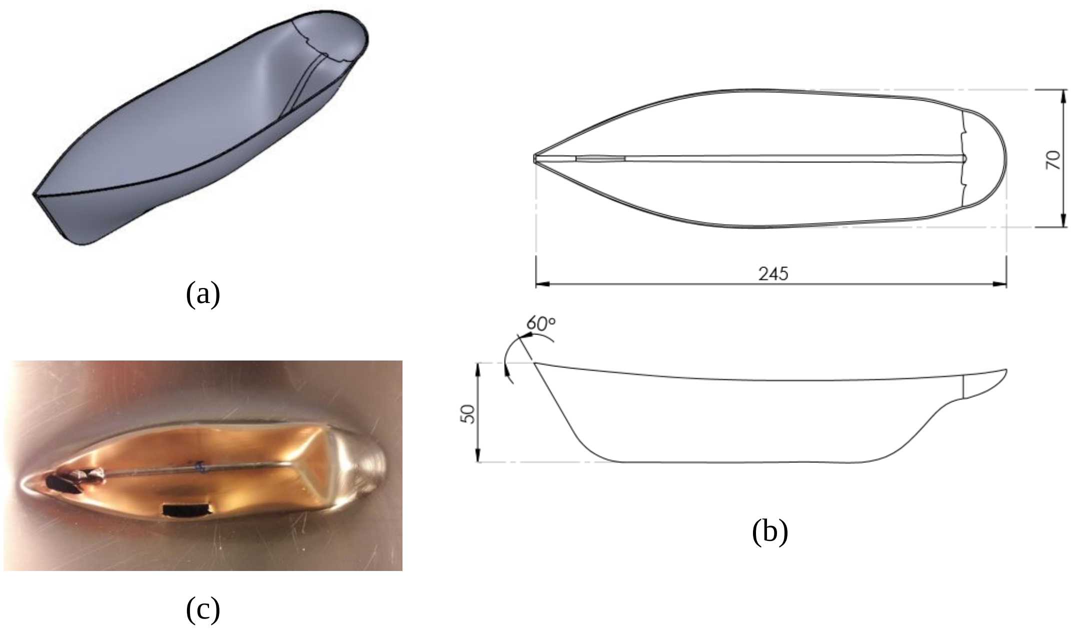

Figure 4.39: Prototype of ship hull, a) Isometric view, b) top and side view with dimensions in mm and c) resulting formed prototype of ship hull

The process was repeated till first fracture appeared (see Figure 4.40) in both the areas so that the fracture strain could be analysed.

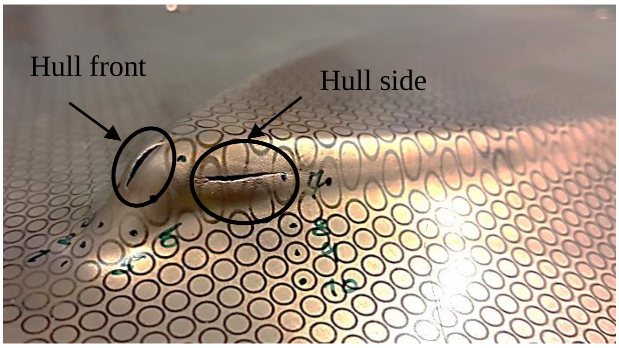

Figure 4.40: Forming the prototype of ship hull till first crack appeared in both the regions

Figure 4.41 shows the strain paths for two different areas of prototype of ship hull where the fracture appeared. The strain path followed by the points lying on both areas, i.e. hull front and hull side followed biaxial deformation.

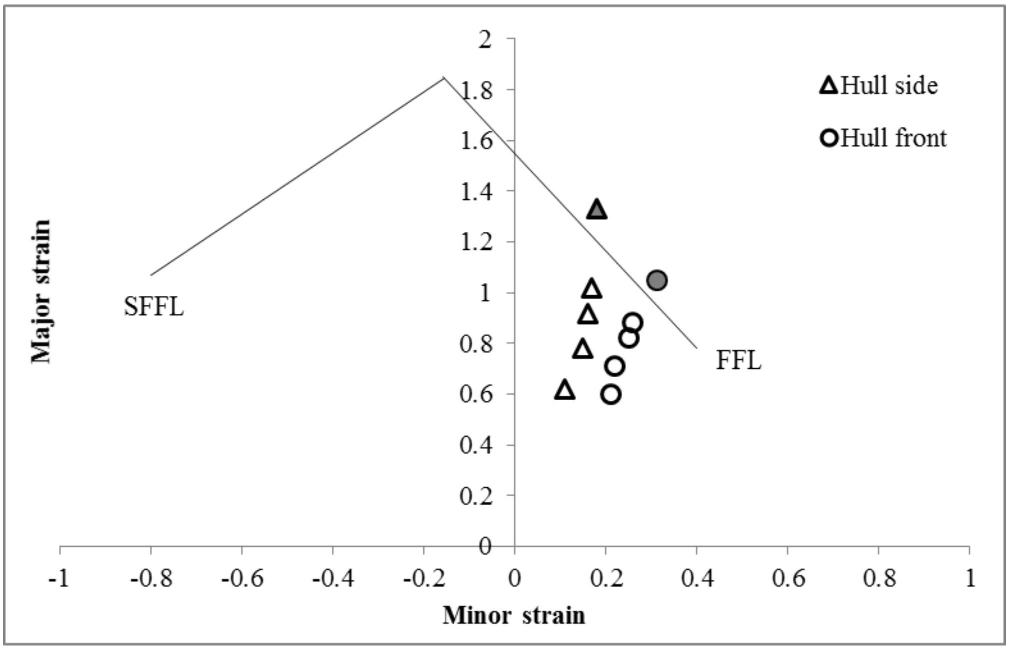

Figure 4.41: Strain path for different areas of prototype of ship hull in forming limit diagram

The fracture points' strains in FLD are indicated by solid filled marker (see Figure 4.40). The fracture strains on the FLD lies above the FFL curve and the strains below FFL are safe.

The strain path analysis of the formed complex geometry applications enables us to validate the FFL and SFFL determined for the copper sheet metal by means of conventional tests (presented in section 4.3). It can be concluded that, in order for component to be formed without fracture, the maximum strain should fall below the SFFL and FFL, in safe zone, in FLD.

Chapter 5 **Conclusions**

The thesis presents a methodology to characterize plastic flow and fracture in single point incremental sheet metal forming. The transition region between SFFL and FFL in FLD is investigated. The specific essential work of fracture (fracture toughness) values for fracture by mode I, mixed mode I&II and mode II of fracture mechanics is calculated. The effect of process parameters and lubrication on the SPIF of copper sheet metal is discussed in detail. The effect of cyclic loading in the SPIF of copper sheet metal is studied and the results are discussed. The SPIF was used to form the complex applications and the same applications were used to validate the obtained SFFL and FFL for the copper sheet metal.

The brief summary of the thesis is presented here after.

The copper sheet metal's properties was determined using the tensile test. Voce and Swift material law for copper sheet metal was determined, with high accuracy using bulge test.

It was observed that the s-DNTT copper specimen are not suitable to determine the fracture toughness for fracture by mixed mode I&II of fracture mechanics and the fracture strains on the FLD, since the specimen did not fracture in the expected ligament area. The newly developed s-CS specimen provides a good alternative to calculate fracture toughness for fracture by mixed mode I&II of fracture mechanics.

The presented s-CS specimen also gave fracture strain points in the FLD, in the transition region between SFFL and FFL, which was previously not investigated. The SFFL is line perpendicular to FFL line in forming limit diagram.

The SFFL and FFL for the copper sheet metal was obtained using the conventional sheet metal, the shear and the staggered specimen tests. These limits were validated using the limiting principal strains obtained from SPIF of copper sheet metal.

The effect of different process parameters on the SPIF formability was investigated. It was found that the forming tool diameter and the step-down are the most influential process parameters that affect the SPIF formability. As the forming tool diameter increases the formability decreases. The spherical end forming tool leads to higher formability than the hemispherical end forming tool. The tool material does not affect the formability, however, the tool material affects the tool wear. For forming of copper sheet metal, using tungsten-carbide tool material results in comparatively less tool wear due to less copper adhesion. As the step down increases the formability decreases. The feed-rate does not have a significant effect on the formability.

The lubrication slightly increases the formability of the copper sheet. The different lubrication conditions does not affect the formability for copper sheet metal. The different lubrication conditions however, significantly affect the surface roughness of the formed component. It was found that the mineral oil is the most economical option to reduce the surface roughness with positively influencing the formability.

The surface roughness of the formed component increases as the strain increases. The surface SEM images were taken to study the surface morphology of the formed conical geometry (till fracture). It was observed in SEM images that, at the higher strains, the fragmentation structures were formed. This fragmentation caused the surface roughness to increase.

It was observed that as the tool diameter decreased the fragmentation density decreased. With this decrease in the fragmentation density the possibility to accommodate the plastic deformation also increases and this might in-turn be the reason for the increase in the formability.

The incremental tool path of the forming tool in SPIF causes cyclic non-proportional loading. This type of loading causes faults like micro-cracks in the formed conical geometry (till fracture). Even though the loading is cyclic in nature the cause of failure is not fatigue. The SEM images from the fractured zone, of the formed component, shows the micro-void coalescence and its alignment suggest fracture by mode I of fracture mechanics. The slip line observed in the surface of the component suggests complex and multi-directional loading mechanism.

The grain boundaries obtained from the transverse section (in-line with tool path) does not show any deformation, whereas the grain boundaries obtained from the longitudinal section showed significant elongation (in the step-down direction).

The SPIF applications with complex geometries like decoration leaf, vortex decoration bowl where successfully formed and applications along with prototype of ship hull were used to validate the FFL and SFFL.

References

[1] S. P. Keeler, "Circular Grid System — A Valuable Aid for Evaluating Sheet Metal Formability," in *SAE Technical Paper 680092*, 1968.

[2] G. M. Goodwin, "Application of Strain Analysis to Sheet Metal Forming Problems in the Press Shop," in *SAE Technical Paper 68009*, 1968.

[3] J. D. Embury and J. L. Duncan, "Formability Maps," *Annu. Rev. Mater. Sci.*, vol. 11, no. 1, pp. 505–521, Aug. 1981.

[4] M. B. Silva, M. Skjoedt, A. G. Atkins, N. Bay, and P. A. F. Martins, "Single-point incremental forming and formability–failure diagrams," *J. Strain Anal. Eng. Des.*, vol. 43, pp. 15–35, 2008.

[5] K. Isik, M. B. Silva, A. E. Tekkaya, and P. A. F. Martins, "Formability limits by fracture in sheet metal forming," *J. Mater. Process. Technol.*, vol. 214, no. 8, pp. 1557–1565, Aug. 2014.

[6] J. Jeswiet, F. Micari, G. Hirt, A. Bramley, J. Duflou, and J. Allwood, "Asymmetric Single Point Incremental Forming of Sheet Metal," *CIRP Ann. - Manuf. Technol.*, vol. 54, no. 2, pp. 88–114, 2005.

[7] Y. H. . Kim and J. J. . Park, "Effect of process parameters on formability in incremental forming of sheet metal," *J. Mater. Process. Technol.*, vol. 130–131, no. 3, pp. 42–46, 2002.

[8] P. A. F. Martins, L. Montanari, V. A. Cristino, and M. B. Silva, *Formability and Simulative Tests in Modern Sheet Metal Forming Education*, no. JANUARY. Berlin, Heidelberg: Springer Berlin Heidelberg, 2014.

[9] L. Yang, L. Smith, A. Gothekar, and X. Chen, "Measure Strain Distribution Using Digital Image Correlation (DIC) for Tensile Tests," *Adv. High Strength Steel Stamp. Team Auto/Steel Partnersh.*, pp. 1–27, 2010.

[10] R. Hill, "A theory of plastic bulging of a metal diaphragm by lateral pressure," *Philos. Mag.*, vol. 41, pp. 1133–1142, 1950.

[11] C. D. Schwindt, M. Stout, L. Iurman, and J. W. Signorelli, "Forming Limit Curve Determination of a DP-780 Steel Sheet," *Procedia Mater. Sci.*, vol. 8, no. January,

pp. 978–985, 2015.

[12] K. Nakazima, T. Kikuma, and K. Hasuka, “Study on the Formability of Steel Sheets,” *Yawata Tech. Rep.*, vol. 264, no. 141–154, 1968.

[13] Standard, “ASTM E8 / E8M-13, Standard Test Methods for Tension Testing of Metallic Materials,” West Conshohocken, PA, 2013.

[14] B. Cotterell and J. K. Reddel, “The essential work of plane stress ductile fracture,” *Int. J. Fract.*, vol. 13, no. 3, pp. 267–277, 1977.

[15] B. Cotterell, E. Lee, and Y. Mai, “Mixed mode plane stress ductile fracture,” *Int. J. Fract.*, vol. 20, no. 1982, pp. 243–250, 1982.

[16] D. R. Shouler and J. M. Allwood, “Design and use of a novel sample design for formability testing in pure shear,” *J. Mater. Process. Technol.*, vol. 210, no. 10, pp. 1304–1313, Jul. 2010.

[17] A. G. Atkins, “Fracture in forming,” *J. Mater. Process. Technol.*, vol. 56, no. 1–4, pp. 609–618, Jan. 1996.

[18] F. A. McClintock, “A Criterion for Ductile Fracture by the Growth of Holes,” *J. Appl. Mech. - Trans. ASME*, vol. 35, pp. 363–371, 1968.

[19] C. M. Muscat-Fenech, S. Arndt, and A. G. Atkins, “The determination of fracture forming limit diagrams from fracture toughness,” *Proc. SheMet 96 Int. Conf.*, vol. I, pp. 249–260, 1996.

[20] Z. Marciniak, “Assessment of material formability,” *Adv. Technol. Plast.*, vol. 1, pp. 685–694, 1984.

[21] M. B. Silva, P. S. Nielsen, N. Bay, and P. A. F. Martins, “Failure mechanisms in single-point incremental forming of metals,” *Int. J. Adv. Manuf. Technol.*, vol. 56, no. 9–12, pp. 893–903, Oct. 2011.

[22] M. Ayada, T. Higashino, and K. Mori, “Central bursting in extrusion of inhomogeneous materials,” *Proc. first ICTP*, vol. 1, pp. 553–558, 1984.

[23] M. B. Silva, K. Isik, A. E. Tekkaya, A. G. Atkins, and P. A. F. Martins, “Fracture toughness and failure limits in sheet metal forming,” *J. Mater. Process. Technol.*, vol. 234, pp. 249–258, Aug. 2016.

[24] T. Madeira, C. M. A. Silva, M. B. Silva, and P. A. F. Martins, “Failure in single point incremental forming,” *Int. J. Adv. Manuf. Technol.*, pp. 1471–1479, 2015.

[25] K. Isik, M. B. Silva, A. G. Atkins, A. Tekkaya, and P. A. Martins, “A new test for determining fracture toughness in plane stress in mode II,” *J. Strain Anal. Eng. Des.*, vol. 50, no. 4, pp. 221–231, May 2015.

[26] A. G. Atkins and Y. W. Mai, “Fracture strains in sheet metal forming and specific essential work of fracture,” *Eng. Fract. Mech.*, vol. 27, no. 3, pp. 291–297, Jan. 1987.

[27] T. Schäfer and R. D. Schraft, “Incremental sheet metal forming by industrial robots using a hammering tool,” *10èmes Assises Eur. Prototypage Rapide, Paris, Fr.*, 2004.

[28] E. Leszak, “Apparatus and Process for Incremental Dieless Forming, Published September 19, 1967,” US3342051, 1967.

[29] W. C. Emmens, G. Sebastiani, and A. H. van den Boogaard, “The technology of Incremental Sheet Forming-A brief review of the history,” *Journal of Materials Processing Technology*. 2010.

[30] W. G. Berghahn, Lee, and G. F. J. Murray, “Method of dieless forming surfaces of revolution,” US3316745, 1967.

[31] P. Suriyaprakan, “Single Point Incremental Forming and Multi-Stage Incremental Forming on Aluminium Alloy 1050,” FEUP, University of Porto, 2013.

[32] B. Mason, “Sheet metal forming for small batches,” Univ. of Nottingham, 1978.

[33] H. Iseki, K. Kato, and S. Sakamoto, “Flexible and incremental sheet metal forming using a spherical roller,” in *Proc. 40th JJCTP*, 1989.

[34] K. Kitazawa, “Incremental sheet metal stretch-expanding with CNC machine tools,” in *Proceedings 4th ICTP, Beijing, China*, 1993, pp. 1899–1904.

[35] M. B. Silva and P. A. F. Martins, “Incremental Sheet Forming,” in *Comprehensive Materials Processing*, vol. 3, 2014, pp. 7–26.

[36] S. Matsubara, “Incremental backward bulge forming of a sheet metal with a hemispherical head tool: a study of a numerical control forming system II,” *J. JSTP*

(in Japanese), vol. 35, pp. 1311–1316, 1994.

[37] M. B. Silva and P. A. F. Martins, “Two-point incremental forming with partial die: Theory and experimentation,” *J. Mater. Eng. Perform.*, vol. 22, no. 4, pp. 1018–1027, 2013.

[38] A. Attanasio, E. Ceretti, C. Giardini, and L. Mazzoni, “Asymmetric two points incremental forming: Improving surface quality and geometric accuracy by tool path optimization,” *J. Mater. Process. Technol.*, vol. 197, no. 1–3, pp. 59–67, 2008.

[39] M. B. Silva, N. Bay, and P. A. F. Martins, “Single-Point Incremental Forming,” in *Sustainable Manufacturing*, Hoboken, NJ, USA: John Wiley & Sons, Inc., 2013, pp. 173–209.

[40] H. Meier, B. Buff, R. Laurischkat, and V. Smukala, “Increasing the part accuracy in dieless robot-based incremental sheet metal forming,” *CIRP Ann. - Manuf. Technol.*, vol. 58, no. 1, pp. 233–238, 2009.

[41] X. H. Cui, J. H. Mo, J. J. Li, J. Zhao, Y. Zhu, L. Huang, Z. W. Li, and K. Zhong, “Electromagnetic incremental forming (EMIF): A novel aluminum alloy sheet and tube forming technology,” *J. Mater. Process. Technol.*, vol. 214, no. 2, pp. 409–427, 2014.

[42] A. Petek, B. Jurisevic, K. Kuzman, and M. Junkar, “Comparison of alternative approaches of single point incremental forming processes,” *J. Mater. Process. Technol.*, vol. 209, no. 4, pp. 1810–1815, 2009.

[43] B. Jurisevic, K. Kuzman, and M. Junkar, “Water jetting technology: an alternative in incremental sheet metal forming,” *Int. J. Adv. Manuf. Technol.*, vol. 31, no. 1–2, pp. 18–23, Oct. 2006.

[44] Y. H. Ji and J. J. Park, “Formability of magnesium AZ31 sheet in the incremental forming at warm temperature,” *J. Mater. Process. Technol.*, vol. 201, pp. 354–358, 2008.

[45] G. Fan, F. Sun, X. Meng, L. Gao, and G. Tong, “Electric hot incremental forming of Ti-6Al-4V titanium sheet,” *Int. J. Adv. Manuf. Technol.*, vol. 49, no. 9–12, pp. 941–947, 2010.

[46] J. R. R. Duflou, B. Callebaut, J. Verbert, and H. De Baerdemaeker, “Laser assisted incremental forming: Formability and accuracy improvement,” *CIRP Ann. - Manuf. Technol.*, vol. 56, no. 2, pp. 273–276, 2007.

[47] G. Hussain, L. Gao, N. Hayat, and X. Ziran, “A new formability indicator in single point incremental forming,” *J. Mater. Process. Technol.*, vol. 209, no. 9, pp. 4237–4242, 2009.

[48] J. M. C. Soeiro, C. M. A. Silva, M. B. Silva, and P. A. F. Martins, “Revisiting the formability limits by fracture in sheet metal forming,” *J. Mater. Process. Technol.*, vol. 217, pp. 184–192, Mar. 2015.

[49] P. A. F. Martins, N. Bay, M. Skjoedt, and M. B. Silva, “Theory of single point incremental forming,” *CIRP Ann. - Manuf. Technol.*, vol. 57, pp. 247–252, 2008.

[50] J. Jeswiet, D. Adams, M. Doolan, T. McAnulty, and P. Gupta, “Single point and asymmetric incremental forming,” *Adv. Manuf.*, vol. 3, no. 4, pp. 253–262, Dec. 2015.

[51] R. Araújo, M. B. Silva, L. Montanari, P. Teixeira, A. Reis, and P. A. F. Martins, “Evaluation of the dimensional accuracy in single point incremental forming,” in *AIP Conference Proceedings*, 2013, vol. 832, no. 2013, pp. 832–835.

[52] B. Lu, Y. Fang, D. K. Xu, J. Chen, H. Ou, N. H. Moser, and J. Cao, “Mechanism investigation of friction-related effects in single point incremental forming using a developed oblique roller-ball tool,” *Int. J. Mach. Tools Manuf.*, vol. 85, pp. 14–29, 2014.

[53] S. B. M. Echrif and M. Hrairi, “Research and Progress in Incremental Sheet Forming Processes,” *Mater. Manuf. Process.*, vol. 26, no. February 2015, pp. 1404–1414, 2011.

[54] M. Skjoedt, M. B. Silva, P. A. F. Martins, and N. Bay, “Strategies and limits in multi-stage single-point incremental forming,” *J. Strain Anal. Eng. Des.*, vol. 45, no. 1, pp. 33–44, 2010.

[55] J. M. Allwood, D. Braun, and O. Music, “The effect of partially cut-out blanks on geometric accuracy in incremental sheet forming,” *J. Mater. Process. Technol.*, vol. 210, no. 11, pp. 1501–1510, 2010.

[56] M. B. Silva, M. Skjoedt, P. A. F. Martins, and N. Bay, "Revisiting the fundamentals of single point incremental forming by means of membrane analysis," *Int. J. Mach. Tools Manuf.*, vol. 48, pp. 73–83, 2008.

[57] K. Jackson and J. Allwood, "The mechanics of incremental sheet forming," *J. Mater. Process. Technol.*, vol. 209, no. 3, pp. 1158–1174, 2009.

[58] W. C. Emmens and A. H. van den Boogaard, "Incremental forming by continuous bending under tension—An experimental investigation," *J. Mater. Process. Technol.*, vol. 209, no. 14, pp. 5456–5463, Jul. 2009.

[59] R. Malhotra, L. Xue, T. Belytschko, and J. Cao, "Mechanics of fracture in single point incremental forming," *J. Mater. Process. Technol.*, vol. 212, no. 7, pp. 1573–1590, 2012.

[60] G. Hussain, L. Gao, and N. Hayat, "Forming Parameters and Forming Defects in Incremental Forming of an Aluminum Sheet: Correlation, Empirical Modeling, and Optimization: Part A," *Mater. Manuf. Process.*, vol. 26, no. 12, pp. 1546–1553, 2011.

[61] T. McAnulty, J. Jeswiet, and M. Doolan, "Formability in single point incremental forming: A comparative analysis of the state of the art," *CIRP J. Manuf. Sci. Technol.*, vol. 16, pp. 43–54, 2016.

[62] J. Jeswiet, E. Hagan, and A. Szekeres, "Forming parameters for incremental forming of aluminium alloy sheet metal," *Proc. Inst. Mech. Eng. Part B J. Eng. Manuf.*, vol. 216, no. 10, pp. 1367–1371, Jan. 2002.

[63] M. Strano, "Technological representation of forming limits for negative incremental forming of thin aluminum sheets," *J. Manuf. Process.*, vol. 7, no. 2, pp. 122–129, 2005.

[64] M. Ham and J. Jeswiet, "Single point incremental forming and the forming criteria for AA3003," *CIRP Ann. - Manuf. Technol.*, vol. 55, no. 1, pp. 241–244, 2006.

[65] G. Hussain, L. Gao, and Z. Y. Zhang, "Formability evaluation of a pure titanium sheet in the cold incremental forming process," *Int. J. Adv. Manuf. Technol.*, vol. 37, pp. 920–926, 2008.

[66] M. Durante, A. Formisano, and A. Langella, "Observations on the influence of

tool-sheet contact conditions on an incremental forming process," *J. Mater. Eng. Perform.*, vol. 20, no. 6, pp. 941–946, 2011.

[67] D. Xu, W. Wu, R. Malhotra, J. Chen, B. Lu, and J. Cao, "Mechanism investigation for the influence of tool rotation and laser surface texturing (LST) on formability in single point incremental forming," *Int. J. Mach. Tools Manuf.*, vol. 73, pp. 37–46, 2013.

[68] G. Buffa, D. Campanella, and L. Fratini, "On the improvement of material formability in SPIF operation through tool stirring action," *Int. J. Adv. Manuf. Technol.*, vol. 66, no. 9–12, pp. 1343–1351, 2013.

[69] S. P. Shanmuganatan and V. S. Senthil Kumar, "Metallurgical analysis and finite element modelling for thinning characteristics of profile forming on circular cup," *Mater. Des.*, vol. 44, pp. 208–215, 2013.

[70] S. Golabi and H. Khazaali, "Determining frustum depth of 304 stainless steel plates with various diameters and thicknesses by incremental forming," *J. Mech. Sci. Technol.*, vol. 28, no. 8, pp. 3273–3278, 2014.

[71] G. Centeno, I. Bagudanch, A. J. J. Martínez-Donaire, M. L. L. García-Romeu, and C. Vallellano, "Critical analysis of necking and fracture limit strains and forming forces in single-point incremental forming," *Mater. Des.*, vol. 63, pp. 20–29, Nov. 2014.

[72] Y. Li, Z. Liu, W. J. T. Daniel, and P. A. Meehan, "Simulation and Experimental Observations of Effect of Different Contact Interfaces on the Incremental Sheet Forming Process," *Mater. Manuf. Process.*, vol. 29, no. February 2015, pp. 121–128, 2014.

[73] X. Ziran, L. Gao, G. Hussain, and Z. Cui, "The performance of flat end and hemispherical end tools in single-point incremental forming," *Int. J. Adv. Manuf. Technol.*, vol. 46, no. 9–12, pp. 1113–1118, 2010.

[74] Z. Liu, Y. Li, and P. A. Meehan, "Experimental investigation of mechanical properties, formability and force measurement for AA7075-O aluminum alloy sheets formed by incremental forming," *Int. J. Precis. Eng. Manuf.*, vol. 14, no. 11, pp. 1891–1899, 2013.

[75] T. Obikawa, S. Satou, and T. Hakutani, “Dieless incremental micro-forming of miniature shell objects of aluminum foils,” *Int. J. Mach. Tools Manuf.*, vol. 49, no. 12–13, pp. 906–915, 2009.

[76] Q. Zhang, F. Xiao, H. Guo, C. Li, L. Gao, X. Guo, W. Han, and A. B. Bondarev, “Warm negative incremental forming of magnesium alloy AZ31 Sheet: New lubricating method,” *J. Mater. Process. Technol.*, vol. 210, no. 2, pp. 323–329, Jan. 2010.

[77] V. Mugendiran, A. Gnanavelbabu, and R. Ramadoss, “Parameter optimization for surface roughness and wall thickness on AA5052 Aluminium alloy by incremental forming using response surface methodology,” *Procedia Eng.*, vol. 97, pp. 1991–2000, 2014.

[78] G. Hussain, L. Gao, N. Hayat, Z. Cui, Y. C. Pang, and N. U. Dar, “Tool and lubrication for negative incremental forming of a commercially pure titanium sheet,” *J. Mater. Process. Technol.*, vol. 203, pp. 193–201, 2008.

[79] M. Skjoedt, M. B. Silva, N. Bay, P. A. F. Martins, and T. Lenau, “Single point incremental forming using a dummy sheet,” *2nd Int. Conf. New Form. Technol. Bremen, Sept. 20-21*, 2007.

[80] N. G. Azevedo, J. S. Farias, R. P. Bastos, P. Teixeira, J. P. Davim, and R. J. Alves de Sousa, “Lubrication aspects during Single Point Incremental Forming for steel and aluminum materials,” *Int. J. Precis. Eng. Manuf.*, vol. 16, no. 3, pp. 589–595, Mar. 2015.

[81] K. Hamilton and J. Jeswiet, “Single point incremental forming at high feed rates and rotational speeds: Surface and structural consequences,” *CIRP Ann. - Manuf. Technol.*, vol. 59, no. 1, pp. 311–314, 2010.

[82] R. Ben Hmida, S. Thibaud, A. Gilbin, and F. Richard, “Influence of the initial grain size in single point incremental forming process for thin sheets metal and microparts: Experimental investigations,” *Mater. Des.*, vol. 45, pp. 155–165, Mar. 2013.

[83] G. Ambrogio and L. Filice, “Three-dimensional FE simulation of single point incremental forming: experimental evidences and process design improving,” *Proc Int. Conf. Comput. Plast.*, pp. 3–6, 2005.

[84] M. Amino, M. Mizoguchi, Y. Terauchi, and T. Maki, "Current Status of 'Dieless' Amino's Incremental Forming," *Procedia Eng.*, vol. 81, no. October, pp. 54–62, 2014.

[85] G. Ambrogio, L. De Napoli, L. Filice, F. Gagliardi, and M. Muzzupappa, "Application of Incremental Forming process for high customised medical product manufacturing," *J. Mater. Process. Technol.*, vol. 162–163, pp. 156–162, May 2005.

[86] J. R. Duflou, B. Lauwers, J. Verbert, F. Gelaude, and Y. Tunckol, "Medical Application of Single Point Incremental Forming: Cranial Plate Manufacturing," *Virtual modeling and rapid manufacturing*. pp. 161–166, 2005.

[87] J. M. Allwood, G. P. F. King, and J. Duflou, "A structured search for applications of the incremental sheet-forming process by product segmentation," *Proc. Inst. Mech. Eng. Part B J. Eng. Manuf.*, vol. 219, no. 2, pp. 239–244, Jan. 2005.

[88] R. Araujo, P. Teixeira, L. Montanari, A. Reis, M. B. Silva, P. A. Martins, R. Araújo, P. Teixeira, L. Montanari, A. Reis, M. B. Silva, and P. A. Martins, "Single point incremental forming of a facial implant," *Prosthet. Orthot. Int.*, vol. 38, no. 5, pp. 369–378, Oct. 2014.

[89] Tanaka S., T. Nakamura, K. Hayakawa, H. Nakamura, and K. Motomura, "Incremental Sheet Metal Forming Process for Pure Titanium Denture Plate," *Proc. 8th Int. Conf. Technol. Plast. – ICTP*, pp. 135–136, 2005.

[90] N. A. Sakharova and J. V. Fernandes, "Strain path change effect on dislocation microstructure of multicrystalline copper sheets," *Mater. Chem. Phys.*, vol. 98, no. 1, pp. 44–50, 2006.

[91] M. Atkinson, "Accurate determination of biaxial stress—strain relationships from hydraulic bulging tests of sheet metals," *Int. J. Mech. Sci.*, vol. 39, no. 7, pp. 761–769, Jul. 1997.

[92] D. L. McDowell, O. K. Stahl, S. R. Stock, and S. D. Antolovich, "Biaxial path dependence of deformation substructure of type 304 stainless steel," *Metall. Trans. A*, vol. 19, no. 5, pp. 1277–1293, 1988.

[93] J. Schijve, "Fatigue as a Phenomenon in the Material," in *Fatigue of Sructure and*

materials, XXI., Springer, 2009, pp. 13–58.

[94] F. Z. Utyashev and G. I. Raab, “The model of structure refinement in metals at large deformations and factors effecting grain sizes,” *Rev. Adv. Mater. Sci.*, vol. 11, pp. 137–151, 2006.